

Reforming towards renewable hydrogen

Citation for published version (APA):

de Nooijer, N. C. A. (2020). *Reforming towards renewable hydrogen: biogas steam reforming in a fluidized bed membrane reactor*. [Phd Thesis 1 (Research TU/e / Graduation TU/e), Chemical Engineering and Chemistry]. Technische Universiteit Eindhoven.

Document status and date:

Published: 20/02/2020

Document Version:

Publisher's PDF, also known as Version of Record (includes final page, issue and volume numbers)

Please check the document version of this publication:

- A submitted manuscript is the version of the article upon submission and before peer-review. There can be important differences between the submitted version and the official published version of record. People interested in the research are advised to contact the author for the final version of the publication, or visit the DOI to the publisher's website.
- The final author version and the galley proof are versions of the publication after peer review.
- The final published version features the final layout of the paper including the volume, issue and page numbers.

[Link to publication](#)

General rights

Copyright and moral rights for the publications made accessible in the public portal are retained by the authors and/or other copyright owners and it is a condition of accessing publications that users recognise and abide by the legal requirements associated with these rights.

- Users may download and print one copy of any publication from the public portal for the purpose of private study or research.
- You may not further distribute the material or use it for any profit-making activity or commercial gain
- You may freely distribute the URL identifying the publication in the public portal.

If the publication is distributed under the terms of Article 25fa of the Dutch Copyright Act, indicated by the "Taverne" license above, please follow below link for the End User Agreement:

www.tue.nl/taverne

Take down policy

If you believe that this document breaches copyright please contact us at:

openaccess@tue.nl

providing details and we will investigate your claim.

Reforming Towards Renewable Hydrogen

Biogas Steam Reforming in a Fluidized Bed Membrane Reactor

PROEFSCHRIFT

ter verkrijging van de graad van doctor aan de Technische Universiteit Eindhoven, op gezag van de rector magnificus prof.dr.ir. F.P.T. Baaijens, voor een commissie aangewezen door het College voor Promoties, in het openbaar te verdedigen op donderdag 20 februari 2020 om 11:00 uur

door

Niek Camiel Adriaan de Nooijer

geboren te Oostburg

Dit proefschrift is goedgekeurd door de promotoren en de samenstelling van de promotiecommissie is als volgt:

voorzitter:	prof.dr. Cees van der Geld
1 ^e promotor:	prof.dr.ir. M. van Sint Annaland
2 ^e promotor:	prof.dr. F. Gallucci
leden:	dr. L.M.P. Madeira (Universidade do Porto)
	prof.dr.ir. A. Nijmeijer (UT)
	prof.dr.ir. D.C. Nijmeijer
	prof.dr.ir. J.A.M. Kuipers
adviseur(s):	Ing. E. Palo (KT-Kinetics Technology S.p.A.)

Het onderzoek of ontwerp dat in dit proefschrift wordt beschreven is uitgevoerd in overeenstemming met de TU/e Gedragscode Wetenschapsbeoefening.



The research described in this thesis has been carried out in the Multiphase Reactors Group (SMR), division Chemical Process Intensification (SPI), within the Chemical Engineering and Chemistry Department of Eindhoven University of Technology, The Netherlands.

The presented work has been part of the project BIONICO. This project has received funding from the Fuel Cells and Hydrogen 2 Joint Undertaking under grant agreement No 671459. This Joint Undertaking receives support from the European Union's Horizon 2020 Research and Innovation Programme, Hydrogen Europe and N.ERGHY.

Copyright © 2020 by N.C.A. de Nooijer

All rights reserved. No part of the material protected by this copyright notice may be reproduced or utilized in any form or by any means, electronic or mechanical, including photocopying, recording or by any information storage and retrieval system, without the prior permission of the author.

Printed by: Gildeprint

A catalogue record is available from the Eindhoven University of Technology Library.

ISBN: 978-90-386-4985-6

Acknowledgements

I use as little as possible, often too little, words when expressing myself. With these acknowledgements, I hope to express my sincere gratitude to all involved in the completion of this thesis.

It feels appropriate to start with the person that convinced me to start this PhD. José, working together with you, both as your student and as colleague, has been a pleasure. Your enthusiasm and curiosity are contagious, you made the choice to start this PhD an easy and good one. I truly hope we have the possibility to work together again in the future.

Fausto, as my daily supervisor you also offered me freedom and autonomy in my research. You were always - if not abroad, but even then - available and prepared to help. Because of you, I was able to enjoy being involved and collaborating in several EU projects (but also good food and nice people). Martin, als student was ik erg gesteld op je colleges, waarin je altijd duidelijk en behulpzaam was. Dit geldt ook voor onze project meetings. Je hebt altijd een overvloed aan kennis en ideeën. I want to thank you both very much for all the opportunities, help and contributions I have received from you in and to my work.

Without good membranes, my research would not have been possible. To my luck, this meant working together with the people from Tecnalía. I want to thank all of you for sharing all your knowledge on membranes, and for great times on conferences and project meetings. Alfredo, thank you for your feedback and all the discussions we had, they were of tremendous value for my research. Ekain, thank you for all our email conversations and your feedback. Jon, first of all sorry that I (sometimes) unfortunately broke your hard work rather quickly. I think we can say we learned a lot because of it. Alba, I now address you as part of Tecnalía, but you have been an awesome office mate and colleague in Eindhoven.

Joris, Joost, Thijs en Herbert, zonder jullie hulp en inzicht had ik mijn werk nooit kunnen doen. Ik heb steeds met veel plezier gebruik gemaakt van jullie kundigheid. Als ik iets nodig had of een idee had, hadden jullie altijd een oplossing. Bedankt voor jullie samenwerking. Judith en Ada, bedankt voor jullie hulp.

My research was part of the European project BIONICO. I want to thank all the people involved in the consortium. It was a pleasure working in this project with you. Thank you for all the project meetings, which helped to give direction to my work, and the great dinners we had.

I have also had the luck to be involved in the European projects FERRET and Promeca. Thank you all and in particular Carlo, Antonella, Emma, Lorena and Vitoria for your hospitality.

Parts of this thesis include work of students who sank their teeth into my research topic. Andres, Emma, Guido, Jessica, Jos, Julio, Konstantinos, Leon, Stefano, Teresa, Thijs, Troy en Wout, I want to thank you all for your contribution and what I learned from you along the way.

I have truly enjoyed working in the SMR group the last 4 years and a bit. This is mostly because of the great environment and colleagues. Aitor, Vincenzo, Marian, Kai, Michela, Milan, Ramon, Alessandro, Maria, Francesco, Wendy, Stefan, Evan, Tim, Solomon, Giulia, Arash, Nerea, Ivo, Morteza. working in the lab, having lunch, discussions (about food...), going to conferences, and so on, were a pleasure to have enjoyed with you.

I also want to thank all my friends and relatives outside of the TU/e. From Zeeland through Breda and Tilburg to The Hague, a lot of people have crossed my path in school, university, camping, skateboarding or surfing or any other way. All of you contributed to what I am now, thank you for that. Niels, we benoemen onze vriendschap niet vaak, ik geloof ook niet dat dit nodig is, maar ik ga deze kans wel aangrijpen. Onze vriendschap gaat verder terug dan dat we ons kunnen herinneren en ik hoop dat hij tot het zelfde punt zal duren. Bedankt. Paul, of het nu skateboarden, surfen of onderzoek is, wij delen onze passies. Al deze dingen zijn belangrijk voor mij en voor het volbrengen van deze thesis. Jij bent onvermijdelijk verbonden met al deze dingen en daarom ook met deze thesis. Bedankt.

Marijtje, wij gaan maar ietsjes verder terug dan het begin van mijn PhD. Je zette toen mijn wereld op zijn kop maar ook mijn voeten op de grond. Dit doe je nog elke dag. De woon-werk reistijd deed er niet toe met jou als bestemming. Zonder

jou had het bereiken van dit punt nooit zo fijn geweest. Bedankt voor alles en in het bijzonder voor je liefde, vertrouwen en vrijheid.

Sandra, ik kijk tegen je op. Jij kan alles wat je wil.

Pa, Ma, bedankt voor alles, ik geloof niet dat ik dit al eens heb gezegd, sorry. Jullie zijn er altijd voor me geweest en hebben me steeds onvoorwaardelijk gesteund. Ik ben jullie hier verschrikkelijk dankbaar voor en ontzettend trots op jullie.

Ik heb mijn best gedaan.

Niek de Nooijer,

The Hague, December 2019

Summary

Hydrogen has an important role to play in the efforts to reduce anthropogenic GHG emissions. Nowadays, hydrogen is mainly used in chemical and industrial processes. The largest part of this hydrogen is produced from fossil fuels with significant GHG emissions. Besides the main use of hydrogen in processing, it is also acknowledged as a future energy carrier, as it can be converted to energy without any GHG emissions. Both uses for hydrogen will increase in the near future and will result in a larger demand for hydrogen. From this the need arises to produce hydrogen from renewable resources.

One of the renewable primary energy sources that could be converted into hydrogen is biomass. Biomass is organic matter, which is produced by the capture of carbon from atmospheric CO₂, the CO₂ emissions from biomass can therefore be considered carbon neutral. Hydrogen from biomass can be produced either through gasification to produce syngas or through biomass conversion in biofuels. One of the biofuels pathways that shows great potential as fuel source for the production of hydrogen is biogas. Biogas consists mainly out of carbon dioxide and methane, and the methane in the biogas can be converted to hydrogen.

Most of the hydrogen nowadays is produced through reforming of natural gas, which, like biogas, also consists mainly of methane. The conventional methane steam reforming process imposes several challenges for the conversion of biogas to hydrogen. Process intensification can offer a solution for these challenges. In the proposed concept in-situ extraction of hydrogen using hydrogen permselective membranes improves the yields and reduces the requirements for downstream separation. This integration makes, the so-called membrane reactor, ideal for the production of hydrogen from a decentralised source as biogas.

The membrane reactor concept has been studied over the past 30 years and the membranes used for the hydrogen extraction have improved significantly over these years. This improvement resulted in a high selectivity and high hydrogen flux resulting in high demands on the heat and mass transfer and reaction rates in the often used fixed bed systems. To overcome the limitations of the fixed bed, the fluidized bed membrane reactor was developed.

The application of fluidized bed membrane reactors has been demonstrated for the production of hydrogen from methane, however, the path from biogas to hydrogen requires further investigation. Optimization of the membrane performance and particularly the stability of the membrane under biogas reforming and fluidization conditions is imperative for the further development of the concept. Moreover, an accurate prediction of the mass transport rates of hydrogen is crucial for the design of such a reactor system and requires further understanding. These topics are investigated in detail in this thesis.

Chapter 2 investigates the long-term stability of thin-film Pd-Ag membranes supported on porous Al₂O₃ supports for up to 2650 hours. The work compares different sealing techniques at high temperature (400-600 °C) conditions and investigates the stability of these membranes in fluidized bed conditions. Results show the importance of the sealing and the benefit from the reduction in the number of sealings. By dead-end finger-like membranes the nitrogen permeation is decreased by 50%. Post characterization indicates a main contribution of small pinholes (<55 nm), due to grain agglomeration. It is also shown that at high temperature, above 450 °C, the fluidization conditions result in an abrasive action on the membranes, which causes a decrease in perm-selectivity.

H₂S, a trace component in biogas, is another component that can adversely affect the stability of the membranes. In chapter 3 the effect of trace amounts of H₂S on the membrane performance was evaluated. It was shown Pd-based membranes alloyed with gold show improved stability in the membrane flux, but that still even trace amounts <2 ppm can significantly deteriorate the membrane performance. The hydrogen flux could decrease to even less than 10% of the original flux. The strong dependence on the partial pressure of H₂S could be well described using a Langmuir adsorption term. No sulphide formation was measured, however, deterioration of the membranes was observed. It is concluded that contact with H₂S should be avoided.

Hydrogen production in a fluidized bed membrane reactor from biogas is demonstrated in chapter 4. With synthetic biogas, experiments have been performed in a single membrane system to investigate the influence of pressure, temperature and feed composition. Methane conversions of 68% at 533 °C for

biogas steam reforming have been obtained, with a hydrogen purity up to 99.88%. The experimental results have subsequently been used to validate a 1D phenomenological two-phase model that accounts for mass transfer limitations from the emulsion phase towards the membrane surfaces (concentration polarisation). A mass transfer boundary film layer thickness of 0.54 cm was found to adequately describe the experimental results.

The scaling up of the single-membrane fluidized bed membrane reactor demonstrated in chapter 4, is investigated in chapter 5. A fluidized bed membrane reactor with 5 and 7 membranes in different configurations has been investigated. Hydrogen recoveries above 80% have been demonstrated. The effects of the fluidization regime (relative fluidization velocity) on the extent of concentration polarisation is investigated. Moreover, it is shown that the configuration in which the membranes are placed in the system can significantly influence the performance. Evaluation of the performance of the system with different membrane configurations showed a clear increase in the extent of concentration polarisation (up to about 25% decrease in the overall mass transfer rate) when the membranes are placed too close to one another and the mass transfer boundary layers of neighbouring membranes start interacting.

Chapter 6 gives a brief summary of the investigations and conclusions made on the investigated technology and put this into context with a economic analysis of the process of biogas steam reforming in a fluidized bed membrane reactor. The cost of hydrogen with the fluidized bed membrane reactor technology is found to be 6.62–6.47 €/kg, which is comparable to the reference case. The cost of hydrogen could be decreased with 6%, when the mass transfer could be enhanced by only 50%. Membrane stability and lifetime remain critical for future application of the fluidized membrane reactor technology for biogas steam reforming.

Table of contents

Acknowledgements

Summary

1.	General introduction	1
2.	Stability of thin-film Pd-based supported membranes	13
3.	Influence of H₂S on thin-film PdAgAu membranes	53
4.	Biogas steam reforming: modelling and experimental validation	81
5.	Effects of scale-up on membrane reactor performance	129
6.	Economic perspective for biogas to hydrogen	153
	List of publications	176
	Curriculum vitae	180



Chapter

One

General introduction

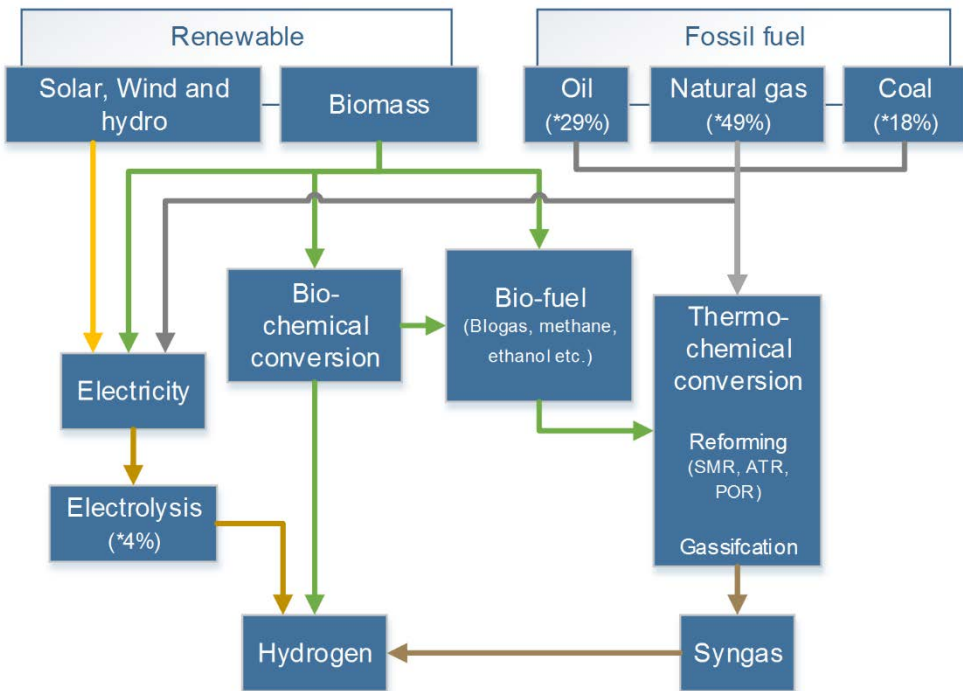
1.1. The water producer

Clapham (England), 1766: Hendry Cavendish is the first to isolate hydrogen (H_2) in his laboratory, which was also his house (A feeling I have felt related with more than once during my Ph.D.). Experimenting with hydrogen, he proved its high energy content (and that shaving was not the only way to remove one's facial hair). In 1783, Antoine Lavoisier was the first to identify hydrogen. He named it after the fact that it produced water when combusted [1]. Lavoisier and his wife later came up with the revolutionary concept of mass conservation, the foundation of all modern chemistry. This was, unfortunately for him, not the only revolution he was involved in. Lavoisier was convicted and guillotined on the 8th of May 1794 in Paris.

In 2015, Paris is the stage of a new revolution: the climate revolution. The Paris agreement, signed by 194 countries and the European Union, in which is recognised the need for an effective and progressive response to the urgent threat of climate change on the basis of the best available scientific knowledge [2]. Amongst others, this means active actions for climate change mitigation. Greenhouse gases are responsible for the observed temperature increase on earth by retaining heat in the atmosphere (greenhouse effect). Carbon dioxide (CO_2), the most famous greenhouse gas (GHG), was measured in the atmosphere for the first time in 1958 at 316 parts per million (ppm) [3]. Currently, the CO_2 concentration in the atmosphere is as high as 415 ppm. Other greenhouse gasses are methane (CH_4), nitrous oxide (N_2O) and fluorinated gases. The significant rise in the concentration of all these gasses is very likely responsible for the change in climate [4]. Studies have confirmed that the use of fossil fuels accounts for the majority of anthropogenic GHG emissions [4]. The largest part of these fossil fuels are used as an energy source. As the demand for energy is expected to keep increasing and 81% of the world primary energy supply was fossil based in 2016 [5], the mitigation of climate change is a matter of drastically reducing the consumption of fossil fuels and GHG emissions from it. In this climate revolution against anthropogenic GHG emissions the *water producer* has a dual role to play.

Today, hydrogen is mainly playing the role of feedstock for chemical processes. In industrial processing, hydrogen is used in oil refining and in the production of

ammonia and methanol, but also in glass, electronics and metal industry. The second, and increasingly important, role for hydrogen is the one of energy carrier, replacing fossil-based energy carriers that emit GHG when converted. With use of a fuel cell hydrogen can be converted to water, electricity and heat. This means hydrogen can be converted to power without GHG emissions. These roles of and their effect on the climate revolution depend on the condition that the hydrogen is produced without GHG emissions or from a renewable source.



*World wide hydrogen production in 2006

Figure 1.1. Hydrogen production paths.

1.2. Hydrogen production

Antoine Lavoisier reacted steam at high temperature with iron to produce iron oxide and hydrogen. Nowadays, various paths for the production of hydrogen have been developed. As shown in Figure 1.1, these paths can be divided into two groups of primary energy use: fossil and renewable. The fossil based hydrogen is

mainly produced from syngas, a mixture of CO and H₂. Syngas is produced via coal gasification, or through reforming of hydrocarbons. The hydrogen can then be separated from the syngas. These processes are energy intensive and require part of the fuel to provide energy to sustain the reaction, resulting in significant GHG emissions. The majority of hydrogen produced today is fossil-based. The demands for hydrogen both as an energy carrier and as feedstock are steadily increasing. This means that for hydrogen to play an effective role in the reduction of anthropogenic GHG emissions the use of primary energy for the production of hydrogen needs to transition towards renewable.

Hydrogen can also be produced from water through electrolysis. The electricity for this process can either be derived from fossil fuels, or from a renewable energy source, such as solar or wind. When renewable energy sources are used, the produced hydrogen is renewable. Strong developments are ongoing in the field of water electrolysis, although the production costs of hydrogen from renewable energy remain high. Moreover, significant deployment of this technology requires more time and further increases the demand for renewable electricity.

Another primary energy source from which hydrogen can be produced is biomass. Biomass consists of organic matter, which is produced by the capture of carbon from atmospheric CO₂. This process occurs over relatively short timescales compared to the formation of fossil fuels. When biomass is used as a primary energy source, there are often still GHG emissions. However, when the rate of biomass production is equal to the rate of its consumption, the GHG emissions can be considered carbon neutral, and biomass can be considered a renewable energy source. Hydrogen from biomass can be produced either through gasification to produce syngas or through biomass conversion into biofuels. These biofuels (e.g. bio-oils) can then be converted into hydrogen by using conventional technologies. This offers a paths to produce renewable hydrogen while using proven technology.

1.3. Biogas to hydrogen

One of these paths is the production of hydrogen from biogas. Biogas is produced from the decomposition of biomass under anaerobic conditions [6]. The biomass

can consists of organic substrates such as manure, sewage sludge, energy crops and organic fractions of industrial or municipal waste. Decomposition can take place either in an anaerobic digester or in a landfill. During the fermentation process, microbial species convert the biomass into biogas, consisting mainly of methane and CO₂. The methane in the biogas can be converted into hydrogen in the reforming process [7,8].

1.4. Intensified reformer

Reforming is the process in which hydrocarbons are converted in the presence of a reforming agent such as steam, to form a hydrogen rich mixture. Methane is most commonly used as feedstock in the reforming process for hydrogen production, because it gives the highest hydrogen yield per mass of fossil fuel. Various reforming processes are available: Partial Oxidation Reforming (POR), Autothermal Reforming (ATR), Dry Reforming (DR) and the most commonly applied Steam Reforming (SR) [9]. In the conventional steam reforming process, methane is converted in an excess of steam via the steam reforming reaction into a CO and hydrogen rich gas. This reaction is endothermic and therefore requires high temperatures (800 – 1000 °C). To increase the hydrogen yield, the water gas shift (WGS) reaction is performed. The WGS reaction converts CO and steam into hydrogen and CO₂ in an exothermic process (thus requiring lower temperatures). Eventually, to obtain pure hydrogen, the hydrogen needs to be separated, which is usually carried out using pressure swing adsorption (PSA). Due to its energy intensive nature, this process is more feasible at a large scale (where heat streams can be recovered for steam and electricity production and export). This makes the process less favourable for a decentralised source such as biogas. Moreover, the concentration of methane in biogas is much lower compared to natural gas, requiring larger units for the same production capacity. This means that the biogas should first be upgraded to bio-methane before it can be applied in a conventional steam reforming process, which is another energy intensive step.

Process intensification is the improvement of a process at different scales to significantly increase process efficiency. Research in the field of process intensification on the conditions, catalyst and reactor configuration have resulted

in the development of novel reforming concepts. One of these novel reforming concepts is the membrane reactor. In a membrane reactor, reaction and hydrogen separation are combined in one single unit. For the steam reforming process this means that SMR, WGS and the separation of hydrogen all take place in a single unit [10]. This allows for significant reduction of the number of equipment, and their size (and therefore reduction of CAPEX). Moreover, the extraction of hydrogen from the reaction environment affects the reaction equilibrium. The shift of equilibrium towards the products, allows operation at much lower temperatures (450 – 600 °C) for the same hydrogen yield (thus reduction of OPEX). The membrane reactor concept opens a new window for small-scale reformers, which is ideal for the production of hydrogen from a decentralised source such as biogas (see Figure 1.2).

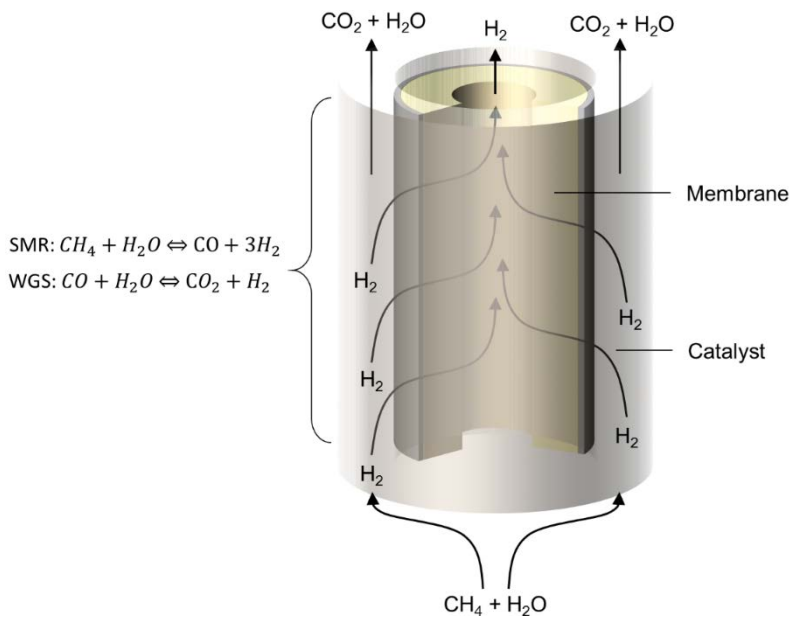


Figure 1.2. Schematic representation of a membrane reactor for H_2 production by methane steam reforming.

1.5. The fluidized bed membrane reactor

Membrane reforming systems have been topic of study for the past 30 years. Its development went hand-in-hand with that of hydrogen perm-selective membranes. Dense metallic membranes have been central to this, due to their unique separation mechanism, resulting in ultra-high purity hydrogen [11]. By decreasing the thickness of the membrane barrier, the hydrogen flux was increased, significantly improving reactor performance and reducing the required membrane area. The first and most studies of the membrane reformer were performed, for their simplicity, in packed-bed configuration [12]. In this configuration, the membrane is surrounded by the catalyst material. The main limitation in that case was the low flux through the membranes. As the permeation through the membranes increased over the years, the hydrodynamics and mass transfer characteristics inside the reactor start to play a significant role affecting the required membrane area. The separation of hydrogen is in this case not only limited by the membrane flux, but also by mass transport of hydrogen towards the membrane [13]. Moreover, as the extent of reaction kept increasing, the heat supply for the highly endothermic system became more and more difficult in packed bed configurations. To overcome these drawbacks of mass and heat transfer, new concepts were introduced, amongst them the fluidized bed membrane reactor. In a fluidized bed, unlike in the fixed state of a packed bed, the catalyst particles are in a dynamic fluid-like state, in which the membranes are immersed. This fluidization state is obtained when the drag forces of the gas on the particles overcome the net gravitational forces. The main advantages are considered to be: negligible pressure drop, (virtually) isothermal operation, improved fluidization due to compartmentalization of the bed by the membranes, resulting in bubble breakup which enhances mass transfer [14].

This thesis encompasses scientific research into the development of the process of steam reforming of biogas in a fluidized bed membrane reactor (see Figure 1.3). The work aims at the understanding of the workings of individual components, through integration and scale up, towards an understanding of the performance of the entire integrated system. In Chapter 2 the membranes, key to pure hydrogen production, are the topic of investigation. The stability and performance of the supported Palladium (Pd) membranes used in this work are

studied for long-term and under different process conditions. Chapter 3 investigates the effect of alloying of gold (Au) into the membranes to operate in an H_2S containing environment. As biogas is more than a mixture of methane and CO_2 , it also contains trace amounts of hydrogen sulfide (H_2S), which can have a strong interaction with the Pd-based membranes. In Chapter 4 membrane and catalyst are integrate in a reactive environment. The performance of a single membrane in a fluidized bed is investigated for the reforming of synthetic biogas. A one-dimensional fluidized bed reactor model is extended to account for the mass transport limitation towards the membrane. The experimental results are used to validate the presented model. In Chapter 5 effects of increasing system scale and membrane configuration on the performance is investigated. Two reactors with a much larger membrane area are experimentally demonstrated and the results are analysed with the developed reactor model. In Chapter 6 the knowledge obtained on the reactor level used in for a system analysis to obtain insight in the economics of biogas steam reforming in a fluidized bed membrane reactor. The results obtained and their implications for reforming towards renewable hydrogen are discussed.

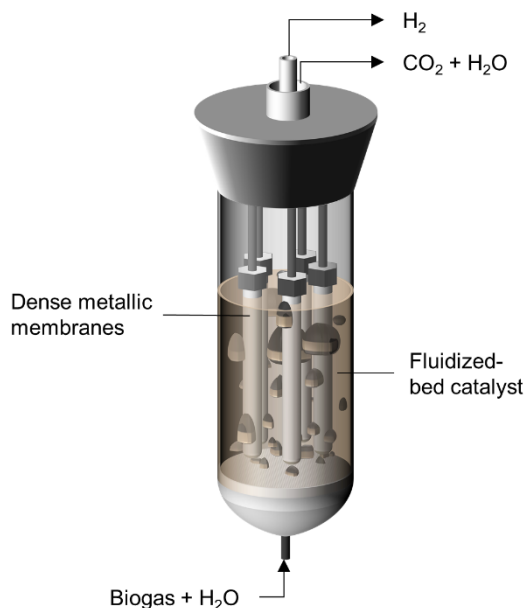
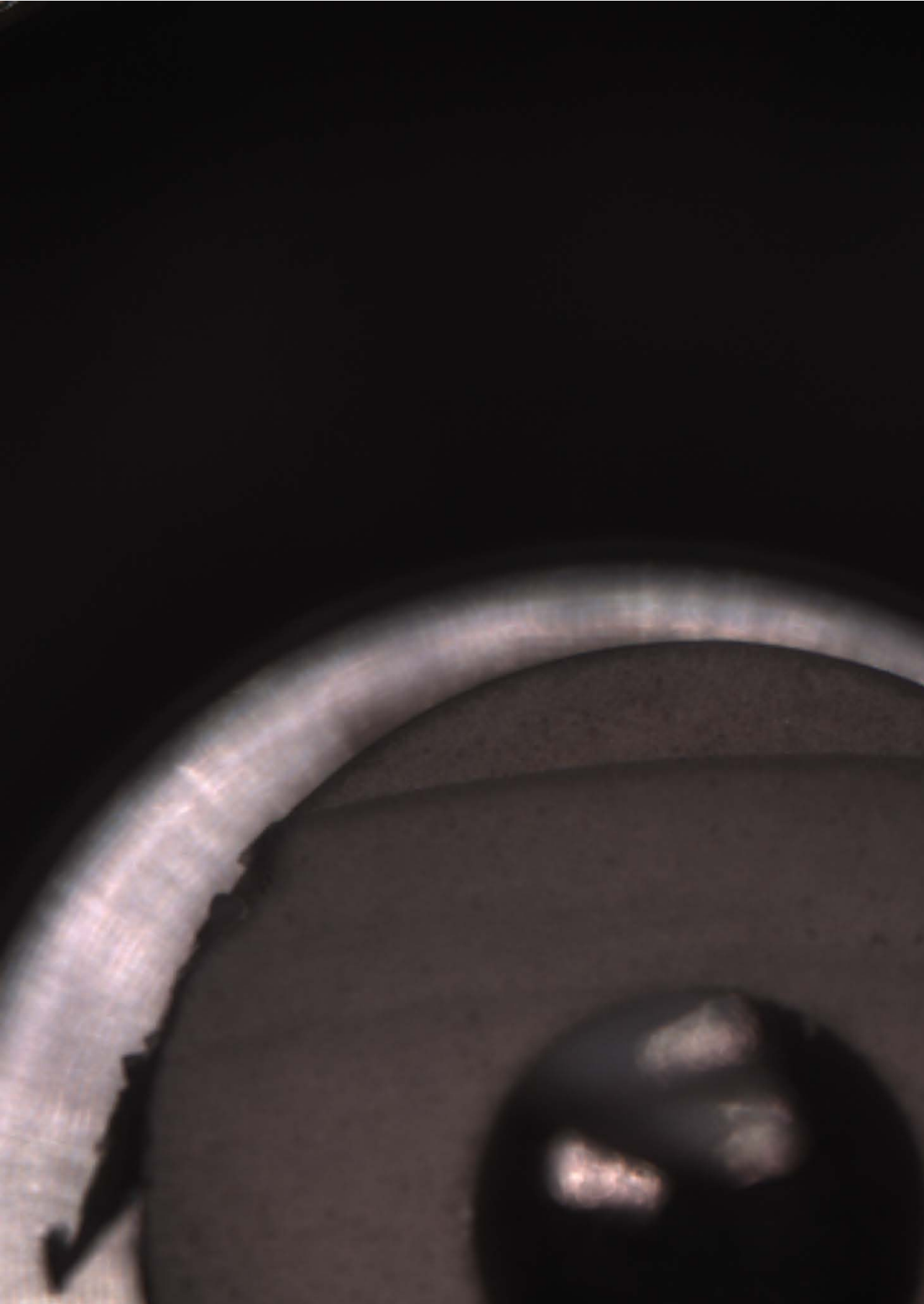


Figure 1.3. Schematic representation of fluidized bed membrane reactor concept for biogas steam reforming

References

- [1] B. Bryson, *A Short History of Nearly Everything*, 2003.
- [2] United Nations, *The Paris Agreement*, 2016.
- [3] Charles D. Keeling, The concentration and isotopic abundances of carbon dioxide in the atmosphere, *Tellus*. 12 (1960).
- [4] IPCC, *Special Report on Renewable Energy Sources and Climate Change Mitigation*, 2012. doi:10.5860/CHOICE.49-6309.
- [5] IEA, *World energy balances 2018*, 2018.
- [6] M. Tabatabaei, M. Aghbashlo, E. Valijaniani, H. Kazemi Shariat Panahi, A.S. Nizami, H. Ghanavati, et al., A comprehensive review on recent biological innovations to improve biogas production, Part 2: Mainstream and downstream strategies, *Renew. Energy*. 146 (2020) 1392–1407. doi:10.1016/j.renene.2019.07.047.
- [7] H.J. Alves, C. Bley Junior, R.R. Niklevicz, E.P. Frigo, M.S. Frigo, C.H. Coimbra-Araújo, Overview of hydrogen production technologies from biogas and the applications in fuel cells, *Int. J. Hydrogen Energy*. 38 (2013) 5215–5225. doi:10.1016/j.ijhydene.2013.02.057.
- [8] N. Muradov, F. Smith, A. T-Raissi, Hydrogen production by catalytic processing of renewable methane-rich gases, *Int. J. Hydrogen Energy*. (2008). doi:10.1016/j.ijhydene.2008.02.026.
- [9] S.D. Angeli, G. Monteleone, A. Giaconia, A.A. Lemonidou, State-of-the-art catalysts for CH₄ steam reforming at low temperature, *Int. J. Hydrogen Energy*. 39 (2014) 1979–1997. doi:10.1016/j.ijhydene.2013.12.001.
- [10] F. Gallucci, E. Fernandez, P. Corengia, M. van Sint Annaland, Recent advances on membranes and membrane reactors for hydrogen production, *Chem. Eng. Sci.* 92 (2013) 40–66. doi:10.1016/j.ces.2013.01.008.
- [11] M. V. Mundschau, X. Xie, C.R. Evenson IV, A.F. Sammells, Dense inorganic membranes for production of hydrogen from methane and coal with carbon

- dioxide sequestration, *Catal. Today.* 118 (2006) 12–23. doi:10.1016/j.cattod.2006.01.042.
- [12] A. Arratibel Plazaola, D.A. Pacheco Tanaka, M. Van Sint Annaland, F. Gallucci, Recent Advances in Pd-Based Membranes for Membrane Reactors, *Molecules.* 22 (2017) 1–53. doi:10.3390/molecules22010051.
- [13] T.P. Tiemersma, C.S. Patil, M. van Sint Annaland, J.A.M. Kuipers, Modelling of packed bed membrane reactors for autothermal production of ultrapure hydrogen, *61* (2006) 1602–1616. doi:10.1016/j.ces.2005.10.004.
- [14] S.A.R.K. Deshmukh, S. Heinrich, L. Mörl, M. van Sint Annaland, J.A.M. Kuipers, Membrane assisted fluidized bed reactors: Potentials and hurdles, *Chem. Eng. Sci.* 62 (2007) 416–436. doi:10.1016/j.ces.2006.08.062.



Chapter

Two

Stability of thin-film Pd-based supported membranes

Membrane reactors have demonstrated large potential for the production of hydrogen via reforming of different feedstocks. The long-term performance and stability of the membranes are extremely important for the possible industrial exploitation of this type of reactors. This chapter investigates the long-term stability of thin-film Pd-Ag membranes supported on porous Al₂O₃ supports. The stability of five (similarly prepared membranes) have been investigated for 2650 hours, at up to 600 °C and under fluidization conditions. Results show the importance and the contribution of the sealing to the (loss of) membrane selectivity. At higher temperatures deformation of the membrane surface results in pinhole formation and consequent decrease in selectivity. Stable operation of the membranes in a fluidized bed is observed up to 450 °C, however, at higher temperatures the abrasive action of the particles under fluidization causes significant deformation of the palladium surface resulting in a decreased selectivity.

This chapter is based on the following paper:

N.C.A. de Nooijer, A. Arratibel Plazaola, J. Melendez Rey, E. Fernandez, D.A. Pacheco Tanaka, M. van Sint Annaland, F. Gallucci. "Long-term stability of thin-film Pd-based supported membranes", *Processes*, 7 – 2 (2019), 106

2.1. Introduction

Palladium-based membrane technology has shown great potential in improving the reforming efficiency and intensifying reforming processes. The membranes can either be applied as a downstream separation step for hydrogen purification or integrated with the catalyst in a membrane reactor, in which hydrogen production and separation are combined in one single unit [1]. Membrane reactors are mostly studied in two different configurations, viz. (micro) packed bed (PB) and fluidized bed (FB) reactors. The membranes allow for the selective extraction of hydrogen from the reactor, shifting the equilibrium, thereby resulting in a higher conversion at lower temperatures (and consequently higher efficiency) compared to conventional reactors. This also produces a stream of pure hydrogen directly from the reactor without the need for down-stream separation units. Long-term stable production of pure hydrogen is therefore imperative to make the concept of membrane reactors industrially interesting. The performance of a membrane reactor depends largely on the flux of hydrogen extracted and on the purity of the hydrogen produced. The stability of a membrane is here considered as the ability of a membrane to maintain a constant flux of hydrogen as well as a constant perm-selectivity over time.

The performance of different membranes and membrane reactors configurations has been reported in literature. Full conversion of the feedstock as well as a high hydrogen recovery through the membranes with production of pure hydrogen have been reported [2]. Unfortunately, very few works have focused on the long-term stability of the system and the durability of the membranes, which is an important aspect for the Pd-based membrane reactors to become a viable technology.

The stability of membranes in steam reforming was studied in the work of Uemiya et al. published in 1991 [3]. Hydrogen production with a steam reforming Pd-membrane reactor was investigated and a constant permeation for at least 10 hours was reported, whereas in previous works a decrease in the permeation was reported because of the formation of carbon on the membrane [4–6]. Other works also reported a decrease in the hydrogen permeation, also under non-reactive conditions, i.e. when using either pure hydrogen or hydrogen/nitrogen gas

mixtures. Okazaki et al. reported a decrease in the hydrogen permeation above 600 °C due to the strong interaction between the alumina support and the Pd-layer [7]. Fernandez et al. observed a strong interaction also between the TiO₂ support of a catalyst and the Pd-membrane [8]. The works of Okazaki and Fernandez c.s. clearly indicate that the materials that come into contact with the membrane should be carefully selected.

Since the flux increases with a decrease in the membrane layer thickness, membrane research has focused on producing thinner selective layers. For self-supported membranes this has resulted in a reduction of mechanical stability. Recent work of Peters et al. has shown that even 200 µm wide channels do not provide sufficient mechanical support to the membrane to withstand the desired high pressure differences; a 12.5 µm palladium-silver layer deformed over time at 550 °C and 6 bar and started to form cracks reducing the perm-selectivity of the membrane [9]. Supported membranes have the advantage of maintaining a high mechanical stability for a very thin membrane layer. Metallic and ceramic supported Pd-based membranes have been prepared by various methods yielding a wide range of permeances and perm-selectivities [2].

Table 2.1 presents a summary of membrane reformer tests published in the literature that reported the duration and results regarding the stability of the membranes. In most of these works, a decreased perm-selectivity or deterioration of the membrane performance was reported. However, a wide variety of causes has been indicated. A better and more quantitative understanding of the rates and causes of the membrane instability and decrease in the perm-selectivity and hydrogen flux will help manufacturing better membranes as well as improving their design to enable durable operation of the membrane reactor.

This chapter investigates the stability of Pd-Ag thin-film membranes on ceramic supports for their application in a fluidized bed membrane reactor. The long-term stability of the Pd-Ag membranes was measured for up to 2750 hours at 550 °C. These results were used as a reference to study the stability of the membrane sealing, as well as the contribution of the formation of leakages at high temperatures up to 600 °C and under fluidization conditions.

Table 2.1. Stability results in literature for membrane reformers.

Reactor configuration	Feed	Membrane	Membrane thickness μm	Temperature $^{\circ}\text{C}$	Pressure bar	Time (h)	Stability results	H ₂ Purity %	Source
PB	CH ₄	Pd glass support	20	350 – 500	1 - 9	10	<ul style="list-style-type: none"> ○ Stable ○ Previous works had carbon on membrane. 	-	[3]
PB	Ethanol	Pd and PdCu	1.3 and 2	280 - 360	1	45	<ul style="list-style-type: none"> ○ Decrease in permeance in first 20 hours. ○ Pinholes and carbon on the Pd membr. After the test (SEM) ○ Few openings after the test (SEM). ○ Both membranes retained bulk integrity. 	100	[6]
PB	methanol	Pd/Al ₂ O ₃	~7	280 - 330	1.5 – 2.5	1000	<ul style="list-style-type: none"> ○ Decrease in ideal perm selectivity 6000 to 4300 (H₂/N₂) 	~100	[10]
PB	Methanol	Pd (support not specified)	24.3	200 - 300	1 – 3.44	36	<ul style="list-style-type: none"> ○ Deteriorated membrane surface, may be attributed to hydrogen embrittlement. ○ Visible carbon deposition. 	-	[5]
PB	CH ₄	PdRu (PSS/YSZ)	5	~580	29	1000	<ul style="list-style-type: none"> ○ Stable CH₄ conversion ○ Relatively stable H₂ recovery ○ Decline in H₂ purity ○ 20% reduction of H₂ flux due to coking. ○ Nitrogen leak increased two orders of magnitude. ○ Defects over the entire surface. 	>93	[11]

PB	CH ₄ /CO ₂	Pd/Al ₂ O ₃	~10	380 - 450	2.5 - 3.5	1000	<ul style="list-style-type: none"> o Decrease in ideal perm selectivity 4300 – 1000 (H₂/N₂). o Formation of pinholes and sintering on the membrane o Catalyst deactivation. 	96 - 70	[12]
PB	CH ₄	Pd/Al ₂ O ₃	~3.8	580	28	1100	<ul style="list-style-type: none"> o Carbon formation found on catalyst. o Increase of leak flow o Membrane selectivity decreased 18 times 	92-86	[13]
PB	NG	Pd stainless steel supported	20	495 - 540	9	3310	<ul style="list-style-type: none"> o Replacement of membranes was required after 492 hours due to leakages. o After replacement H₂ purity remained >99.99% o Increase of impurities after 2100 hours. 	>99.99	[14]
FB	CH ₄	PdAg (Inconel)	3 + 1.5 out + in	500 - 630	2.0 - 5.3	260	<ul style="list-style-type: none"> o Overall properties of the membrane were not altered. 	-	[15]
FB	EtOH	PdAg/Al ₂ O ₃	~3-4	450 - 550	2 - 4	50	<ul style="list-style-type: none"> o Test stopped due to failure on sealing. 	-	[16]

2.2. Experimental

2.2.1. Membrane preparation

The membranes investigated in this study are thin-film palladium-silver membranes prepared by electroless plating on 100 nm asymmetric Al_2O_3 tubular supports provided by Rauschert Kloster Veilsdorf. Different support dimensions were used, as shown in Figure 2.1, in particular 10/4 mm and 14/7 mm outer/inner diameter (OD/ID). These supports were used in two different configurations, viz. with both sides open and with one side closed (referred to as “finger-like” supports). The finger-like shape is also porous and further covered by the palladium/silver selective layer. Ceramic substrates were activated by immersion into a palladium acetate solution with a subsequent co-deposition of a Pd-Ag layer following the method by Pacheco Tanaka et al. [17]. The palladium concentration was modified according to the dimensions of the supports and the electroless plating process was carried out for 5 hours for each membrane. Only membrane 5 (shown in Table 2.2) had 6 hours of deposition. Palladium silver compositions were calculated after analysis of the samples taken from the ELP solution. The results of the characterization carried out by ICP-OES are summarized in Table 2.2. After the plating step, the metallic layer was annealed at 550 °C for 4 h in a reducing atmosphere (10% H_2 and 90% N_2).

Table 2.2. Membranes used in this study with electroless plating time and solution composition.

Membrane	ELP time (h)	Pd%	Ag%
1	5	94.70	5.30
2	5	94.83	5.17
3	5	95.08	4.92
4	5	95.07	4.93
5	6	92.42	7.58

The membranes were sized and sealed using the Swagelok sealing method developed by Fernandez et al. for 10/7 mm outer/inner diameter (OD/ID) [8] as also applied in other studies ([16] and [18] for 10/4 and 14/7 mm supports respectively).



Figure 2.1. Sealed membranes with a cross-section; from left to right: a 14/7 mm OD/ID membrane, a 10/4 mm OD/ID membrane and a 14/7 mm OD/ID finger-like membrane.

2.2.2. Permeation modules

Three module configurations were used to study the stability of the membranes (Figure 2.2), using the same feed and outlet control and analysis systems (one module per time can be used in the permeation setup). The feeding of hydrogen, nitrogen and air (or a mixture of them) was controlled by Bronkhorst mass flow controllers. Membrane module configuration A allows testing of 5 membranes at once in a single permeation module; this ensured that all the membranes were exposed to exactly the same operating conditions. The permeate of each of the 5 membranes can be measured individually. Configuration B is a permeation module for the testing of a single membrane. This same module allows for the integration of the membrane in a fluidized bed, as shown in configuration C; the fluidized bed

material consisted of Rh/Al₂O₃ particles (provided by Johnson Matthey) with an average particle size of 180 μm. The pressure in the system was controlled using a backpressure regulator. The permeate flow rate from the membrane was measured using Horiba VP film flow meters. For the hydrogen flux the Horiba VP-4 (1-10 l/min) was used, whereas for the nitrogen flux the Horiba VP-1 was used (0.2-10 ml/min). In some cases, the nitrogen flow rate was below 0.2 ml/min, in which case the flux (for the calculation of the perm-selectivity) was set at 0.2 ml/min with the indication that the actual flux is smaller than this value.

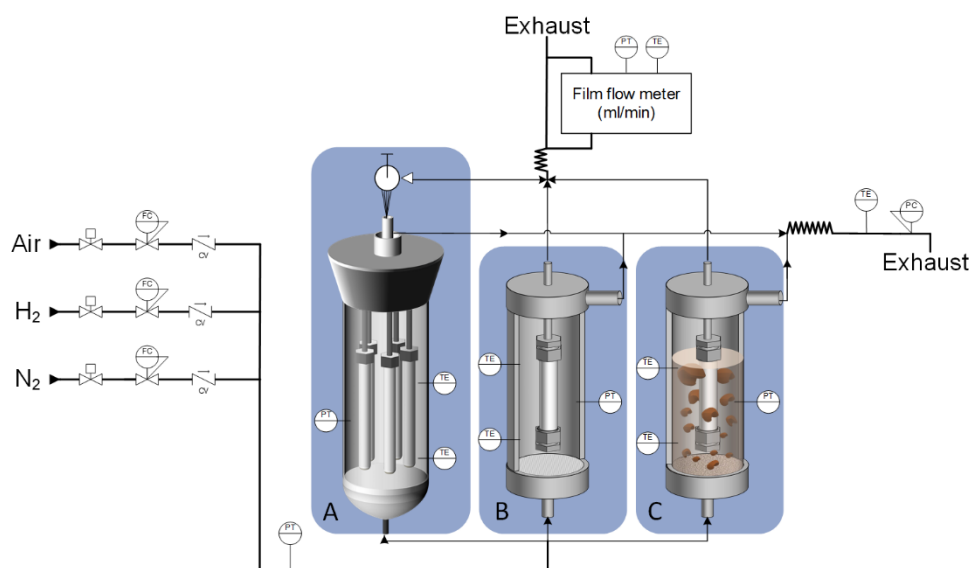


Figure 2.2. Schematic representation of the permeation modules used in this study.

2.2.3. Long-term stability tests

The stability of five membranes was studied using configuration A. Membranes 1 and 2 prepared on 14/7 (OD/ID) supports were cut in two parts (indicated with 1a, 1b and 2a, 2b respectively) in order to investigate the stability evolution of two equally prepared membranes. Membrane 2a had a finger-like part; this membrane was used to investigate the effect of the membrane sealing on the stability. Membrane 3 was prepared on a 10/4 support, and due to the lower thickness of the support, a lower torque was applied to seal this membrane. The five membranes were in total operated for 2000 hours. After 2000 hours,

membrane 1a and 2a were removed for intermediate characterization, while the other membranes were operated for another 750 hours. Membrane number 4 (10/4 OD/ID) was studied as a single membrane at high temperature. The membrane was stabilized at 400 °C for 150 hours and operated at 550 °C and 600 °C. Membrane 4b and 5, both finger-like, 10/4 (OD/ID) and 265 mm were sealed with the same torque. These membranes were used to study the influence of the fluidization on the permeation properties. The membranes were integrated into two separate reactors and stabilized at 400 °C for 150 hours. After this period, a catalyst bed was introduced into the reactor containing membrane 4b. The minimum fluidization velocity was experimentally determined with the standard pressure-drop method to ensure the fluidization velocity was set at 3 times the minimum fluidization velocity. Both membranes were first kept at 400 °C and after 700 hours the temperature was increased to 500 °C. The gas feed was a 50:50 mixture of nitrogen and hydrogen, the nitrogen ensured that the permeation of hydrogen did not decrease the fluidization velocity too much so that the fluidization velocity was kept well above the minimum fluidization velocity (although this induced external mass transfer limitations, which are not relevant for this study on the membrane stability and are not further discussed in this study). The membrane parts and experimental details are summarized in Table 2.3.

Table 2.3. Details of membranes and conditions used in this work.

Membrane Number	Reactor configuration	Support		Sealing		Length (mm)	Temperature (°C)	Time Tested (hours)	On Stream*
		Material	Size Ø Outer/inner (mm)	Top	Bottom				
1a	5 membranes Empty tube	Pd-Ag Al ₂ O ₃ 100 nm	14/7	Swagelok 12 Nm	Swagelok 12 Nm	105	400-525	2000	H ₂
1b	5 membranes Empty tube	Pd-Ag Al ₂ O ₃ 100 nm	14/7	Swagelok 12 Nm	Swagelok 12 Nm	90.5	400-550	2650	H ₂
2a	5 membranes Empty tube	Pd-Ag Al ₂ O ₃ 100 nm	14/7	Swagelok 12 Nm	Finger-like	112	400-525	2000	H ₂
2b	5 membranes Empty tube	Pd-Ag Al ₂ O ₃ 100 nm	14/7	Swagelok 14 Nm	Swagelok 14 Nm	75	400-550	2650	H ₂
3	5 membranes Empty tube	Pd-Ag Al ₂ O ₃ 100 nm	10/4	Swagelok 7 Nm	Swagelok 7 Nm	107.5	400-550	2650	H ₂
4a	Single membrane Empty tube	Pd-Ag Al ₂ O ₃ 100 nm	10/4	Swagelok 6 Nm	Swagelok 6 Nm	87.98	400-600	725	H ₂
4b	Single membrane Fluidized bed	Pd-Ag Al ₂ O ₃ 100 nm	10/4	Swagelok 6 Nm	Finger-like	265	400-500	1150	H ₂ /N ₂ (50:50)
5	Single membrane Empty tube	Pd-Ag Al ₂ O ₃ 100 nm	10/4	Swagelok 6 Nm	Finger-like	265	400-500	1150	H ₂ /N ₂ (50:50)

* "On stream" indicates the gas or gas mixture the membranes were exposed to when not being measured.

2.2.4. Membrane characterization

After the membranes were tested the systems were cooled down in nitrogen. When at room temperature the nitrogen flux was measured at different pressures and the membranes were removed from the system. The sealing parts were covered with a resin, to distinguish the leakage contribution of the sealing from the leakages from the surface, and subsequently the permeation of nitrogen was again measured (dry permeation). To obtain the pore sizes of the pinholes, capillary flow porometry was used. The membranes were immersed in ethanol and the nitrogen flux as a function of the pressure was measured (wet permeation). With the dry and wet permeation lines, the pore size of the pinholes was estimated using the Young-Laplace equation [19].

2.2.5. Post mortem characterization

After the flux characterization, the seals were removed and the membranes were characterized by X-Ray Diffraction (XRD), Scanning Electron Microscopy (SEM) and Energy Dispersive Spectroscopy (EDS). The XRD analysis was performed at 1.5406 Å, with the Rigaku Miniflex 600. SEM was performed on both a cross-section and the surface of the membranes, using secondary electrons and backscattered electrons, with a Phenom Pro X. The EDS was performed on the same system as the SEM at 15kV.

2.3. Results and discussions

In order to integrate the membranes in the reactors, each membrane was connected to a dense metallic tube using Swagelok and graphite seals. The mechanical stress that can be induced on the membranes by the Swagelok sealing method is found to be limited by the support and could result in failure of the membrane sealing during operation. The 10/4 supports used in this work allow for sealing with a higher torque than used on the 10/7 mm OD/ID membranes presented in the work of Fernandez et al [8]. However, Spallina et al. used also 10/4 supports and reported significant failure of the membranes [16]. For the sealing of the membranes in this work it was found that the torque applied on the 10/4 supports could be increased compared to the 10/7 membranes. The 14/7 mm OD/ID support was found to withstand a sealing torque exceeding 20 Nm.

However, at this torque level the membrane showed damage to the thin palladium film, therefore the maximum torque applied in this work was set to 14 Nm. All membranes investigated in this work were leak tested prior to other tests. The quality of the sealing can be considered as a potential contribution to the decrease in perm-selectivity of the membranes. Thus, a reduction in the number of sealing points could improve the stability of the membrane. In this work finger-like membranes were used where the end cap of the membrane is completely covered with the palladium layer. The end cap is made of a porous ceramic part formed during the support production and therefore also contributing to the total surface area of the membrane [20].

2.3.1. Air treatment and initial conditions

Air treatment is usually performed to stabilize and increase the hydrogen flux [21–23]. Roa et al. have shown that the air treatment had more than a cleaning effect on the surface of the membranes and also caused morphological changes of the surface [24]. However, it has been reported that air treatment also increased the nitrogen flux indicating the formation of pinholes. The membranes in this work were heated up to the desired temperatures under nitrogen; at this temperature, the nitrogen permeation was measured followed by an air treatment. The air treatment was performed by flushing a 50:50 air/nitrogen mixture into the system for 2 minutes; for membranes 1a, 1b, 2a, 2b and 3 at 500 °C, and for membranes 4a, 4b and 5 at 400 °C respectively. After the treatment, the nitrogen and hydrogen flux were again measured. The obtained permeation results are reported in Figure 2.3.

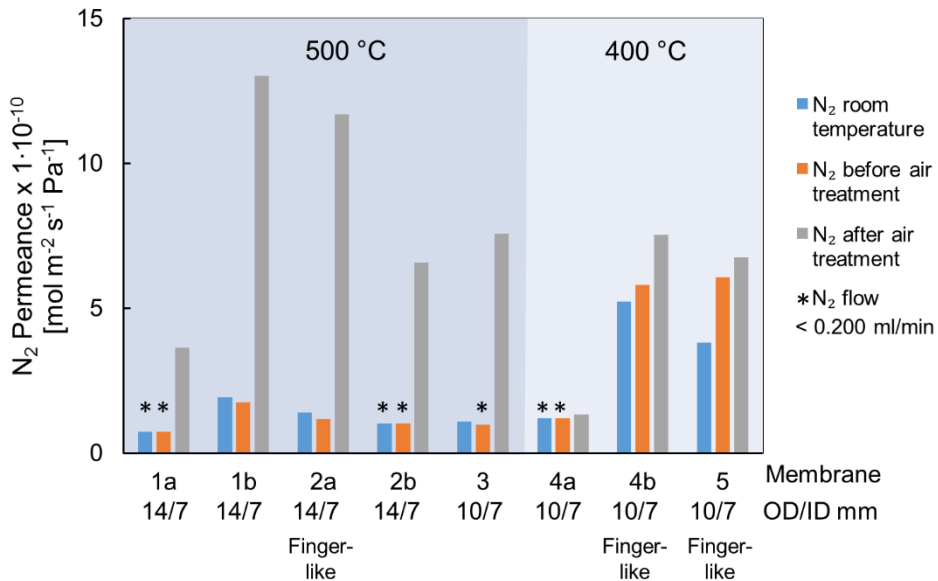


Figure 2.3. Nitrogen permeance before and after heating and air treatment.

The results show that the nitrogen permeance after the air treatment increases between 400% and 700% at 500 °C, which is significantly more than the 10% to 30% at 400 °C. The increase in nitrogen permeance could be the result of a rearrangement of the palladium surface because of oxidation, which may cause defects. The formation and connection of defects through the palladium layer as a result of this rearrangement could subsequently result in the formation of pinholes. The results show that this effect is more pronounced at higher temperatures. This can be related to the higher reaction kinetics of palladium oxidation at higher temperatures, which results in a faster and less structured rearrangement [25]. The air treatment did not show significantly different effects for the finger-like membrane compared to the other membranes, indicating that the graphite ferrules in the sealing are not significantly affected by the air treatment, both at 400 °C and 500 °C. The hydrogen flux increased from 70% up to 110% compared to the case before the air treatment; this is expected and comparable to the increases reported before in the literature [21]. The ideal permselectivity ranged, after the air activation, between 7500 and 9000 at 500 °C for these membranes. The results of the permeation test for all the membranes at their initial conditions are shown in Figure 2.4. The permeation flux of all

membranes after activation showed good correspondence with the transmembrane difference of the square root of the hydrogen partial pressure, indicating that the hydrogen flux is only limited by bulk diffusion of hydrogen in the palladium layer. Both parts of membrane 1 and 2 showed almost the same hydrogen permeance, whereas the permeance of membrane number 3 was found to be 1.2 times higher than that of membrane 1 and 2. We can relate this difference to a minor difference in the (thickness of the) selective layer and not to differences in the dimensions of the support, since the pressure exponent showed a good fit with 0.5 for all membranes, indicating no effect of the support. Membrane 4 showed a higher permeance compared to membrane 5, which can be explained by the longer time of the ELP process of membrane 5 which resulted in a slightly thicker Pd-Ag layer, lowering the hydrogen permeance.

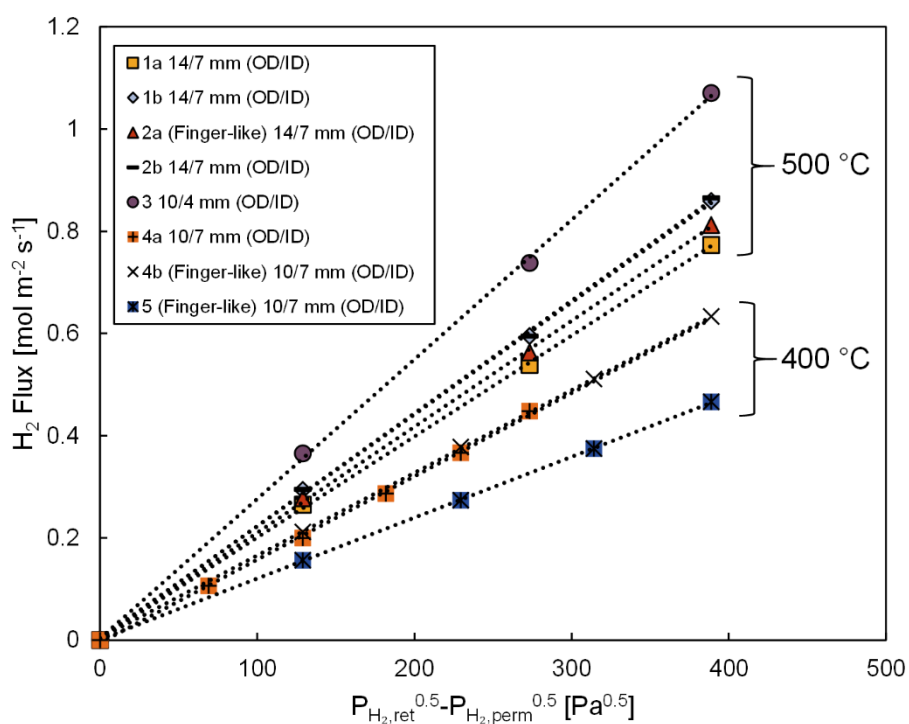


Figure 2.4. Initial hydrogen permeance of the membranes as measured after air activation.

2.3.2. Long-term stability

Membranes 1a, 1b, 2a, 2b and 3 were studied to compare the different seals and sealing forces. The long-term behaviour of these membranes was investigated at 500 °C, 525 °C and 550 °C using setup configuration A. Both the hydrogen and nitrogen permeances are measured over the tested time, and are shown in Figure 2.5 and Figure 2.6, respectively. The hydrogen permeance initially increased, however after 200 hours it stabilized for membranes 1a, 1b, 2a and 2b. This process was shown to be faster for membrane 3. This initial increase is understood as a period of further annealing of the membrane. After this initial increase the hydrogen permeance decreased for all the membranes, however, for membrane 3 it decreased more significantly. The hydrogen permeance stabilized after ca. 1000 hours. At this point the temperature was increased to 525 °C, and an increase in the hydrogen permeability as a result of the increased temperature is observed. This is followed with a similar initial increase over time as seen at 500 °C followed by a decrease, which then again stabilizes. Once again, for membrane 3 the process is more pronounced and faster. After 2000 hours on stream, the system was cooled down and membrane 1a and 2a were removed. After heating up the system, the remaining membranes showed a stable hydrogen permeance. Following the stable period, the system was heated further to 550 °C. At this temperature a direct decrease in the hydrogen permeance was measured. After 2750 hours the test was stopped in order to analyse the membranes. The effects of the high operating temperature of 550 °C and above are further investigated using membrane 4a.

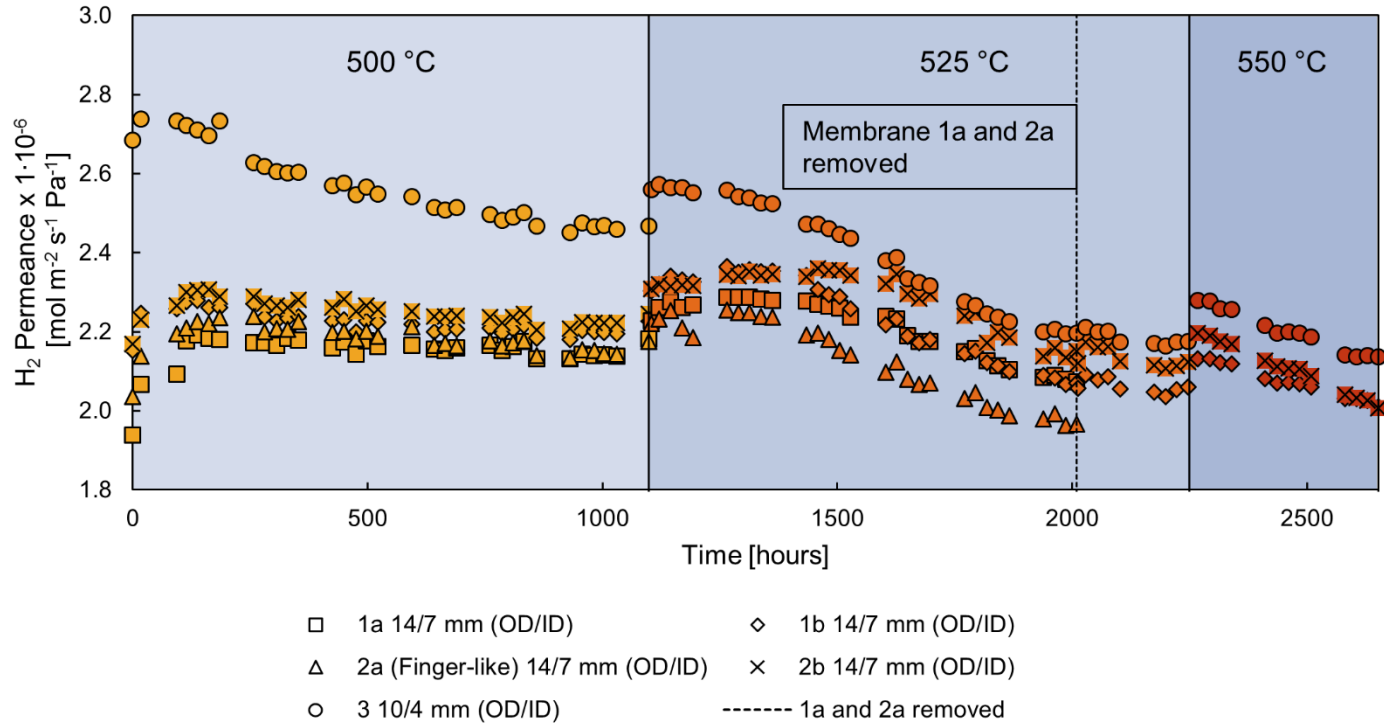


Figure 2.5. Long-term hydrogen permeance of membranes 1a, 1b, 2a, 2b and 3 at 500 °C, 525 °C and 550 °C.

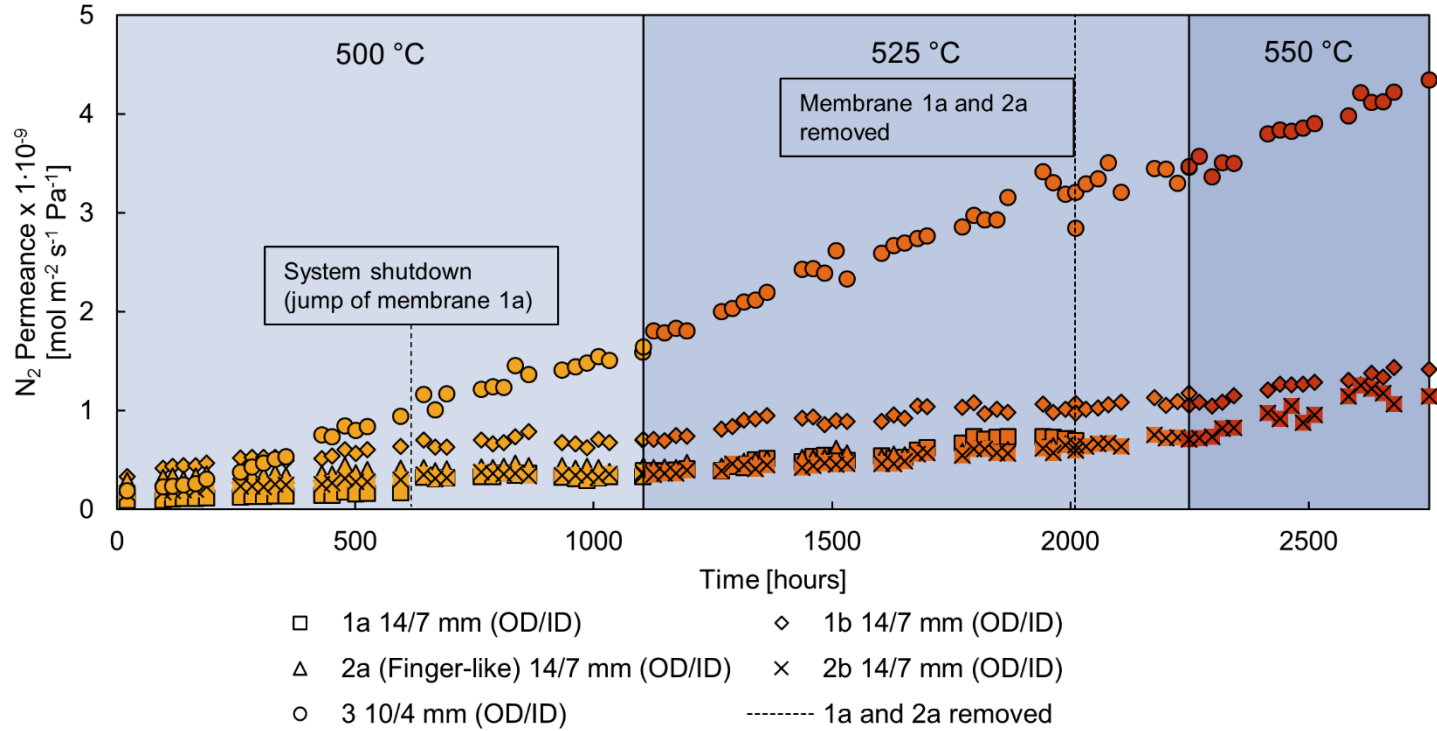


Figure 2.6. Long-term nitrogen permeance of membranes 1a, 1b, 2a, 2b and 3 at 500 °C, 525 °C and 550 °C.

The increase in nitrogen permeation follows a linear trend over time for all the membranes. However, membrane 3 shows a more pronounced increase in the nitrogen permeance. Due to a shutdown of the system (at around 600 hr), membrane 1a made a small jump up in nitrogen permeance. The other membranes seemed to be unaffected by this shutdown. The ideal perm-selectivity ranged after the long-term test from 755 to 3100 at 550 °C for membrane 1b, 2b and 3.

To further compare the long-term behaviour of the membranes both the time derivative of the hydrogen and nitrogen permeance were calculated and compared for each temperature (see Figure 2.7). In the calculations of the slopes the initial increase was not considered for the hydrogen permeation. The hydrogen permeance has a negative slope as the permeation decreases over time; it is clear that the slopes become more significant at higher temperatures. The decrease in hydrogen permeability is possibly related to surface deformation, of which the rate is increased at higher temperatures [26]. The surface transformations are further investigated in the post characterization.

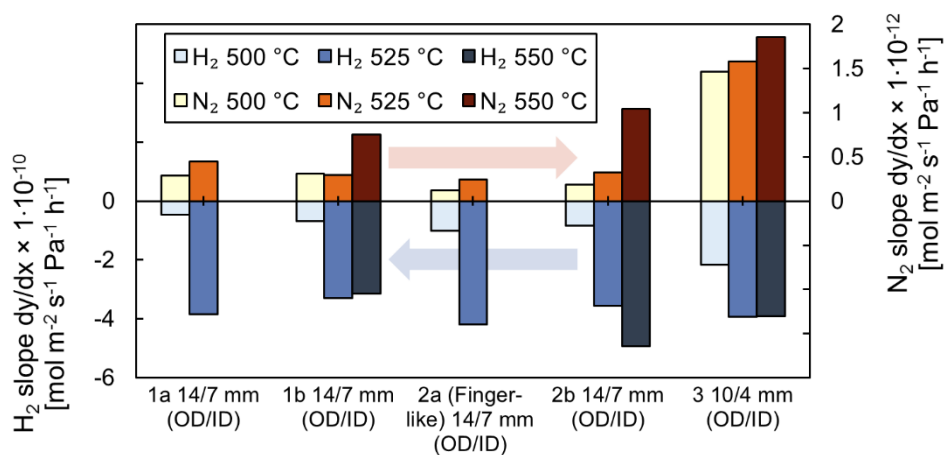


Figure 2.7. Slope of hydrogen and nitrogen permeance over time.

The slopes of the nitrogen permeance of the tested membranes are relatively small compared to literature. Abu El Hawa reported slopes of $4 \cdot 10^{-11}$ down to $5 \cdot 10^{-12}$ mol m⁻² s⁻¹ Pa⁻¹ h⁻¹ for metallic supported membranes with a 30 μm layer of YSZ [27]. With an increase in the temperature the slope of the nitrogen

permeance increases almost for all the membranes. Membrane 2a (finger-like) shows the lowest increase in nitrogen permeation due to the fact that this membrane has only one sealing. To further investigate this, the relative nitrogen permeance was determined by dividing the nitrogen permeance by the initial nitrogen permeance, which is shown in Figure 2.8. These results show that the relative nitrogen permeance of membrane 2a is half that of membrane 2b (which was originally part of the same membrane but has now two sealings), also membrane 1a shows that the relative nitrogen permeance is doubled compared to membrane 1b. This indicates that the main contribution of the nitrogen permeance increase over time is related to the sealing. Thus, also the larger increase in the nitrogen permeance through membrane 3 can be suspected to be caused by the lower force applied on the sealing. At 525 °C this effect was less pronounced, which could indicate an increased contribution of leakages through pinholes formed on the surface. If the surface contribution increases the effect of the sealings become less pronounced.

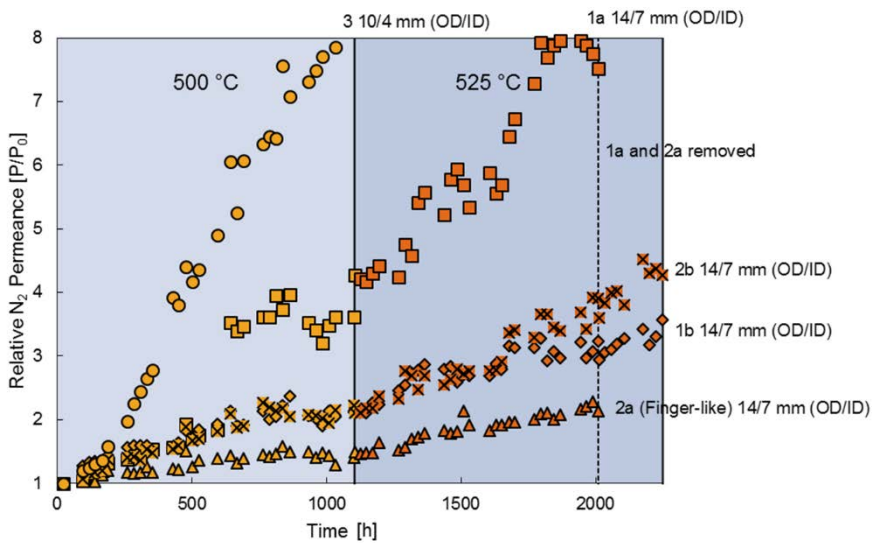


Figure 2.8. Relative nitrogen permeance of the membranes 1a to 3 in the long-term membrane test.

2.3.3. High temperature stability

To investigate the membrane stability at temperatures above 550 °C membrane 4a was used. The hydrogen permeance increases with temperature; at 500 °C

this increase is more pronounced due to the stabilization of the Pd-Ag layer; the corresponding nitrogen permeance as well as the slope of nitrogen permeance are comparable to those observed for membrane 3 at both 500 °C and 550 °C. At 600 °C there is a very large decrease in the hydrogen permeance and a very pronounced increase in the nitrogen permeance, which eventually resulted in membrane failure (i.e. ideal perm-selectivity <500). The decrease in hydrogen flux was expected, since at 600 °C there is a strong interaction between the alumina support and the palladium layer [7]. A similar increase in the nitrogen permeation was observed after 150 hours at 600 °C in single gas conditions for a Pd_{94.9}Ag_{5.1} membrane by Melendez et al. [28]. The main purpose of the high temperature stability test in this work is to differentiate between different effects that cause the increase in the nitrogen permeance, which is further discussed in the post characterization section.

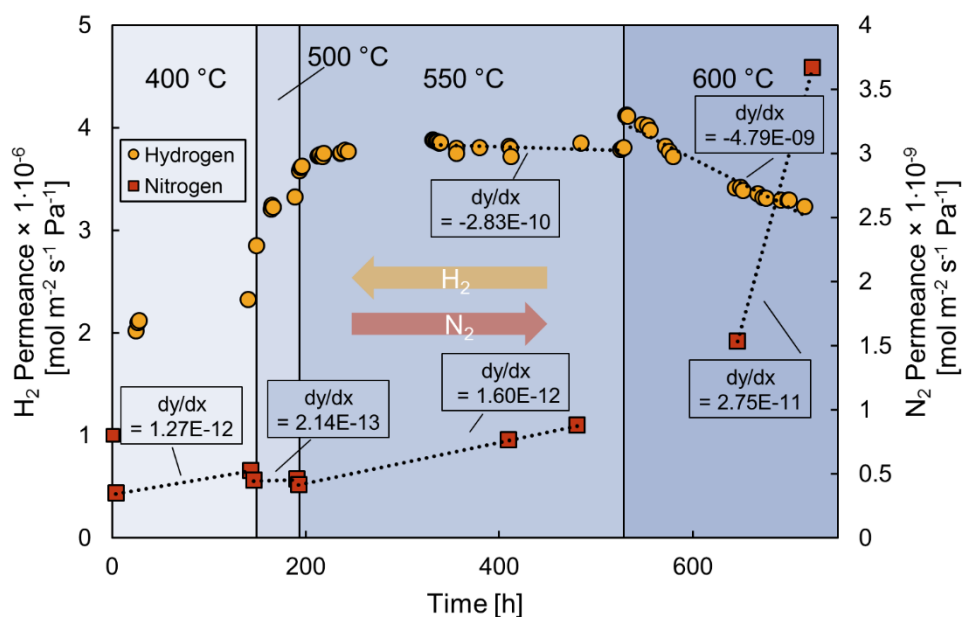


Figure 2.9. Effect of temperature on the long-term hydrogen and nitrogen permeance of membrane 4a.

2.3.4. Fluidization conditions

In order to study the effect of fluidization on the hydrogen and nitrogen permeation, two similar finger-like membranes, 4b and 5, were integrated in two

identical reactors and the nitrogen and hydrogen permeances were measured. Both membranes were activated with an air treatment and were subsequently stabilized at 400 °C. Both membranes showed a similar performance and stability, as can be seen from Figure 2.10 and Figure 2.11 showing the hydrogen and nitrogen permeance respectively. Membrane 4b exhibited a somewhat higher initial hydrogen permeance, whereas the nitrogen permeance for both membranes were similar. After the stabilization period the systems were cooled, the catalyst bed was introduced into the system of membrane 4b and both systems were heated back up. After heating up, membrane 4b showed a small step increase in the hydrogen permeance, whereas membrane 5 showed a step decrease; the increase in hydrogen permeance of membrane 4b could be explained by a higher average temperature in the system; the temperature profile along membrane 4b in the fluidized bed became more uniform and hence a higher permeation was obtained. The step decrease can be related to a deactivation of the palladium layer during the cool-down cycle, however this behaviour is normally not observed for these membranes when cooled down and heated back up. The nitrogen permeation is also affected by the cool-down and the integration of the catalyst. During fluidization, membrane 4b showed a decrease in the hydrogen permeance during the first 250 h, after which a stable hydrogen permeance was obtained. The nitrogen permeance of membrane 4b decreased under fluidization, in contrast to all other experiments. It is suspected that both effects are the result of catalyst particles covering the membrane surface, covering the pinholes and reducing the surface area available for hydrogen adsorption. Membrane 5 exhibited a stable hydrogen and nitrogen permeance over this period. After 850 hours the system temperatures were increased to 500 °C. Both membranes showed an increased hydrogen permeance related to this temperature increase. Membrane 5 showed initially a decrease in the hydrogen permeance, which could be attributed to the change in temperature distribution along the membrane. Nevertheless, the temperature along membrane 4b in the fluidized bed was found to be stable and still an increase in the hydrogen permeance was observed. Taking the nitrogen permeance into account, a stable operation for membrane 5 was observed, whereas a large increase in the nitrogen permeance was observed for membrane 4b. From these results it can be concluded that the membrane and sealing was significantly affected by the presence of the fluidized bed at 500 °C. To investigate

whether the extent of the leakages increases gradually with higher operating temperature, or whether there is a strong increase at a certain temperature, membrane 5 was resealed after post characterization, placed in the fluidized bed and then tested again at 450 °C and 500 °C under the same conditions as for membrane 4b before (results are not shown in the figure, since the time scales were shorter). The nitrogen slope at 450 °C was found to be $4.8 \cdot 10^{-13} \text{ mol m}^{-2} \text{ s}^{-1} \text{ Pa}^{-1} \text{ h}^{-1}$ and at 500 °C $1.5 \cdot 10^{-11} \text{ mol m}^{-2} \text{ s}^{-1} \text{ Pa}^{-1} \text{ h}^{-1}$. The nitrogen permeation increased with a factor 3 between 400 °C and 450 °C, while it increased with a factor 31 when going from 450 °C to 500 °C. These results suggest a critical change between 450 °C and 500 °C, where the leak rate increases significantly. Post characterization of the membranes was performed in order to understand the main contribution to the membrane failure.

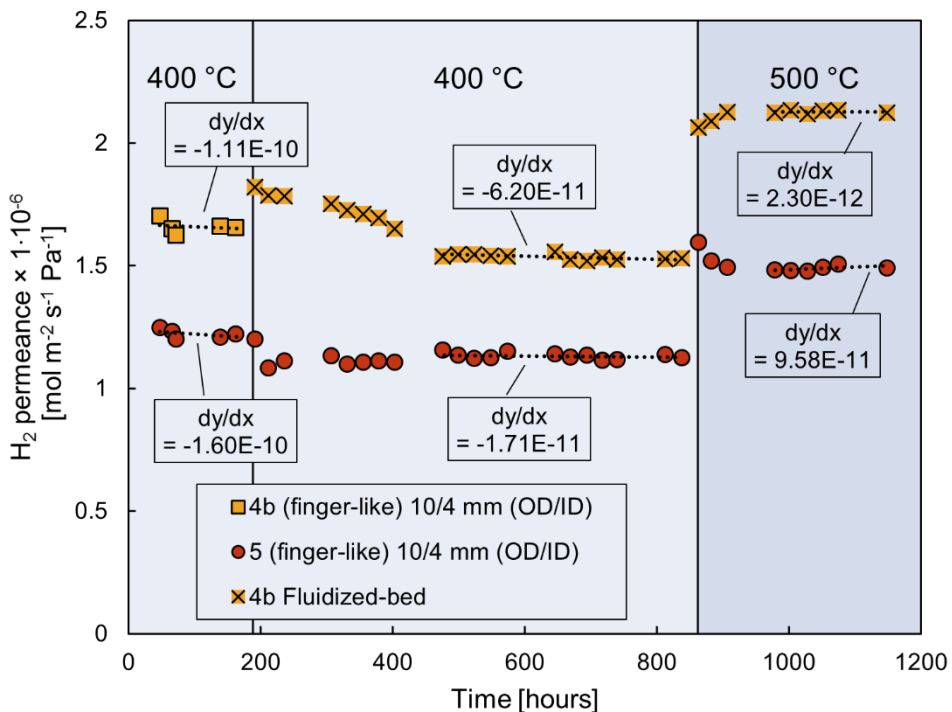


Figure 2.10. Hydrogen permeance of membrane 4b in the fluidized bed and membrane 5 in the empty system.

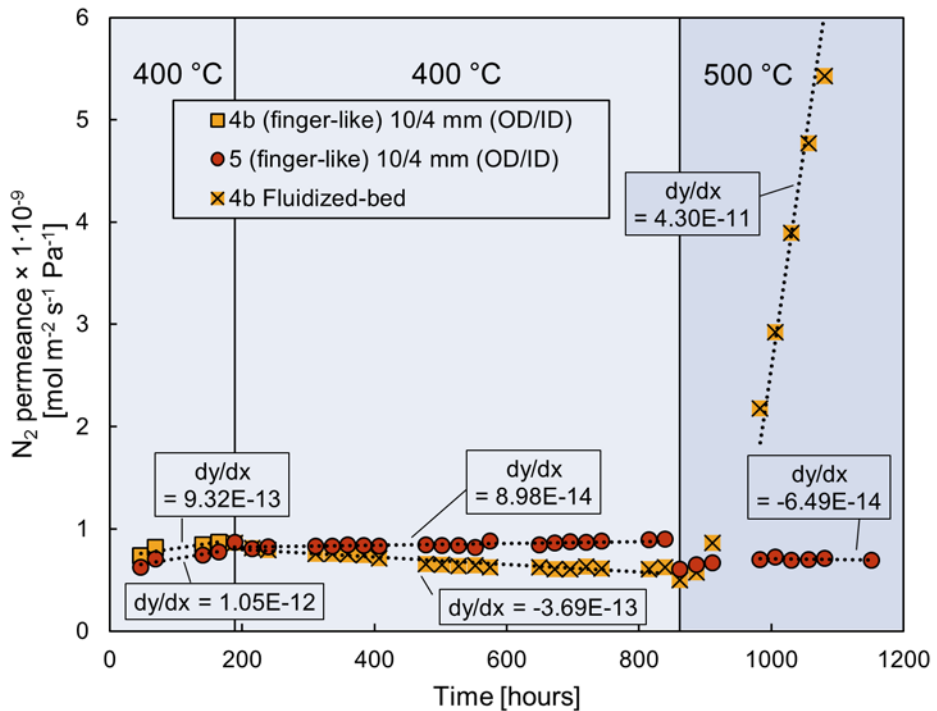


Figure 2.11. Nitrogen permeance of membrane 4b in the fluidized bed and membrane 5 in the empty reactor.

2.3.5. Post characterization

To better understand the origin of the increase in the nitrogen permeance of the tested membranes, capillary flow porometry was used (after closing the sealing parts by using a gas tight resin). The results of the capillary flow porometry are translated to pore sizes using the Young-Laplace equation; the results are shown in Figure 2.12. The pore distribution for membrane 4a could not be determined due to damage to the membrane while preparing the sample.

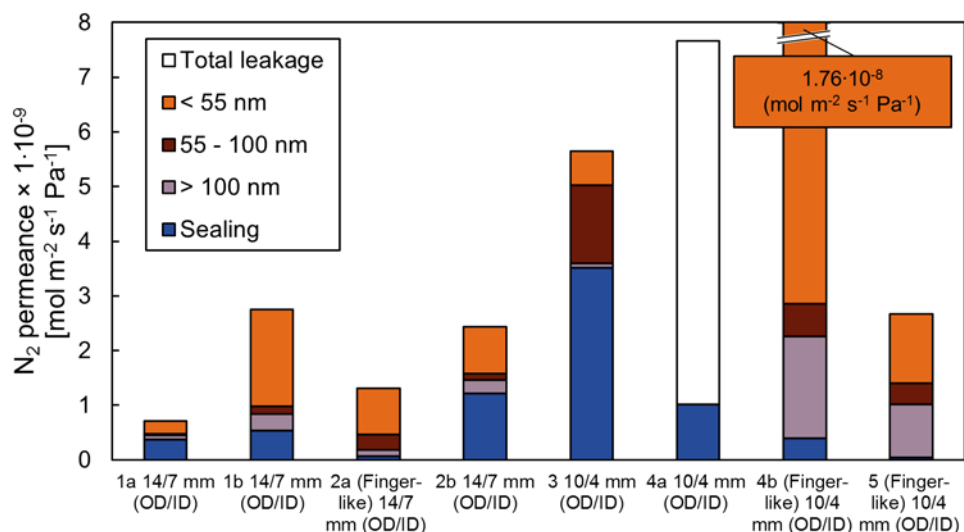


Figure 2.12. Nitrogen permeance contributions at room temperature, with corresponding pore size contributions

The blue part in the bars in Figure 2.12 shows which part was a result of leakages from the sealing. It is clear from the figure that the contribution of leakages from the sealing was the lowest for finger-like membranes 2a, 4b and 5 with only one sealing, which confirms the results obtained during the long-term stability tests that the sealing contributes partly to the nitrogen permeance and can be decreased by decreasing the number of sealings used. Moreover, it can be seen that the contribution of the sealing to the nitrogen permeance on membrane 3 was significantly higher because of the lower torque applied on the sealing. However, the increase in nitrogen permeation during the long-term stability test could also be related to the formation of large pores, as they show to have a significant contribution to the overall leakage rate as well. In membranes 1a, 1b, 2a and 2b most of the contribution is shown to result from pores with a size smaller than 55 nm. Membrane 4b and 5 show a large contribution of pores larger than 100 nm and pores smaller than 55 nm. The contribution of the large pores was expected for membranes 4b and 5 since minor pinholes were visible on the surface when the membrane was immersed in ethanol before the high temperature tests were carried out.

The different contributions to the nitrogen permeance of membrane 4b and 5 were studied in more detail to investigate whether the finger-like part of the membrane suffered more damage from the fluidization than other parts of the membrane. To this end, the membrane was immersed in increments of 1 cm in ethanol while the permeate side was pressurized with helium from the inside of the membrane. The helium flow rate was measured during the immersion. The pressure difference over the membranes was selected such that the ethanol closed all the pinholes during the test and that no bubbles were observed from the membrane surface. Figure 2.13 shows the distribution of the leakage rates along the membrane, where the relative-length 0.0 represents the tip of the finger-like membrane. From these results it can be observed that membrane 5 shows a relatively equal distribution along its length with some parts that show a slightly larger contribution with more pinholes. Peters et al. reported also an almost evenly distribution of the leaks for Pd membranes [29]. Membrane 4b which was in the fluidized bed showed a higher total helium flow rate; however, no significantly higher contribution is obtained from the finger-like part, suggesting that the finger-like part did not suffer more than the other parts in the fluidized bed. For membrane 4b the helium flow rate along the membrane increased with the length of the membrane. It is suspected that this is related to interactions of the catalyst particles and the Pd film in the fluidized bed reactor. An inherent property of a fluidized bed is that bubbles of gas rise through the bed of solid particles, the size of the bubbles grow along the reactor. These bubbles carry particles in their wake inducing a solids circulation [30]. As bubbles rise in the bed, they grow and rise with higher velocity, thereby also increasing the particle velocity. The higher particle velocity results in an increased energy of impact of the collisions of the particles on the membrane. The results suggest that the increase in leakage rate is related to the increase in mechanical impact of the fluidized bed on the membranes. The temperature plays in this case a detrimental role in when the collisions of the particles become destructive to the membrane.

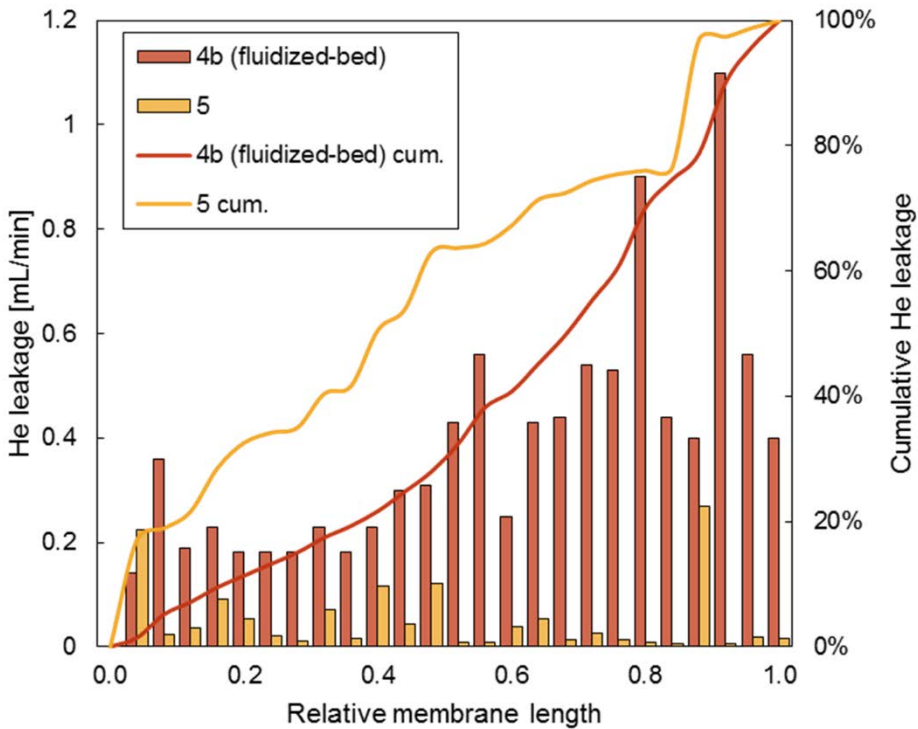


Figure 2.13. Helium flow rate distribution along the membrane 4b and 5.

2.3.6. Post mortem characterization

XRD

To verify whether there is chemical interaction and to investigate the alloying condition, XRD analysis has been used. Samples of the pre-tested membranes were compared with samples of the membranes after the tests. The results of the XRD analysis are presented in Figure 2.14. The only peaks that are distinguished correspond to either Pd, Ag or the alloy of Pd₇₅Ag₂₅. The pre-testing sample showed for membrane 1, 2 and 4 a split in the peak indicating that the alloy of Pd-Ag is not completely formed yet. This alloying can explain the increase in the hydrogen permeance during the first 200 hours of membranes 1 and 2 as opposed to membrane 3 in the long-term test [26]. The intensity of the used membrane 1, 2 and 3 are 2 to 3 times larger compared to the fresh membrane samples. The differences in the peak width and intensity indicate a change in morphology. According to the Scherrer equation 2.1, the crystal size is inversely proportional

to the peak width. In Table 2.4, the following crystal sizes were obtained for the tested membranes applying the Scherrer equation.

$$B = \frac{K\lambda}{L\cos(\theta)} \quad \text{Eq. 2.1}$$

Membrane 1, 2 and 3 show significant growth with increased time on stream and with temperature. The growth of crystals can be related to the growth in grain size. The growth of the grains can be used to explain the reduction in the hydrogen flux for membrane 1, 2 and 3. The diffusion of hydrogen along the grain boundary is ~100 times faster than the diffusion through the lattice [31]. The grain growth reduces the grain boundary density, hence the decrease in hydrogen flux [32]. SEM analysis was performed to confirm the grain growth and further investigate the structural changes.

Table 2.4. Crystal sizes calculated from XRD results.

	Membrane	Peak 111	Peak 200
		Crystal size (nm)	Crystal size (nm)
1	Pre testing	43.7	33.9
	used 2000 h	59.3	40.6
	used 2650 h	72.1	54.1
2	Pre testing	59.4	52.5
	used 2000 h	63.8	40.6
	used 2650 h	63.8	46.3
3	Pre testing	43.7	46.3
	used 2650 h	72.1	54.0
4	Pre testing	16.6	11.4
	after 715 h (600 °C)	63.8	50.6
	after FB 1150 h (500 °C)	63.8	47.7
5	Pre testing	61.4	46.3
	used 1150 h (500 °C)	59.2	47.7

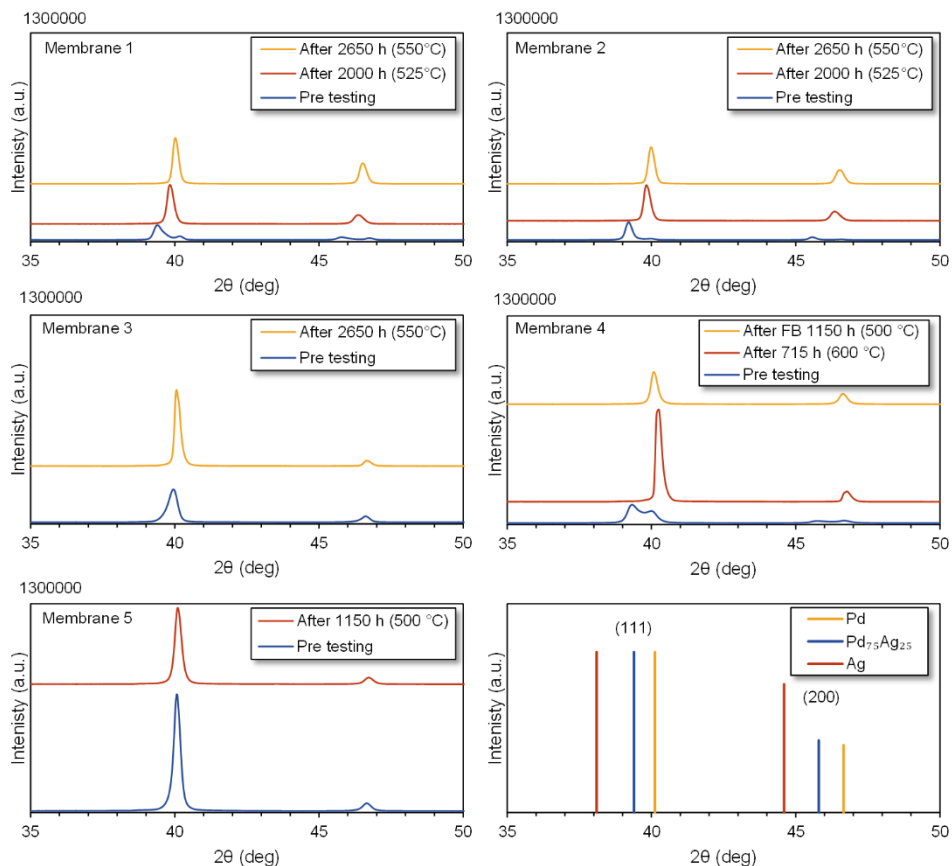


Figure 2.14. XRD profiles of the different membranes before and after testing.

SEM analysis

SEM analysis is used to further investigate the changes in the surface of the selective layers and to measure the thickness of the membranes, pre and post testing. Figure 2.15 shows the evolution of the surface of membrane 1 during the long-term test. Prior to the test, a smooth surface with a very small grain size can be observed. After 2000 hours of operation and a temperature up to 525 °C the grain size is increased, which even further increases after 2650 hours up to 550 °C. As can be seen, the grain boundary density is decreased and, as mentioned before, this can explain the observed decrease in the hydrogen flux. Besides the formation of larger grains, the membranes showed the formation of small pinholes. The formation of pinholes was relatively pronounced for membrane

3, where some of the black spots appear to be holes between the grain boundaries. The sizes of these defects, however, do not directly correspond to the size of the pinholes found by porometry. This would suggest that below the surface there is a narrower pitch between these defects which is measured by the porometry, while the growth and agglomeration of the grains results in the formation of these defects. Figure 2.17 shows the surface of membrane 4a, where the grains show a wide size distribution and seemed to have grown irregularly. Also from the porometry test it was concluded that the surface of membrane 4a contributes significantly to the nitrogen permeation. Moreover, membranes 1, 2, 3 and 4a showed an increase in crystal growth from the XRD results. Previous works indicated that microstructural changes of the surface result in the formation of void spaces [29,33–35]. It can therefore be suspected that the formation and connection of these defects resulted in the formation of pinholes, and at higher temperatures the more irregular surface deformation increases the number of defects formed and thereby the chance of the formation of pinholes. The thickness of the selective layer was also measured on a cross-section of the membranes. The thickness of the selective layer of membranes 1, 2, 3, 4a and membrane 5 before fluidization showed no changed compared to the fresh sample thickness of 4 to 5 microns.

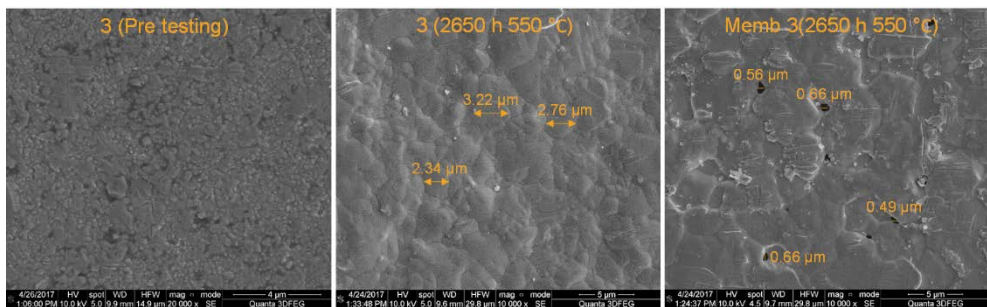


Figure 2.15. SEM pictures of the surface of membrane 1 pre-testing, after 2000 hours and after 2650 hours.

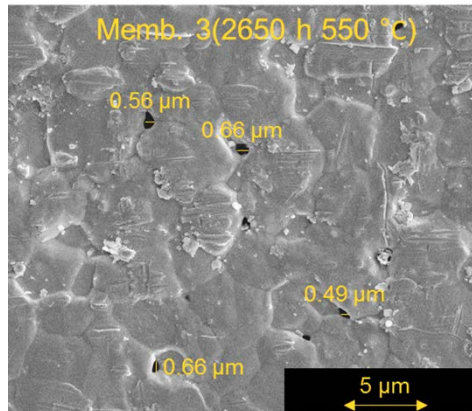


Figure 2.16. SEM picture of pinholes on the surface of membrane 3 after 2650 h and up to 550 °C.

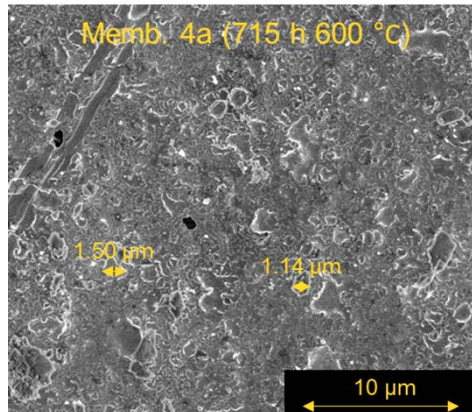


Figure 2.17. SEM picture of surface of membrane 4b after 715 h of operation up to 600 °C

Membrane 4b that was operated in the fluidized bed was divided into 3 sections to inspect the change of the surface along the membrane. In Figure 2.18 the surface of the membrane is shown for the three sections at two different magnifications, with the flow direction being from the bottom to the top of the images. A clear pattern is visible in the flow direction were towards the top the pattern becomes less spikey and more flat. The pattern looks like overlapping grains, like a fish scale. As mentioned in the discussion of the permeation results, the main increase in the nitrogen permeation was found to occur between 450 °C and 500 °C. Helmi et al. [36] showed that no significant surface effects were visible after fluidization at 400 °C. Therefore, it is expected that the main surface deformation took place between 450 °C and 500 °C. It is expected that a

combination of operation at the temperatures above 450 °C and the scouring action of the fluidized particles result in an increased surface energy. Since the palladium layer is ductile and the hardness of the palladium decreases with temperature, the increased surface energy could allow ductile deformation of the PdAg layer. EDS analyses revealed that the pattern formed on the surface is relatively homogeneous in composition indicating more mechanical interactions than chemical interactions with the catalyst. Beside the pattern, the surface itself also shows many small darker spots. From the EDS results in the dark spots a high presence of Al and O was found. Closer inspection showed that the dark spots were mainly holes. The high concentration of Al and O could be explained due to fines of the catalyst that are stuck in the holes of the surface. The thickness was measured with SEM on 4 different points along the membrane, using Figure 2.18 as a reference, at point A, between A and B, between B and C and at point C. The average thickness is shown to decrease from bottom to top with about 1 μm . This decrease in thickness seems to corroborate with the leak distribution results that showed a larger leakage contribution towards the top of the membrane as a result of the increased particle velocity. This shows that the configuration and design of a system can significantly affect the stability of the membranes, since the hydrodynamics play an important role in the particle velocities. Possible solutions to avoid the erosion effects observed in this work can be found in protecting the membranes with a porous ceramic layer, as presented in the recent work by Arratibel et al. [37].

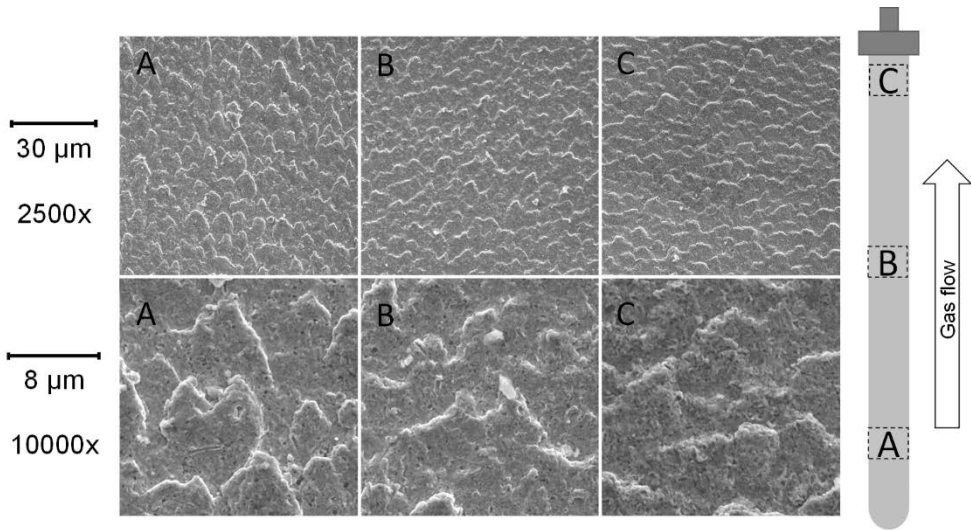


Figure 2.18. Surface effects on membrane 4b after 1150 hours and fluidization up to 500 °C.

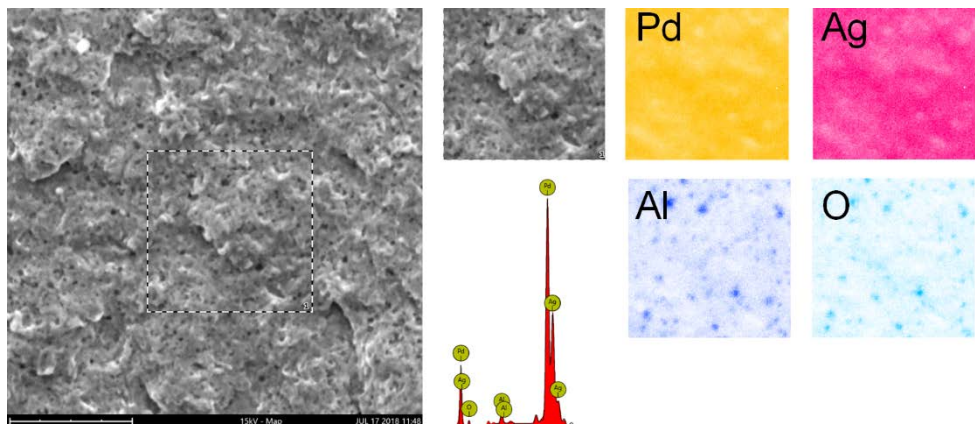


Figure 2.19. EDS on membrane 4b section B after 1150 hours and fluidization up to 500 °C.

2.4. Conclusions

In this chapter the long-term stability of thin-film PdAg membranes supported on Al₂O₃ porous supports was investigated. The performance of the membranes has been investigated over longer times on stream, assessing the relative contribution of the sealings and surface defects at different operating temperatures and with or without fluidized catalyst particles. The long-term stability experiments have shown an important contribution of leakages through the sealings, especially at lower operating conditions, where a reduction in the number of sealings resulted in a more stable operation. At temperatures above 500 °C the contribution of leakages coming from the surface become more pronounced and larger than the leakages through the sealings. The leak rates for the different membranes have been reported and can be used as a comparative basis. Post characterization showed that the main leakages originate from small pinholes < 55 nm in the surface of the membranes. Small surface defects are formed due to the agglomeration of Pd grains, while the increased grain size decreases the grain boundary density and thus also the hydrogen permeation rate over time. At temperatures above 550 °C a wide distribution of grain sizes on the surface is observed with a high contribution of surface defects. The results of these high-temperature experiments showed that when steam reforming is performed at temperatures above 500 °C a decrease in the perm-selectivity can be expected.

The integration of membranes in a fluidized bed up to 450 °C showed no significant impact on the stability of the palladium membranes. However, between 450 °C and 500 °C the membrane surface is significantly affected and the nitrogen permeance increases rapidly. Post characterization revealed that the bed hydrodynamics play a significant role on the extent of erosion of the membranes in the fluidized bed.

The observations described in this chapter from both the long-term tests and the tests in the fluidized bed will be used to select an operation regime and membrane handling during the reforming tests. Furthermore, it can be concluded that membrane reactors operated under reforming conditions for hydrogen production require improved membranes in terms of thermal stability. For the integration of the membranes in fluidized bed membrane reactors, the selective layer of Pd-Ag

needs to be protected or its mechanical stability needs to be further improved, while simultaneously the design of fluidized bed membrane reactors needs to be revisited to further improve the bed hydrodynamics and decrease the scouring action of the particles on the membranes.

References

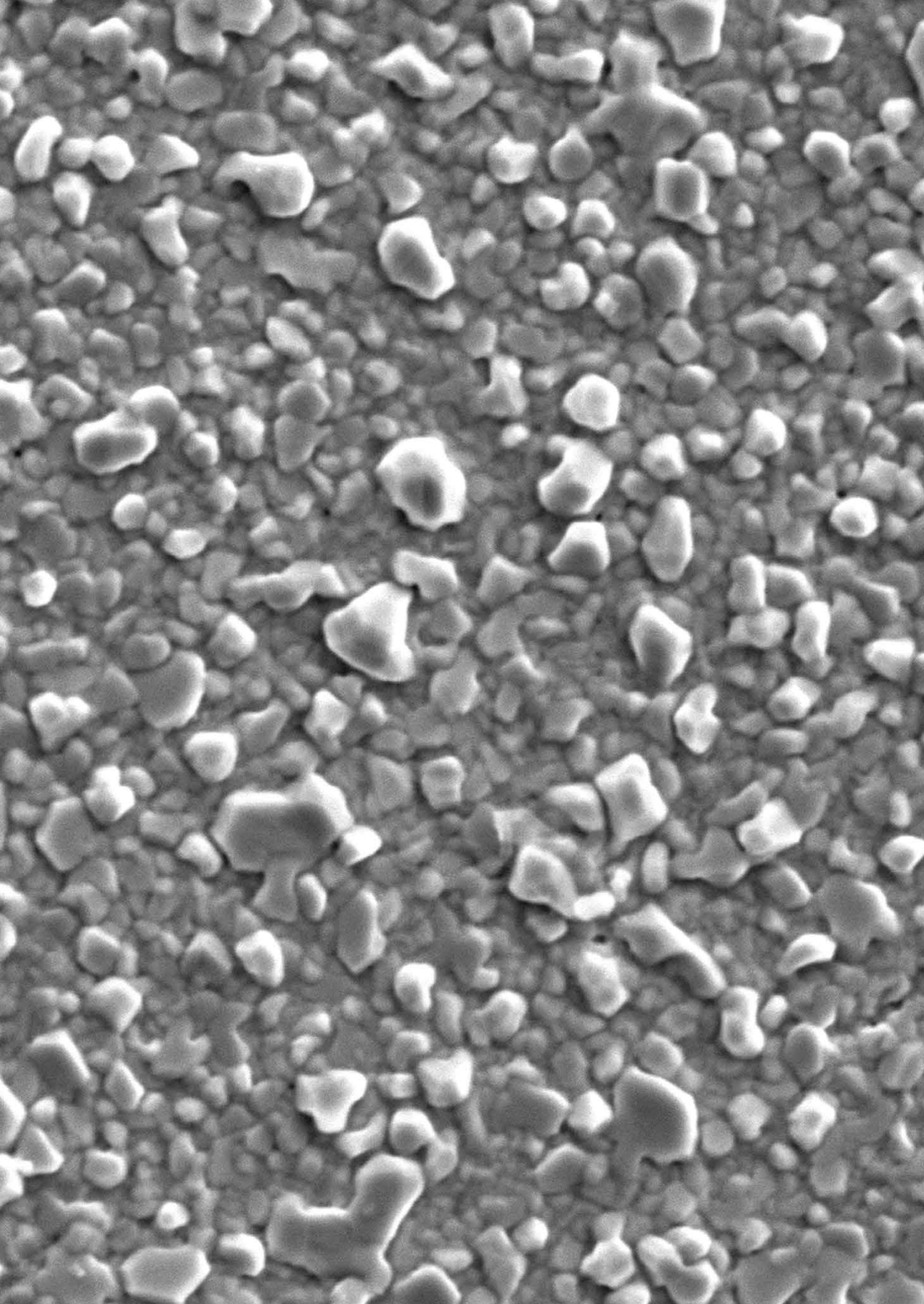
- [1] F. Gallucci, E. Fernandez, P. Corengia, M. van Sint Annaland, Recent advances on membranes and membrane reactors for hydrogen production, *Chem. Eng. Sci.* 92 (2013) 40–66. doi:10.1016/j.ces.2013.01.008.
- [2] A. Arratibel Plazaola, D.A. Pacheco Tanaka, M. Van Sint Annaland, F. Gallucci, Recent Advances in Pd-Based Membranes for Membrane Reactors, *Molecules*. 22 (2017) 1–53. doi:10.3390/molecules22010051.
- [3] S. Uemiya, N. Sato, H. Ando, T. Matsuda, E. Kikuchi, Steam reforming of methane in a hydrogen-permeable membrane reactor, *Appl. Catal.* 67 (1991) 223–230. doi:10.1016/S0166-9834(00)84445-0.
- [4] P.K. Seelam, S. Liguori, A. Iulianelli, P. Pinacci, V. Calabrò, M. Huuhtanen, et al., Hydrogen production from bio-ethanol steam reforming reaction in a Pd / PSS membrane reactor, *Catal. Today*. 193 (2012) 42–48. doi:10.1016/j.cattod.2012.01.008.
- [5] M.A. Islam, S. Ilias, Steam Reforming of Methanol in a Pd-Composite Membrane Reactor, *Sep. Sci. Technol.* 47 (2012) 2177–2185. doi:10.1080/01496395.2012.672357.
- [6] S. Yun, H. Lim, S. Ted Oyama, Experimental and kinetic studies of the ethanol steam reforming reaction equipped with ultrathin Pd and Pd-Cu membranes for improved conversion and hydrogen yield, *J. Memb. Sci.* (2012). doi:10.1016/j.memsci.2012.03.059.
- [7] J. Okazaki, T. Ikeda, D.A. Pacheco, K. Sato, T.M. Suzuki, F. Mizukami, et al., An investigation of thermal stability of thin palladium-silver alloy membranes for high temperature hydrogen separation, *J. Memb. Sci.* 366 (2011) 212–219. doi:10.1016/j.memsci.2010.10.011.
- [8] E. Fernandez, A. Helmi, K. Coenen, J. Melendez, J.L. Viviente, D.A. Pacheco Tanaka, et al., Development of thin Pd-Ag supported membranes for fluidized bed membrane reactors including WGS related gases, *Int. J. Hydrogen Energy*. 40 (2015) 3506–3519. doi:10.1016/j.ijhydene.2014.08.074.

- [9] A.L. Mejdell, M. Jøndahl, T.A. Peters, R. Bredesen, H.J. Venvik, Experimental investigation of a microchannel membrane configuration with a 1.4 μm Pd/Ag23 wt.% membrane-Effects of flow and pressure, *J. Memb. Sci.* 327 (2009) 6–10. doi:10.1016/j.memsci.2008.11.028.
- [10] S. Liguori, A. Iulianelli, F. Dalena, V. Piemonte, Y. Huang, A. Basile, Methanol steam reforming in an Al_2O_3 supported thin Pd-layer membrane reactor over Cu/ZnO/ Al_2O_3 catalyst, *Int. J. Hydrogen Energy.* 39 (2014) 18702–18710. doi:10.1016/j.ijhydene.2013.11.113.
- [11] H.W. Abu, E. Hawa, S.N. Paglieri, C.C. Morris, A. Harale, J.D. Way, Application of a Pd – Ru composite membrane to hydrogen production in a high temperature membrane reactor, *Sep. Purif. Technol.* 147 (2015) 388–397. doi:10.1016/j.seppur.2015.02.005.
- [12] A. Iulianelli, S. Liguori, Y. Huang, A. Basile, Model biogas steam reforming in a thin Pd-supported membrane reactor to generate clean hydrogen for fuel cells, *J. Power Sources.* 273 (2015) 25–32. doi:10.1016/j.jpowsour.2014.09.058.
- [13] Y.C. Van Delft, R. Sumbharaju, D.F. Meyer, A. De Groot, M. Sari, Steam reforming of methane in a bench-scale membrane reactor at realistic working conditions, 193 (2012) 74–80. doi:10.1016/j.cattod.2012.04.009.
- [14] Y. Shirasaki, T. Tsuneki, Y. Ota, I. Yasuda, S. Tachibana, H. Nakajima, et al., Development of membrane reformer system for highly efficient hydrogen production from natural gas, *Int. J. Hydrogen Energy.* 34 (2009) 4482–4487. doi:10.1016/j.ijhydene.2008.08.056.
- [15] L. Roses, F. Gallucci, G. Manzolini, M. van Sint Annaland, Experimental study of steam methane reforming in a Pd-based fluidized bed membrane reactor, *Chem. Eng. J.* 222 (2013) 307–320. doi:10.1016/j.cej.2013.02.069.
- [16] V. Spallina, G. Maturro, C. Ruocco, E. Meloni, V. Palma, E. Fernandez, et al., Direct route from ethanol to pure hydrogen through autothermal reforming in a membrane reactor: Experimental demonstration, reactor

- modelling and design, *Energy*. 143 (2018) 666–681. doi:10.1016/j.energy.2017.11.031.
- [17] D.A. Pacheco Tanaka, M.A. Llosa Tanco, S. Niwa, Y. Wakui, F. Mizukami, T. Namba, et al., Preparation of palladium and silver alloy membrane on a porous α -alumina tube via simultaneous electroless plating, *J. Memb. Sci.* 247 (2005) 21–27. doi:10.1016/j.memsci.2004.06.002.
- [18] N. de Nooijer, F. Gallucci, E. Pellizzari, J. Melendez, D.A. Pacheco Tanaka, G. Manzolini, et al., On concentration polarisation in a fluidized bed membrane reactor for biogas steam reforming: Modelling and experimental validation, *Chem. Eng. J.* 348 (2018). doi:10.1016/j.cej.2018.04.205.
- [19] ASTM International, ASTM F316-03 - Standard Test Methods for Pore Size Characteristics of Membrane Filters by Bubble Point and Mean Flow Pore Test, *Astm.* (2014). doi:10.1520/F0316-03R11.2.
- [20] C. Gunther, V. Prehn, T. Wölfel, New Membrane Applications in Liquid and Gas Separation, in: 15th Int. Conf. Inorg. Membr., 2018.
- [21] T.A. Peters, M. Stange, R. Bredesen, On the high pressure performance of thin supported Pd-23%Ag membranes-Evidence of ultrahigh hydrogen flux after air treatment, *J. Memb. Sci.* 378 (2011) 28–34. doi:10.1016/j.memsci.2010.11.022.
- [22] A.L. Mejdell, H. Klette, A. Ramachandran, A. Borg, R. Bredesen, Hydrogen permeation of thin, free-standing Pd/Ag23% membranes before and after heat treatment in air, *J. Memb. Sci.* 307 (2008) 96–104. doi:10.1016/j.memsci.2007.09.024.
- [23] L. Yang, Z. Zhang, X. Gao, Y. Guo, B. Wang, O. Sakai, et al., Changes in hydrogen permeability and surface state of Pd – Ag / ceramic composite membranes after thermal treatment, *J. Memb. Sci.* 252 (2005) 145–154. doi:10.1016/j.memsci.2004.12.006.
- [24] F. Roa, J.D. Way, The effect of air exposure on palladium-copper composite membranes, *Appl. Surf. Sci.* 240 (2005) 85–104. doi:10.1016/j.apsusc.2004.06.023.

- [25] D. Zemlyanov, B. Klötzer, H. Gabasch, A. Smeltz, F.H. Ribeiro, S. Zafeiratos, et al., Kinetics of Palladium Oxidation in the mbar Pressure Range: Ambient Pressure XPS Study, *Top. Catal.* 56 (2013) 885–895. doi:10.1007/s11244-013-0052-z.
- [26] A. Rollett, F. Humphreys, G.S. Rohrer, M. Hatherly, *Recrystallization and Related Annealing Phenomena: Second Edition*, 2004. doi:10.1016/B978-0-08-044164-1.X5000-2.
- [27] H.W. Abu, E. Hawa, S.N. Paglieri, C.C. Morris, A. Harale, J.D. Way, Identification of thermally stable Pd-alloy composite membranes for high temperature applications, *J. Memb. Sci.* 466 (2014) 151–160. doi:10.1016/j.memsci.2014.04.029.
- [28] J. Melendez, N. de Nooijer, K. Coenen, E. Fernandez, J.L.J.L. Viviente, M. van Sint Annaland, et al., Effect of Au addition on hydrogen permeation and the resistance to H₂S on Pd-Ag alloy membranes, *J. Memb. Sci.* 542 (2017) 329–341. doi:10.1016/j.memsci.2017.08.029.
- [29] T.A. Peters, P.A. Carvalho, J.F. Van Wees, J.P. Overbeek, E. Sagvolden, F.P.F. Van Berkel, et al., Leakage evolution and atomic-scale changes in Pd-based membranes induced by long-term hydrogen permeation, *J. Memb. Sci.* 563 (2018) 398–404. doi:10.1016/j.memsci.2018.06.008.
- [30] D. Kunii, O. Levenspiel, *Fluidization Engineering*, Elsevier, 1991. doi:10.1016/B978-0-08-050664-7.50012-3.
- [31] U. Stuhr, T. Striffler, H. Wipf, H. Natter, B. Wettmann, S. Janssen, et al., An investigation of hydrogen diffusion in nanocrystalline Pd by neutron spectroscopy, 254 (1997) 393–396.
- [32] K.J. Bryden, J.Y. Ying, Nanostructured palladium-iron membranes for hydrogen separation and membrane hydrogenation reactions, *J. Memb. Sci.* 203 (2002) 29–42. doi:10.1016/S0376-7388(01)00736-0.
- [33] F. Guazzone, Y.H. Ma, Leak Growth Mechanism in Composite Pd Membranes Prepared by the Electroless Deposition Method, 54 (2008). doi:10.1002/aic.

- [34] T.A. Peters, W.M. Tucho, A. Ramachandran, M. Stange, J.C. Walmsley, R. Holmestad, et al., Thin Pd-23%Ag/stainless steel composite membranes: Long-term stability, life-time estimation and post-process characterisation, *J. Memb. Sci.* 326 (2009) 572–581. doi:10.1016/j.memsci.2008.10.053.
- [35] A.J. Haslam, S.R. Phillpot, D. Wolf, D. Moldovan, H. Gleiter, Mechanisms of grain growth in nanocrystalline fcc metals by molecular-dynamics simulation, *J. Memb. Sci.* 318 (2001) 293–312.
- [36] A. Helmi, E. Fernandez, J. Melendez, D. Alfredo, P. Tanaka, F. Gallucci, et al., Fluidized bed membrane reactors for ultra pure H₂ production - A step forward towards commercialization, *Molecules*. 21 (2016). doi:10.3390/molecules21030376.
- [37] A. Arratibel, A. Pacheco Tanaka, I. Laso, M. van Sint Annaland, F. Gallucci, A. Pacheco, et al., Development of Pd-based double-skinned membranes for hydrogen production in fluidized bed membrane reactors, *J. Memb. Sci.* 550 (2018) 536–544. doi:10.1016/j.memsci.2017.10.064.



Chapter

Three

Influence of H₂S on thin-film PdAgAu membranes

Pd-based membranes have the potential to be used for hydrogen purification and production in membrane reactors. However, the presence of impurities in the feedstock, such as H₂S can poison the membrane, thus decreasing the hydrogen permeation by blocking and deactivating active sites of the Pd-alloy on the membrane surface. H₂S at high concentrations can even destroy the membrane by the formation of Pd₄S. It is known that alloying of Pd with Au enhances the membrane resistance to H₂S. This work reports the performance of six PdAg(Au)/Al₂O₃ supported membranes, prepared by electroless plating combined with PVD under exposure to trace amounts (<2 ppm) of H₂S. It is shown that the Au content does not play a significant role on the flux inhibition at these low concentrations. Exposure results suggest a dual influence of physisorbed H₂S and chemisorbed S species. The observed Langmuir type dependency shows that the influence of the partial pressure of hydrogen is negligible on the flux inhibition at industrially relevant conditions. In the post characterization the absence of Pd₄S was shown, however the surface was still affected by the exposure to H₂S.

This chapter is based on the following paper:

N.C.A. de Nooijer, J.Davalos Sanchez, J. Melendez Rey, E Fernandez, D.A. Pacheco Tanaka, M. van Sint Annaland, F. Gallucci. "Influence of H₂S on the hydrogen flux of thin-film PdAgAu membranes" International Journal of Hydrogen Energy. In Press, Corrected Proof (2019)

3.1. Introduction

Palladium-based membrane technology has gained significant attention because of the high flux and theoretically infinite perm-selectivity towards hydrogen [1]. One of the processes that has the potential to become a viable technology utilizing Pd-based membranes, is the production of hydrogen from biogas [2]. Biogas mainly consists of CH_4 and CO_2 , but also contains some trace components such as hydrogen sulphide (H_2S) (from 200 to 2000 ppm). The presence of the H_2S can damage equipment, catalyst and the Pd-based membranes. The hydrogen permeation can be decreased by the presence of low concentrations (< 2 ppm) of H_2S [3]. At higher concentrations of H_2S , the formation of Pd_4S further decreases the flux and can result in the deformation of the palladium lattice, which can create pinholes deteriorating the membrane performance [4,5]. Significant efforts have been devoted to the understanding of the effects of H_2S on the membrane properties and in finding a way to increase the H_2S resistance of the Pd-based membranes. However, with the current status the H_2S in biogas, and also natural gas or syngas from coal gasification, must be removed before being processed via Pd-based membranes. Moreover, the presence of other trace components such as siloxanes and NH_3 in biogas could affect the equipment in the system such as valves, compressors and the catalyst. Therefore, cleaning of the raw biogas remains imperative [6]. Technologies such as adsorption, absorption, membrane filtration and novel biological desulfurization processes can reduce H_2S levels. However, these processes may not always reach 100% H_2S removal efficiencies [7,5], also in view of economic constraints. It is therefore of importance to assess the resistance and understand the performance of Pd-based membranes under trace concentrations of H_2S .

Increasing the resistance of Pd-based membranes towards H_2S inhibition has been studied for many years. McKinley identified already in 1967 that gold (Au) or copper (Cu) alloyed with the Pd membrane can increase the resistance of the membranes by increasing the barrier for the irreversible formation of Pd_4S [4,8,9]. Several groups have studied the use of ternary membranes, such as PdAuCu and PdAgAu [10,11]. Peters et al. identified PdAgAu as an alloy with good properties to reduce H_2S poisoning [12], influencing the dissociation of H_2S by modification

of the potential energy surface [13]. However, a very different performance have been reported under exposure of H₂S [14], which could be related to differences in compositions and operating conditions, incomplete alloying, and differences in membrane thickness and surfaces of the membranes [15].

In this chapter, a set of PdAgAu membranes, with different concentrations of Au, have been investigated. The membranes were prepared by a sequential method, where first a layer of PdAg was deposited on a porous support by electroless plating, followed by PVD deposition of a layer of Au, and after alloying the membranes were exposed to hydrogen containing between 0.25 and 2 ppm of H₂S at 400, 450 and 500 °C. Under these conditions, the H₂S is known to inhibit the H₂ flux mainly by reversible adsorption [3,16]. A Langmuir adsorption isotherm is used to describe the inhibiting effects of trace amounts of H₂S on the hydrogen permeation rate.

3.2. Materials and methods

3.2.1. Membrane preparation

The membranes used in this chapter were prepared by ELP combined with PVD magnetron sputtering, as reported in previous papers [17,18]. Alumina tubes (10/7 mm o.d/i.d., 70-80 mm long) with an outer Al₂O₃ top layer (100 nm mean pore size) were used as membrane supports (provided by Rauschert Kloster Veilsdorf). First, a thin Pd-Ag layer (~4 μm thick) was deposited onto a ceramic support as reported in chapter 2. The Ag content determined by inductively coupled plasma optical emission spectrometer (ICP-OES) for these membranes was 5 wt%. The Pd and Ag deposited on the membrane was calculated from the initial and final concentrations of the metals in the plating solution. This characterization was carried out for a membrane used as a reference and prepared at the same conditions. Then, a thin Au layer was deposited onto the ELP layer by DC-Magnetron Sputtering technique using a "Cemecon CC800/8" apparatus. High purity (99.99%) Au rectangular plates (200 mm height – 88 mm width – 1.5 mm depth) were used as target materials and high purity Ar ionized gas was fed. The operating conditions used for the deposition were similar to the ones reported elsewhere [17], and the Au content on the final membranes was controlled by

adjusting the sputtering time. After the Au deposition by Magnetron Sputtering, an annealing treatment was carried out at 550 °C for 24 hours to homogenise the selective layer at the same conditions as reported in [11]. After the preparation, the membranes were sealed with Swagelok fittings according to the method presented by Fernandez et al. [19]. The layer thickness used was estimated from the preparation time. In Table 3.1, The Pd and Ag content obtained from the plating solution, the estimated Au content, membrane length and the membrane thickness of the samples are given in Table 3.1.

Table 3.1. Pd-Ag-Au membranes used in this study.

Membranes	Pd		Ag		Au		Length [mm]	~Layer Thickness (μm)
	estimated		estimated		estimated			
	wt%	at%	wt%	at%	wt%	at%		
M1	92.6	93.8	4.9	4.9	2.5	1.4	34.8	4
M2	90.3	92.4	4.8	4.8	5.0	2.8	9.8	4
M3	90.3	92.4	4.8	4.8	5.0	2.8	39.4	4
M4	90.3	92.4	4.8	4.8	5.0	2.8	28.4	4
M5	87.9	91.1	4.6	4.7	7.5	4.2	38.4	4
M6	87.9	91.1	4.6	4.7	7.5	4.2	34.9	4
M7	95.0	95.1	5.0	4.9	0	0	36.0	5

3.2.2. Permeation setup

Hydrogen permeation experiments were performed in a tube-in-shell configuration. The setup is suited to perform permeation experiments under the exposure of H_2S , a schematic representation of the setup is shown in Figure 3.1. A three zone oven was used to heat the reactor, where the temperature was controlled by three independent thermocouples, and an additional thermocouple was placed inside the membrane tube. The pressure was controlled by a Bronkhorst back pressure regulator and monitored both at the retentate and permeate side of the membrane. Bronkhorst mass flow controllers were used to feed the desired gases (H_2 , N_2 , $\text{H}_2/\text{H}_2\text{S}$ and O_2). The H_2S was added to the system from a bottle containing 10 ppm of H_2S in H_2 supplied by Linde. The H_2 permeance was continuously measured using a Bronkhorst mini Cori flow meter. The system

was fully automated and controlled by a computer. The N₂ permeance was manually measured with a Horibastec liquid film flow meter.

Prior to H₂S exposure, the membranes were stabilized at 500 °C in pure H₂ in order to start the experiments with a stable hydrogen flux. Then, the hydrogen permeation at several temperatures in the presence of H₂S were measured. Subsequently, the H₂S adsorbed on the membranes were removed by feeding pure hydrogen at 500 °C, and M1, M4, M5 and M7 membranes were step wise exposed to different amounts of H₂S during one single exposure. All exposures were performed at a total pressure of 2 bar(a).

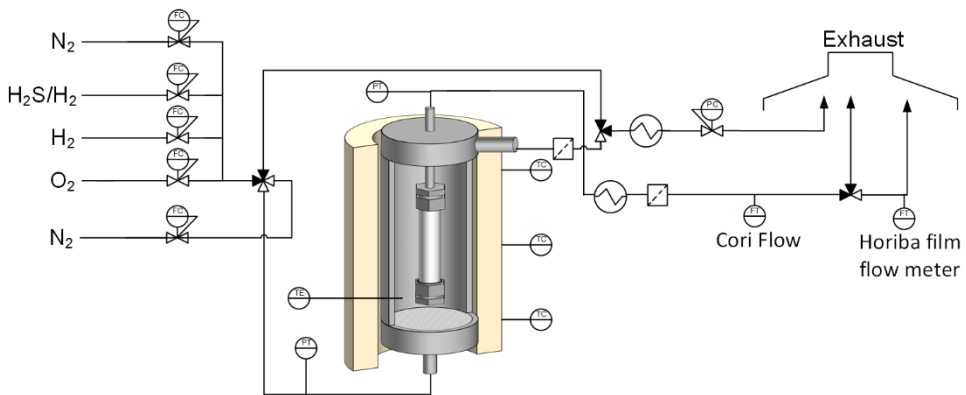


Figure 3.1. Schematic description of the experimental setup used in this work.

3.2.3. Post characterization

After the exposure experiments, a leak test was performed on the membranes, by pressurising the permeate side with He. To evaluate the leakage contribution the He pressurised membrane was slowly immersed in ethanol. Ethanol blocks the small pores and allows identifying in which position of the membranes the leaks are concentrated. X-ray photoelectron spectroscopy (XPS) was used to obtain surface details. The XPS characterization was performed with a monochromatic Thermo Scientific K-Alpha. Spectra were obtained using an aluminium anode (Al K α = 1486.6 eV) operating at 72 W and a spot size of 400 μ m and sputtering was done with a beam energy of 1000 eV at low current. Etching rate of Ta₂O₅ (reference sample) was 0.25 nm s⁻¹, performed with argon sputtering of 3·10⁻⁷ mbar, 3000 eV and low current. Samples before and after H₂S exposure were

analysed. The morphology of the samples after the experiments were analysed using a Phenom ProX Scanning Electron Microscope (SEM).

3.3. Results

3.3.1. Flux stabilization

To allow for a stable H₂ flux, during the H₂S exposure tests, the membranes were first activated (removal of burnable contaminants from the surface) by treatment for 2 min with a 50:50 mixture of nitrogen and air at 400 °C. The ideal H₂/N₂ perm selectivity was calculated from pure N₂ and H₂ permeances; the ideal perm selectivity of the membranes ranged from 1000 to 5000. The membranes were thereafter left in pure H₂ at 500 °C and a pressure difference of 1 bar for 72 h. From Figure 3.2 it is observed that first the hydrogen permeance was increased in time until stable permeation was obtained; membrane 1, having the lowest Au content, is the first to reach stable conditions. The increase in the permeance is attributed to uncomplete alloying of the membranes, concluding that after 72 hours all the membranes are completely alloyed. Membrane 7 shows that without Au the membrane is found to be stable within 20 hours. Melendez et al. reported a stabilization period of 24 hours at 400 °C in pure H₂ for a membrane containing 3.5% Au prepared by sequential ELP method [11]. The authors suggested that the Au content can increase the permeation by influencing the adsorption and dissociation steps. However, in this work no strong correlation is found between the permeance and the Au content. This could be related to slight differences in thickness of the selective layer, since from the ELP technique a homogeneous thickness cannot be guaranteed. After the hydrogen flux was stable the temperature was gradually decreased from 500 °C by 25 °C where a permeance test was carried out for each temperature until 400 °C. From these results the activation energy and pre-exponential factor were obtained, which are reported in Table 3.2 together with the permeability. The measured permeability at 500 °C correlates well to what was found by Melendez et al. and Peters et al. for PdAgAu membranes, $1.0 \cdot 10^{-8} \text{ mol m}^{-1} \text{ s}^{-1} \text{ Pa}^{-0.5}$ at 500 °C and $0.93 \cdot 10^{-8} \text{ mol m}^{-1} \text{ s}^{-1} \text{ Pa}^{-0.5}$ at 450 °C, respectively [12]. The activation energy however, was found to be significantly lower than the 16 kJ/mol reported by Melendez et al. and Braun et al. [11,20]. The obtained activation energies in this work were closer to the

activation energy of 11.3 kJ/mol obtained by Okazaki et al. for a Pd₉₀Au₁₀ membrane [21]. Au is known to affect the H₂ adsorption and dissociation, the difference in activation energy might therefore be related to differences in the surface concentration of Au. Membrane 7 showed a much lower permeability than expected for a PdAg membrane prepared by ELP, which is around $1.5 \cdot 10^{-8}$ mol m⁻¹s⁻¹Pa^{-0.5} at 400 °C [17].

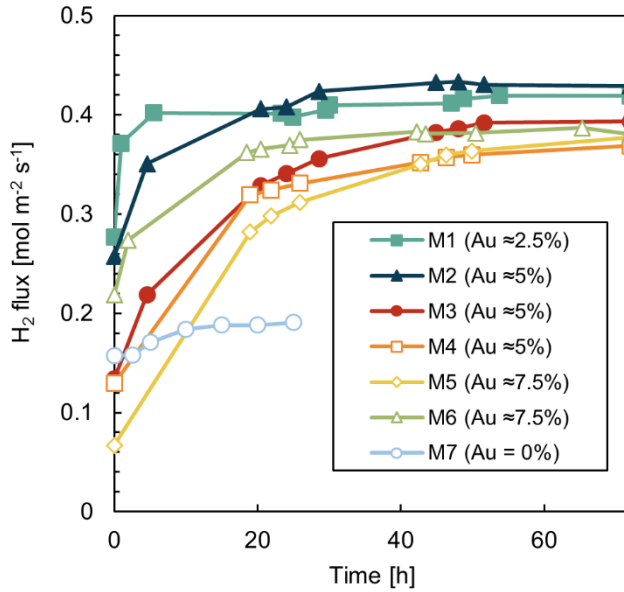


Figure 3.2. Stabilization of the PdAgAu membrane flux at 500 °C and 1 bar ΔP .

Table 3.2. Results from activation energy and pre-exponential factor fitting.

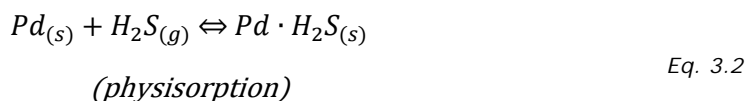
Membrane	M1	M2	M3	M4	M5	M6	M7
Ea (Activation energy) [kJ/mol]	9.7	14.1	9.5	11.3	9.6	11.0	13.2
P ⁰ (Pre-exponential factor) x10 ⁻² [mol m ⁻² s ⁻¹ Pa ^{0.5}]	1.30	3.37	1.29	1.54	1.19	1.40	1.42
Permeability at 500 °C x10 ⁻⁸ [mol m ⁻¹ s ⁻¹ Pa ^{-0.5}]	1.30	1.33	1.22	1.14	1.17	1.18	0.75

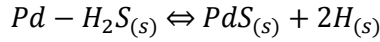
3.3.2. H₂S exposure

For the first exposures all membranes were exposed to H₂ containing H₂S at 1 bar pressure difference for 5 hours. After that the feed was switched to pure hydrogen and the permeation was monitored for an additional 8 hours. Figure 3.3, Figure 3.4 and Figure 3.5 show the results changing the Au content, temperature and H₂S concentration. The results are expressed in terms of the relative H₂ flux which was obtained by dividing the measured flux by the initial flux in pure hydrogen, as shown in Eq. 3.1.

$$\text{Relative } H_2 \text{ flux} = \frac{J_{H_2}^t}{J_{H_2(\text{pure } H_2)}^0} \quad \text{Eq. 3.1}$$

The loss of hydrogen permeance is the result of the adsorption of H₂S on the Pd surface, decreasing the number of active sites available for the adsorption of hydrogen (Eq. 3.2); each adsorbed sulphur atom can block 4-13 sites for H₂ adsorption [22,23]. The adsorbed H₂S on Pd is unstable and is catalytically decomposed into H₂ and S (Eq. 3.3) [24]; the strong repulsive interactions of H-S and S can result in further blocking of H₂ dissociation sites [24,25].





(chemisorption)

Eq. 3.3

After the incorporation of S into the membrane, sulphides such as PdS, Pd₁₆S₇, Ag₅Pd₁₀S₅ and Pd₄S can be formed, which depends on the concentration of H₂S and the temperature [26,27]. The formation of Pd₄S is the most probable, as it has the lowest free energy of formation [28]. The H₂ permeability of Pd₄S is approximately 20 times less than pure palladium [29]. The formation of Pd₄S causes an irreversible reduction of the permeance and a failure in the membrane due to the formation of defects. The conditions applied in this work were below the thermodynamic limit for sulphide formation of pure Pd at 450 °C of 5.67 ppm H₂S [5].

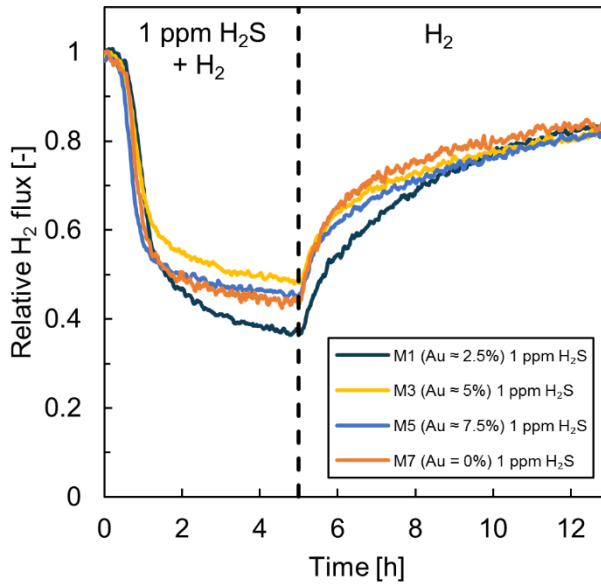


Figure 3.3. Relative flux during H₂S exposure and recovery of M1, M3, M5 and M7 at 450 °C.

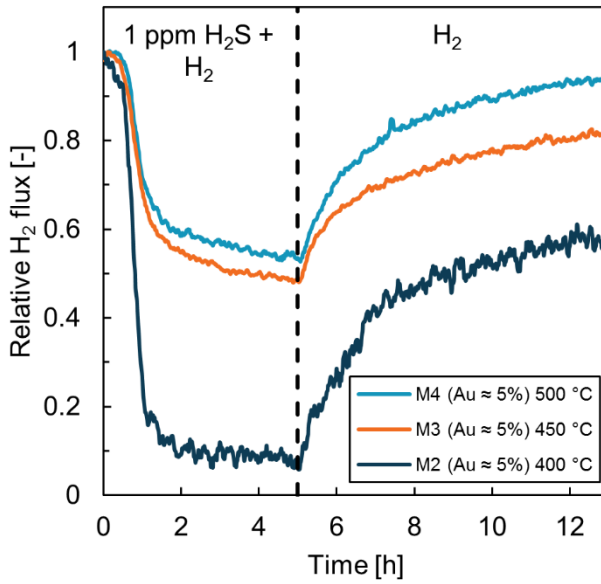


Figure 3.4. Relative H₂ permeance for membrane M2, M3 and M4 respectively at 400, 450 and 500 °C.

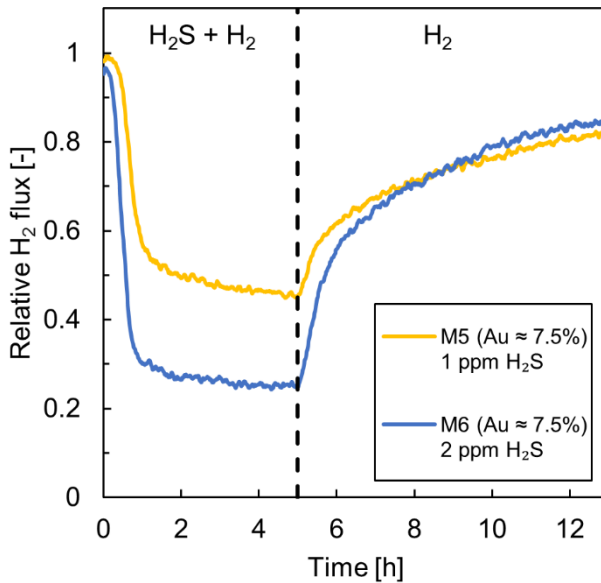


Figure 3.5. Relative H₂ permeance of M5 and M6, respectively exposed to 1 and 2 ppm of H₂S at 450 °C.

From the exposure graphs the decrease was found not to be instantaneous as often described in literature [9,30]. Chen et al. and Peters et al. also reported a gradual permeation decrease during exposure [3,16]. The retentate concentration was monitored and it was found that the decrease during exposure was related to the adsorption of H₂S on the permeation system, which took some time to equilibrate until a constant exposure concentration was obtained, at higher H₂S concentrations this equilibrium was obtained faster [16]. It was assumed that the delay obtained here was also related to the H₂S adsorption on the system and the relative large size of the reactor compared to the membrane surface in combination with the low concentration of H₂S resulted in the delay. After 30 minutes, a sharp decrease followed by a slower decrease in the H₂ permeation was observed.

To see the influence of Au content on the H₂ flux, the exposure of M1, M3, M5 and M7 to 1 ppm of H₂S at 450 °C is compared in Figure 3.3. The permeance decrease observed for M1 was from $2.67 \cdot 10^{-3}$ to $1.00 \cdot 10^{-3}$ mol m⁻²s⁻¹Pa^{-0.5} and for M7 from $1.5 \cdot 10^{-3}$ to $6.60 \cdot 10^{-4}$ mol m⁻²s⁻¹Pa^{-0.5} corresponding to a relative H₂ permeance decrease of 0.37 and 0.44 for M1 (0% Au) and M7 (Au 2.5%), respectively. M3 and M5 decreased to 0.48 and 0.45, respectively. The results of M3 and M5 are also shown in Figure 3.4 and Figure 3.5. From these results no clear correlation between the permeance decrease and Au content could be observed. The larger decrease of M7 could be explained by the low permeability. After H₂S exposure, pure H₂ was introduced into the system producing a slow recovery of the H₂ flux. After 8 hours of exposure all 4 membranes recovered up to ~0.85 of the value before exposure. The physically adsorbed H₂S can be relatively easily replaced by H₂ (Eq. 1), however the chemisorbed sulphur (Eq. 2) is more difficult to be removed. The addition of Au has shown to decrease the formation of sulphides and to have a higher resistance towards the formation of bulk sulphides [12]. However, from Figure 3.4 it can be seen that the extent of the permeance decrease or recovery is not much influenced by the Au content. This suggests that at these H₂S concentrations the main influence on the permeance decrease is the adsorbed H₂S and not so much the S, S-H and sulphide species therefore the influence of Au is not noticeable. Full recovery was achieved for the membranes at 500 °C in an additional 12 hours (not shown in this figure).

Relative decreases in flux of 0.15 to 0.47 have been reported in literature for PdAgAu membranes [22,31,32], however, for H₂S exposure concentrations that were significantly higher (> 20 ppm of H₂S) than applied in this work. In the work by Peters et al. [3], a PdAg film was exposed to a trace amount of 2 ppm for a period of 1 hour and a period of 10 min resulting in a recovery time of respectively 2 hours and <1 hour. The recovery time was much longer when exposed to 20 ppm and 100 ppm of H₂S [3]. In the work of Chen et al., an increased duration of the exposure resulted in longer recovery times [22].

To investigate the influence of the H₂S exposure temperature, membranes M2, M3 and M4 with the same estimated composition (Au 5%) were exposed to 1 ppm of H₂S for 5 hours at different temperatures (Figure 3.4). The decrease pattern of the relative permeation is very similar to that shown in Figure 3.3. However, the effect of the inhibition decreases as the temperature increases, as expected since the adsorption and possible dissociation of the H₂S onto the palladium surface is exothermic. The initial permeance for membrane M2, M3 and M4 were $2.53 \cdot 10^{-3}$, $2.82 \cdot 10^{-3}$ and $2.64 \cdot 10^{-3}$ mol m⁻²s⁻¹Pa^{-0.5}, respectively. The exposure to 1 ppm H₂S reduced the H₂ permeance to 0.07, 0.48 and 0.53 relative to the original flux for M2, M3 and M4, respectively. The highest recovery up to a relative flux of 0.96 was obtained with M4 at 500 °C, while for membrane M2 at 400 °C the recovery reached only 0.63, and full recovery was not possible in a practically achievable period at this temperature related to the formation of chemisorbed sulphur [33]. Only by going to higher temperatures this chemisorbed sulphur could be removed. Chen et al. also showed that, for a PdAu (8% Au) membrane exposed to 54.8 ppm of H₂S, lower permeance loss was obtained at higher temperatures and more permeance could be recovered.

The influence of the H₂S concentration on the H₂ permeation rate was investigated with membranes M5 and M6 (both with 7.5 % of Au) exposing them to 1 ppm and 2 ppm of H₂S respectively at 450 °C. The results are shown in Figure 3.5. The exposure to 2 ppm H₂S (M6) causes a faster initial drop in the permeance and a higher reduction in the H₂ permeation explained by the increased amount of H₂S adsorbed on the membrane surface. However, the permeation recovery after 8 hours is almost the same as for M5 (1 ppm H₂S), in the same time. The higher inhibition in this case did not result in a lower recovery as with M2 at lower

temperature. The regeneration and removal of chemisorbed S and S-H species seems to be a much slower process in comparison to the relatively fast desorption of the physisorbed H₂S. Only by increasing the temperature to 500 °C a fast and complete flux recovery can be achieved. These results agree with the two previously mentioned mechanisms responsible for the decrease in H₂ flux by H₂S. The first one is competitive adsorption between the H₂S and H₂ molecules for dissociation sites. The second is the energy barriers that are formed when the H₂S is dissociated into H₂ and S species. It is the removal of these species that require higher temperatures and an extended period of recovery. A third effect that could further decrease the flux and even result in failure of the membrane is the formation of Pd₄S, which in this work is avoided by keeping the conditions below the thermodynamic equilibrium for the formation of Pd₄S. The possible presence of Pd₄S was evaluated with post characterization, discussed later.

After the H₂S exposure experiments, the membranes M1, M4, M5 and M7 were regenerated for 12 hours at 500 °C with pure H₂ until they reached >90% of their initial permeance. These membranes were used in a sequential incremental exposure to five different concentrations of H₂S, (0.25, 0.5, 1, 1.5 and 2 ppm). Each membrane was exposed to each concentration for 5 hours; these results, together with the first results, are summarized in

Table 3.3. From this table it becomes apparent that after the recovery at 500 °C membranes M1, M4 and M8 are close to or even above 1, while membrane M5 only reached 0.91. These effects can be related to segregation or changes in the membrane topography due to the H₂S exposures and subsequent regeneration. The permeance decreases with increasing H₂S concentration as shown before in Figure 3.5. Comparing the exposures to 1 ppm H₂S from the sequential exposures with the first exposure, a slight difference can be observed probably due to small fluctuations in the H₂S concentration.

Table 3.3. Relative flux for each membrane for the first exposure and the second sequential exposure after exposure and recovery.

Membrane	Relative flux at 450 °C									
	First H ₂ S exposure			After 12h recovery at 500 °C	Sequential H ₂ S exposure					
	1 ppm	2 ppm	After 8 h recovery		0.25 ppm	0.5 ppm	1 ppm	1.5 ppm	2 ppm	After 8 h recovery
M1 (Au ≈ 2.5%)	0.37	-	0.85	1.00	0.77	0.64	0.43	0.30	0.27	0.91
M2 (Au ≈ 5%)	0.08*	-	0.61*	-	-	-	-	-	-	-
M3 (Au ≈ 5%)	0.48	-	0.80	-	-	-	-	-	-	-
M4 (Au ≈ 5%)	0.53**	-	0.95**	1.05	0.78	0.62	0.45	0.34	0.28	0.94
M5 (Au ≈ 7.5%)	0.45	-	0.82	0.91	0.64	0.52	0.40	0.30	0.24	0.79
M6 (Au ≈ 7.5%)	-	0.26	0.88	-	-	-	-	-	-	-
M7 (Au = 0%)	0.44	-	0.84	1.07	0.88	0.74	0.55	0.40	0.34	0.95

* Relative flux not at 450 °C but at 400 °C

** Relative flux not at 450 °C but at 500 °C

To investigate the influence of temperature on the decrease in H₂ permeance with increasing H₂S concentration, membrane M5 was regenerated again for 23 hours at 500 °C to reach a relative flux of 1, and then sequentially exposed from 0.25 to 2 ppm of H₂S at 400 °C, 450 °C and 500 °C. After the tests at each temperature the membrane was fully regenerated at 500 °C for 20 hours. The results are shown in Figure 3.6. The permeance decrease is higher at lower temperatures and seems to flatten at higher concentrations probably due to saturation of the active sites for adsorption. From the results in

Table 3.3 and Figure 3.6 the influence of the H₂S concentration on the inhibition becomes clear.

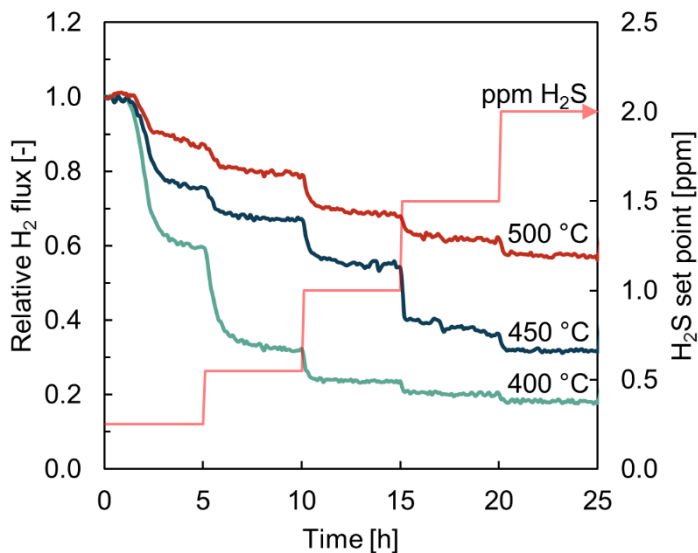


Figure 3.6. Relative H₂ permeance of M5 during sequential exposure of different H₂S concentrations at 400, 450 and 500 °C.

The Langmuir adsorption model has been used to describe the H₂S inhibition of Pd membranes [34,35]. In this work the inhibition model proposed by Peters et al. was used to evaluate the obtained experimental results [34]. The relative flux is compared to the inhibited surface coverage of hydrogen divided by the surface coverage of hydrogen for the clean membrane, this yields Eq. 3.4. In this equation

θ_{H_2S/H_2} and θ_{H_2} represent the surface coverage with H_2S and without respectively, P_{H_2} and P_{H_2S} are the partial pressures of H_2 and H_2S (in Pa). K_H and K_S are the adsorption coefficients of H_2 and S species (in Pa^{-1}).

$$Relative\ H_2\ flux = \frac{\theta_{H_2S/H_2}}{\theta_{H_2}} = \frac{1 + \sqrt{K_H P_{H_2}}}{1 + \sqrt{K_H P_{H_2}} + K_S P_{H_2S}} \quad Eq. 3.4$$

The adsorption equilibrium constant of hydrogen was estimated with the method presented by Israni et al., see Eq. 3.5 [36]. This -0.68 eV/molecule is in the range (-0.58 to -1.22 eV/molecule) for Pd and PdAg alloys values reported from DFT calculations in literature.

$$K_H = 6.17 \cdot 10^{-10} e^{\left(\frac{0.68 \left(\frac{eV}{molecule} \right)}{k_B T} \right)} \quad Eq. 3.5$$

K_H is then used in Eq. 3.4 to obtain K_S for the results shown in Figure 3.6, the fitting obtained is shown in Figure 3.7. The K_S obtained from the fitting was used to obtain the activation energy shown in Eq. 3.6. The activation energy of -1.12 eV/molecule, is close to the -1.20 eV for co-adsorption of S and H reported by Peters et al.

$$K_S = 1.78 \cdot 10^{-7} e^{\left(\frac{1.12 \left(\frac{eV}{molecule} \right)}{k_B T} \right)} \quad Eq. 3.6$$

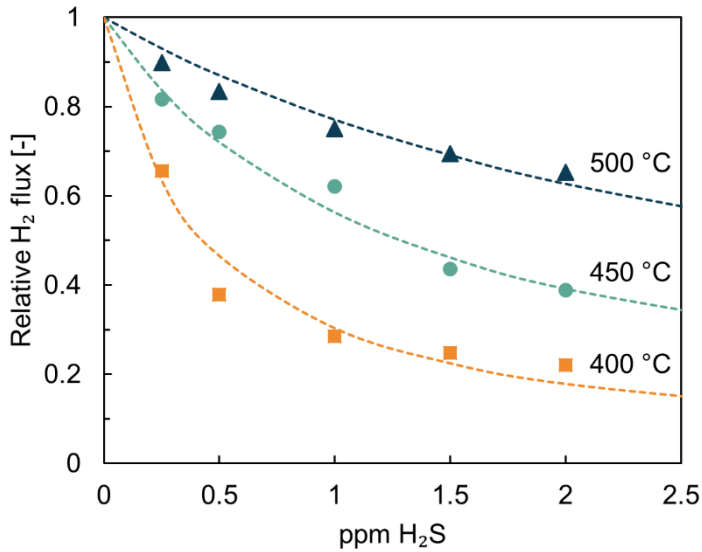


Figure 3.7. M5 Relative H₂ flux vs H₂S concentration, where the markers indicated the experimental points and dotted lines the relative flux description.

In practical applications the fraction of hydrogen with respect to the concentration of H₂S is however much lower than in most literature and these experiments. The implication of Eq. 3.4 and the fitted parameters of Eq. 3.5 and Eq. 3.6 is that the influence of the hydrogen fraction is negligible. This is also confirmed with the results of a similar permeation experiment on M5, however in this case performed with a 75% H₂ in N₂ mixture, at 450 °C. In Figure 3.8 this experiment shows a good agreement with the description relative flux description obtained from Eq. 3.4. It should however be considered that the thermodynamic limit for Pd₄S formation is lowered with a decrease in the partial pressure of hydrogen [5]. The negligible influence of the partial pressure of hydrogen implies that the influence of H₂S increases with the total pressure, as shown in Figure 3.9.

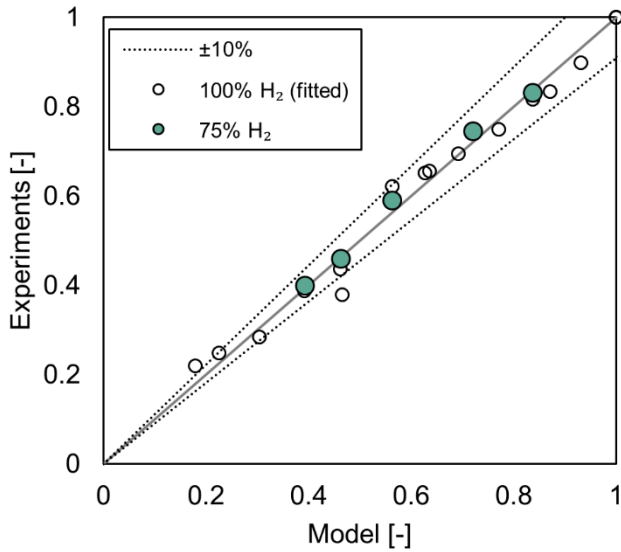


Figure 3.8. Parity plot for the experiments applied in the fitting (open dots) and experiments performed with a 75% H₂ in N₂ mixture in hydrogen.

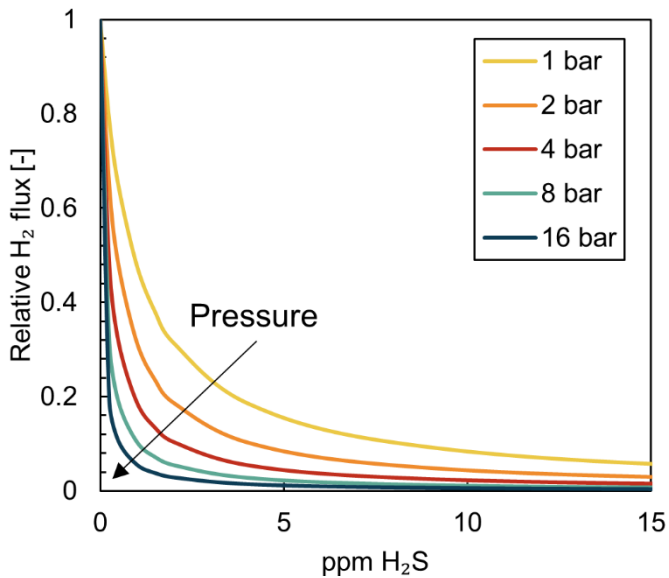


Figure 3.9. Model estimation of the influence of pressure on the H₂S flux inhibition at 450 °C.

3.3.3. Post characterization

It is often reported in the literature that the selectivity decreases when the Pd-based membranes are exposed to H₂S. This decrease is often related to the formation of Pd sulphides (mainly Pd₄S) that results in changes of the alloy lattice producing cracks in the membrane. The ideal perm-selectivity of the membranes investigated in this work ranged initially from 1000 to 5000 except for membrane M3 which was 297, which was mainly due to leakages from the sealing. The membranes showed, after testing, a leak increase of 30% on average, which could be related to leakages from the sealing, which was observed for some of the membranes when immersed in ethanol and pressurised on the permeate side with He.

XPS analyses were performed on the tested samples. The Pd_{3d}, Ag_{3d}, Au_{4f} and S_{2p} core level spectra of the surface of each membrane was evaluated. No clear peaks for S⁰ 2p_{1/2} or S⁰ 2p_{3/2} were observed in the S_{2p} spectra. This indicates that no Pd_xS was present in the samples. The depth profile of membrane M3 is shown in Figure 3.10 after preparation and after H₂S testing. The results for the other membranes were very comparable to the profile of M3. The average concentration on the surface obtained from the XPS analyses is shown in Table 3.4 together with the composition after 1000 s of sputtering. The 1000 s is estimated to correspond to around ~1% of the selective layer. On average over the first 100 s of sputtering the fraction of palladium on the surface is higher than towards the bulk of the layer, indicating a slight migration of Pd towards the surface.

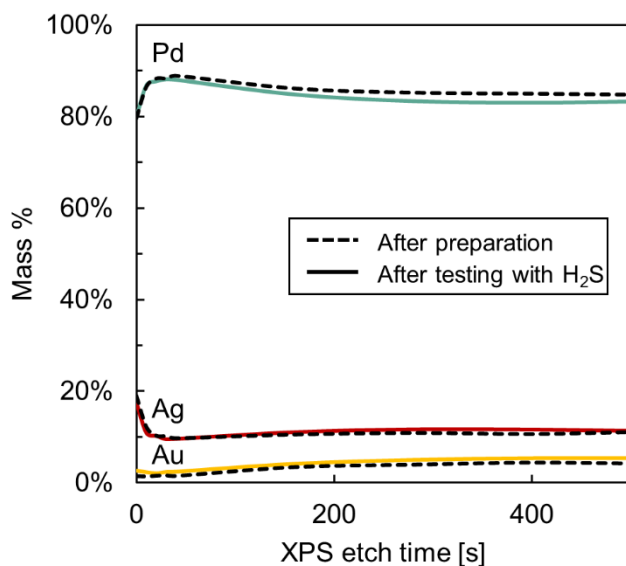


Figure 3.10. XPS depth profile of M3 after preparation and after testing.

Table 3.4. XPS measurement surface composition and composition after 1000 s sputtering of the membrane in mass %.

Membrane	Surface composition [mass%]			Composition after 1000 s [mass %]		
	Pd	Ag	Au	Pd	Ag	Au
M1 (Au \approx 2.5%)	87.7	11.5	0.8	85.1	12.4	2.6
M2 (Au \approx 5%)	80.8	17.0	2.2	81.9	13.1	5.0
M3 (Au \approx 5%)	80.0	17.4	2.6	84.2	11.2	4.7
M4 (Au \approx 5%)	81.4	16.8	1.8	81.3	14.1	4.6
M5 (Au \approx 7.5%)	83.5	14.1	2.4	87.7	7.8	4.6
M6 (Au \approx 7.5%)	79.6	15.6	4.8	82.1	10.1	7.8
M7 (Au = 0%)	88.2	11.8	-	93.4	6.6	-

The surface of the membranes was investigated by SEM after preparation and after the H₂S exposures. A clear difference could be observed between the

membranes that were only exposed to a single H₂S exposure of 5 hours (M2, M3 and M6). The membranes which were regenerated and used again showed a rougher topography with larger particle like grains. This could be best observed comparing M5 and M6 as shown in Figure 3.11A and Figure 3.11B. A grain formation similar to that observed for M5 has been reported by Melendez et al. and was related to the formation of Pd₄S [11]. In this work however, no indication of Pd₄S was observed from the XPS results, it is expected that the formation of these grains is a result of the migration of the palladium or the chemisorbed H₂S, which was completely removed during the regeneration, but may have resulted in the deformation of the membrane surface. The rate of these effects might be very slow, and due to the longer time of exposure of M5 more evident than for M6. Excessive transformation of the membrane surface could lead to the formation of pinholes, which could in the end significantly decrease the selectivity.

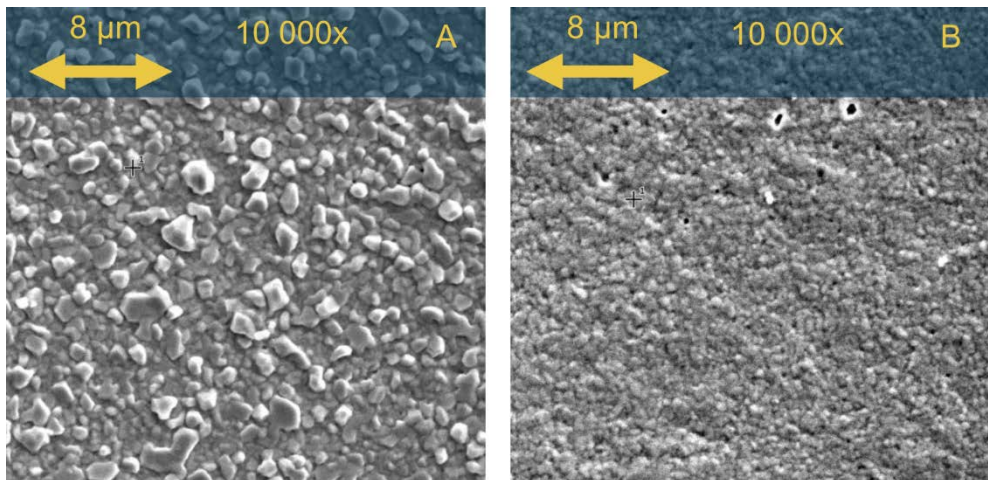


Figure 3.11. SEM picture of the surface of M5(A) after several H₂S exposure and M6(B) after a single H₂S exposure.

3.4. Conclusions

In this paper six PdAgAu membranes and PdAg membrane have been prepared and the effect of small amounts of H₂S (< 2 ppm) in the H₂ feed on the hydrogen permeation fluxes were studied. The PdAgAu membranes were prepared by sequential ELP and PVD deposition, and had an Au content ranging from 2.5% to 7.5%. The membranes were sealed and stabilized at 500 °C for 72 h in a hydrogen

environment during this period, stable hydrogen permeation was obtained suggesting that complete alloying was achieved. The membrane with the lower Au content reached stable conditions in the shortest amount of time. After the stabilization the membranes were exposed to up to 2 ppm of H₂S, which is below the thermodynamic limit for formation of palladium sulphides; therefore, the inhibition was reversible. The membranes showed a relative flux decrease of around 50%. The extent of this decrease in H₂S flux was shown to be influenced both by temperature, due to the exothermic nature of H₂S adsorption, and the H₂S concentration. Four of the membranes were selected and were fully recovered to the initial membrane flux and were subsequently exposed to sequentially increased H₂S concentrations. The decrease in flux of these membranes did not show a correlation with the Au content, in this work the increase of Au content did not show beneficial results with respect to H₂S exposure. It is suggested that at these low concentrations of H₂S, the physisorption of H₂S is dominating while at higher concentrations the effect Au addition could be beneficial since than the effects of S-H, S and sulphide species on the H₂ dissociation are more pronounced. With a Langmuir term the measured inhibition of H₂ permeation flux by H₂S could be well described. The influence of the partial pressure of hydrogen was found to be negligible on the inhibition at low pressures, while it was shown that the fitted inhibition parameters indicate that at higher operating pressures the total pressure has a very significant influence and this should be studied in more detail, since the desired operation regimes for industrial application of these membranes are at elevated pressures. The post characterization showed that no sulphide formation was present at these membranes after the tests, as expected, since the H₂S tests were carried out at conditions below the thermodynamic limit of Pd₄S formation. Studies over the past decades has shown that the resistance towards the Pd₄S formation can be improved by alloying with Au. However, the work in this chapter shows au addition is not sufficient to limit the effects of inhibition and structural changes of the membrane. Therefore, the approach of avoiding contact between the H₂S and the membrane should be considered, as this will both avoid deterioration of the membrane and inhibition of the membrane flux.

References

- [1] F. Gallucci, E. Fernandez, P. Corengia, M. van Sint Annaland, Recent advances on membranes and membrane reactors for hydrogen production, *Chem. Eng. Sci.* 92 (2013) 40–66. doi:10.1016/j.ces.2013.01.008.
- [2] N. de Nooijer, F. Gallucci, E. Pellizzari, J. Melendez, D.A. Pacheco Tanaka, G. Manzolini, et al., On concentration polarisation in a fluidized bed membrane reactor for biogas steam reforming: Modelling and experimental validation, *Chem. Eng. J.* 348 (2018) 232–243. doi:10.1016/j.cej.2018.04.205.
- [3] T.A. Peters, M. Stange, P. Veenstra, A. Nijmeijer, R. Bredesen, The performance of Pd-Ag alloy membrane films under exposure to trace amounts of H₂S, *J. Memb. Sci.* 499 (2016) 105–115. doi:10.1016/j.memsci.2015.10.031.
- [4] N. Pomerantz, Y.H. Ma, Effect of H₂S on the Performance and Long-Term Stability of Pd/Cu Membranes, *Ind. Eng. Chem. Res.* 48 (2009) 4030–4039.
- [5] M. V. Mundschau, X. Xie, C.R. Evenson IV, A.F. Sammells, Dense inorganic membranes for production of hydrogen from methane and coal with carbon dioxide sequestration, *Catal. Today.* 118 (2006) 12–23. doi:10.1016/j.cattod.2006.01.042.
- [6] O. Wesley, A. Yaqian, Z. Ange, N. Doan, P. Minh, A Review of Biogas Utilisation, Purification and Upgrading Technologies, *Waste and Biomass Valorization.* 8 (2017) 267–283. doi:10.1007/s12649-016-9826-4.
- [7] M. Israel, D. Jeison, R. Muñoz, L. Meier, I. Diaz, D. Jeison, A review on the state-of-the-art of physical / chemical and biological technologies for biogas upgrading, *Rev. Environ. Sci. Biotechnol.* 14 (2015) 727–759. doi:10.1007/s11157-015-9379-1.
- [8] S.K. Gade, S.J. Devoss, K.E. Coulter, S.N. Paglieri, G.O. Alptekin, J.D. Way, Palladium-gold membranes in mixed gas streams with hydrogen sulfide: Effect of alloy content and fabrication technique, *J. Memb. Sci.* 378 (2011)

- 35–41. doi:10.1016/j.memsci.2010.11.044.
- [9] C.P. O'Brien, B.H. Howard, J.B. Miller, B.D. Morreale, A.J. Gellman, Inhibition of hydrogen transport through Pd and Pd₄₇Cu₅₃ membranes by H₂S at 350 °C, *J. Memb. Sci.* 349 (2010) 380–384. doi:10.1016/j.memsci.2009.11.070.
- [10] T.A. Peters, T. Kaleta, M. Stange, R. Bredesen, Development of thin binary and ternary Pd-based alloy membranes for use in hydrogen production, *J. Memb. Sci.* 383 (2011) 124–134. doi:10.1016/j.memsci.2011.08.050.
- [11] J. Melendez, N. de Nooijer, K. Coenen, E. Fernandez, J.L. Viviente, M. van Sint Annaland, et al., Effect of Au addition on hydrogen permeation and the resistance to H₂S on Pd-Ag alloy membranes, *J. Memb. Sci.* 542 (2017). doi:10.1016/j.memsci.2017.08.029.
- [12] T.A. Peters, T. Kaleta, M. Stange, R. Bredesen, Development of ternary Pd-Ag-TM alloy membranes with improved sulphur tolerance, *J. Memb. Sci.* 429 (2013) 448–458. doi:10.1016/j.memsci.2012.11.062.
- [13] M.P. Hyman, B.T. Loveless, J.W. Medlin, A density functional theory study of H₂S decomposition on the (1 1 1) surfaces of model Pd-alloys, *601* (2007) 5382–5393. doi:10.1016/j.susc.2007.08.030.
- [14] A. Arratibel Plazaola, D.A. Pacheco Tanaka, M. Van Sint Annaland, F. Gallucci, Recent Advances in Pd-Based Membranes for Membrane Reactors, *Molecules.* 22 (2017) 1–53. doi:10.3390/molecules22010051.
- [15] E. Acha, Y.C. Van Delft, J.F. Cambra, P.L. Arias, Thin PdCu membrane for hydrogen purification from in-situ produced methane reforming complex mixtures containing H₂S, *Chem. Eng. Sci.* 176 (2018) 429–438. doi:10.1016/j.ces.2017.11.019.
- [16] C. Chen, Sulfur Tolerance of Pd/Au Alloy Membranes for Hydrogen Separation from Coal Gas, 2011.
- [17] E. Fernandez, J.A. Sanchez-Garcia, J. Melendez, V. Spallina, M. van Sint Annaland, F. Gallucci, et al., Development of highly permeable ultra-thin

- Pd-based supported membranes, *Chem. Eng. J.* 305 (2016) 149–155. doi:10.1016/j.cej.2015.11.060.
- [18] B. Dittmar, A. Behrens, N. Schödel, M. Rüttinger, T. Franco, G. Straczewski, et al., Methane steam reforming operation and thermal stability of new porous metal supported tubular palladium composite membranes, *Int. J. Hydrogen Energy.* (2013). doi:10.1016/j.ijhydene.2013.05.030.
- [19] E. Fernandez, K. Coenen, A. Helmi, J. Melendez, J. Zuñiga, D.A. Pacheco Tanaka, et al., Preparation and characterization of thin-film Pd-Ag supported membranes for high-temperature applications, *Int. J. Hydrogen Energy.* 40 (2015) 13463–13478. doi:10.1016/j.ijhydene.2015.08.050.
- [20] F. Braun, A.M. Tarditi, J.B. Miller, L.M. Cornaglia, Pd-based binary and ternary alloy membranes: Morphological and perm-selective characterization in the presence of H₂S, *J. Memb. Sci.* 450 (2014) 299–307. doi:10.1016/j.memsci.2013.09.026.
- [21] J. Okazaki, D.A.P. Tanaka, M.A.L. Tanco, Y. Wakui, T. Ikeda, F. Mizukami, et al., Preparation and Hydrogen Permeation Properties of Thin Pd-Au Alloy Membranes Supported on Porous α -Alumina Tube, *Mater. Trans.* 49 (2008) 449–452. doi:10.2320/matertrans.MBW200720.
- [22] C.H. Chen, Y.H. Ma, The effect of H₂S on the performance of Pd and Pd/Au composite membrane, *J. Memb. Sci.* 362 (2010) 535–544. doi:10.1016/j.memsci.2010.07.002.
- [23] M.L. Burke, R.J. Madix, Hydrogen on Pd(100)-S: the effect of sulfur on precursor mediated adsorption and desorption, *Surf. Sci.* 237 (1990) 1–19. doi:10.1016/0039-6028(90)90515-A.
- [24] S. Wilke, M. Scheffler, Poisoning of Pd (100) for the dissociation of H₂: a theoretical study of co-adsorption of hydrogen and sulphur, *Surf. Sci.* 329 (1995) L605--L610.
- [25] D.R. Alfonso, A. V. Cugini, D.C. Sorescu, Adsorption and decomposition of H₂S on Pd(1 1 1) surface: A first-principles study, *Catal. Today.* 99 (2005)

- 315–322. doi:10.1016/j.cattod.2004.10.006.
- [26] W. Feng, Q. Wang, X. Zhu, Q. Kong, J. Wu, P. Tu, Influence of Hydrogen Sulfide and Redox Reactions on the Surface Properties and Hydrogen Permeability of Pd Membranes, *Energies*. 11 (2018). doi:10.3390/en11051127.
- [27] L. Zhao, A. Goldbach, H. Xu, Tailoring palladium alloy membranes for hydrogen separation from sulfur contaminated gas streams, *J. Memb. Sci.* 507 (2016) 55–62. doi:10.1016/j.memsci.2016.01.055.
- [28] R. Bhatt, S. Bhattacharya, R. Basu, A. Singh, U. Deshpande, C. Surger, et al., Growth of Pd₄S, PdS and PdS₂ films by controlled sulfurization of sputtered Pd on native oxide of Si, 539 (2013) 41–46. doi:10.1016/j.tsf.2013.04.143.
- [29] B.D. Morreale, B.H. Howard, O. Iyoha, R.M. Enick, L. Chen, D.S. Sholl, Experimental and computational prediction of the hydrogen transport properties of Pd₄S, *Ind. Eng. Chem. Res.* 46 (2007) 6313–6319. doi:10.1021/ie070461u.
- [30] M. Kajiwara, S. Uemiya, T. Kojima, Stability and hydrogen permeation behavior of supported platinum membranes in presence of hydrogen sulfide, *Int. J. Hydrogen Energy*. 24 (1999) 839–844. doi:10.1016/S0360-3199(98)00156-6.
- [31] A.E. Lewis, H. Zhao, H. Syed, C.A. Wolden, J.D. Way, PdAu and PdAuAg composite membranes for hydrogen separation from synthetic water-gas shift streams containing hydrogen sulfide, *J. Memb. Sci.* 465 (2014) 167–176. doi:10.1016/j.memsci.2014.04.022.
- [32] F. Braun, J.B. Miller, A.J. Gellman, A.M. Tarditi, B. Fleutot, P. Kondratyuk, et al., PdAgAu alloy with high resistance to corrosion by H₂S, *Int. J. Hydrogen Energy*. 37 (2012) 1–9. doi:10.1016/j.ijhydene.2012.09.040.
- [33] D.R. Alfonso, First-principles study of sulfur overlayers on Pd(111) surface, *Surf. Sci.* 596 (2005) 229–241. doi:10.1016/j.susc.2005.09.021.

- [34] T.A. Peters, J.M. Polfus, F.P.F. van Berkel, R. Bredesen, Interplay between propylene and H₂S co-adsorption on the H₂ flux characteristics of Pd-alloy membranes employed in propane dehydrogenation (PDH) processes, *Chem. Eng. J.* 304 (2016) 134–140. doi:10.1016/j.cej.2016.06.065.
- [35] M.A. Murmura, M. Sheintuch, Permeance inhibition of Pd-based membranes by competitive adsorption of CO: Membrane size effects and first principles predictions, *Chem. Eng. J.* 347 (2018) 301–312. doi:10.1016/j.cej.2018.04.072.
- [36] S.H. Israni, M.P. Harold, Methanol steam reforming in Pd-Ag membrane reactors: Effects of reaction system species on transmembrane hydrogen flux, *Ind. Eng. Chem. Res.* 49 (2010) 10242–10250. doi:10.1021/ie1005178.



Chapter

Four

Biogas steam reforming: modelling and experimental validation

Biogas as feedstock for the production of hydrogen imposes challenges for the reforming process. In this chapter the integration of catalyst and membranes under biogas reforming is studied. A phenomenological one-dimensional two-phase fluidized bed reactor model accounting for mass transport towards the membranes with a stagnant film model has been developed and used to investigate the system performance. The validation of the model was performed with steam reforming experiments. The model results were in good agreement with the experimental results, when assuming a thickness of the stagnant mass transfer boundary layer around the membrane equal to 0.54 cm. It is shown the effects of concentration polarisation in a fluidized bed membrane reactor can be well described with the implementation of a film layer description in the two-phase model.

This chapter is based on the following paper:

N.C.A. de Nooijer, F. Gallucci, E. Pellizzari, J. Melendez, D.A. Pacheco Tanaka, G. Manzolini, M. van Sint Annaland. "On concentration polarisation in a fluidized bed membrane reactor for biogas steam reforming: modelling and experimental validation", *Chemical Engineering Journal*. 348 (2018), 232-243.

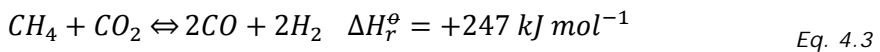
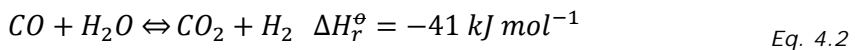
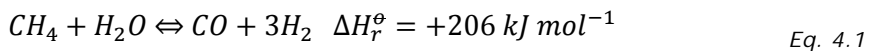
4.1. Introduction

Biogas is produced from biomass mainly through anaerobic digestion of organic substrates (manure, sewage sludge, organic fractions of industry waste and energy crops) [1]. The composition of biogas varies significantly depending on the source of biomass. Typical biogas compositions from an anaerobic digester and landfill production are shown in Table 4.1.

Table 4.1. Anaerobic digestion or landfill biogas composition [2].

Component	AD biogas	Landfill biogas	Unit
CH ₄	53-70	30-65	vol%
CO ₂	30-50	25-47	vol%
N ₂	2-6	<1-17	vol%
O ₂	0-5	<1-3	vol%
H ₂	N/A	0-3	vol%
C _x H _y	N/A	N/A	vol%
H ₂ S	0-2000	30-500	ppm
NH ₃	<100	0-5	ppm
Chlorines	<0.25	0.3-225	mg Nm ³
Siloxane	<0.08-0.5		µg/g-dry

The methane in the biogas can be converted into a hydrogen rich gas by steam reforming (SR): methane reacts with steam at high temperatures over a nickel-based catalyst to produce CO and H₂ via the Steam Methane Reforming reaction (SMR), Eq. 4.1. To increase the hydrogen yield this process is combined with Water Gas Shift (WGS), Eq. 4.2. Because of the high CO₂ content, Dry Reforming (DR), Eq. 4.3, is likely to take place as well.



The reforming of methane is highly endothermic and requires high temperatures (800 - 1000 °C) and is favoured at low pressures. Moreover, to obtain high purity hydrogen from the SR process, downstream separation and purification steps are required. The application of biogas in the SR process has significant challenges: (i) the combination of the nickel catalyst and high operation temperatures makes the system prone to coking, (ii) the high CO₂ content of biogas induces equilibrium limitations and (iii) the presence of H₂S even if present in trace amounts requires intensive cleaning of the biogas. The development of reforming catalysts with a high resistance to carbon formation have increased the potential for hydrogen production from biogas [3]. Noble metal catalysts, such as Rh, Ru, Pt and Pd show a high activity and selectivity for hydrogen production [4]. Generally Rh has been found to have the best performance along the different noble metal catalysts. To remove the H₂S, the biogas can be upgraded by cleaning using e.g. pressurized water scrubbing, pressure swing adsorption, amine absorption or membrane absorption [2]. However, these methods significantly increase the energy consumption and costs of hydrogen [2]. Previous works investigated the application of biogas steam reforming in a membrane reactor [5–7]. Sato et al. [5] identified the membrane reactor as a promising technology for hydrogen production from biogas. In this work, steam reforming of a biogas mixture derived from supercritical water gasification of glucose was performed using a PdAg supported on stainless steel membrane in a fixed bed containing a Ru/Al₂O₃ catalyst. Iulianelli et al. [6] studied the steam reforming of biogas in a Pd-based membrane on a porous Al₂O₃ support over a Ni catalyst. Methane conversion of 34% and separation of the produced hydrogen up to 70% were reported. However, the process required regeneration of the catalyst deactivated by carbon formation, and the hydrogen purity was decreased rapidly due to the formation of pinholes. Vasquez et al. [7] investigated the effect of the temperature and pressure on the steam reforming in a fixed bed and described their experiments with a one-dimensional model. However, the use of fixed-bed reactors has some drawbacks, in particular when applied to membrane reactors with high fluxes. First of all, the poor heat transfer in the packed bed results in large temperature gradients, which can be detrimental for the membrane flux and membrane stability. Moreover, when high-flux membranes are used, mass transfer limitations from the bulk to the membrane wall, known as concentration

polarisation (CP), become dominant and negatively impact the reactor performance [8,9]. CP, is a depletion of the permeable species at the wall resulting in a lower driving force. As shown in the schematic description in Figure 4.1, the higher permeability of the membrane compared to the mass transfer results in a concentration gradient towards the membrane. The region in which the hydrogen concentration differs from the bulk concentration is referred as the concentration polarization layer.

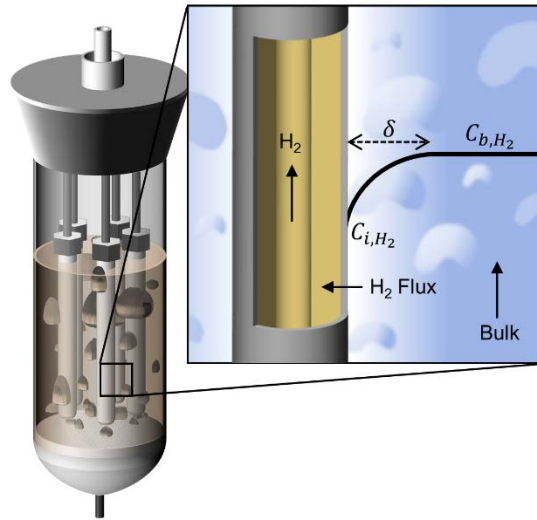


Figure 4.1. Schematic representation of concentration polarization in a fluidized bed membrane reactor.

These aspects can be reduced by using fluidized bed membrane reactors, which have significantly higher heat and mass transfer rates compared to fixed bed membrane reactors, resulting in advantages in terms of heat management and a much more even temperature distribution [10]. Moreover, it is expected that the higher mass transfer rates also result in a reduction of the concentration polarisation. However, the concentration polarisation is still expected to influence the system performance significantly and needs to be accounted for in the design of the reactor.

This chapter evaluates the performance of a fluidized bed membrane reactor for biogas steam reforming and the influence of concentration polarisation on the system performance. The effect of concentration polarisation is first analysed

experimentally for hydrogen/nitrogen mixtures with and without the fluidized bed. The steam reforming of synthetic biogas mixtures (mainly CO_2 and CH_4) as well as pure methane is evaluated for temperatures between 430 °C and 530 °C and pressures up to 5 bar. The results are discussed, followed by the description and validation of a developed phenomenological, one-dimensional, two-phase fluidized bed membrane reactor model. The model is then used to quantify the influence of the concentration polarisation and its significance for the design of fluidized bed membrane reactors for biogas reforming.

4.2. Experimental

4.2.1. Experimental setup

Single and mixed gas permeation tests to characterize the membrane performance and reforming experiments, were conducted in a membrane reactor consisting of a shell-and-tube configuration (see Figure 4.2) where the reactor has a diameter of 4.27 cm and a total length of 44 cm. The membrane is made of a thin Pd-Ag layer deposited by electroless plating onto an alumina porous tube obtained from Rauschert. The membrane was sealed using the graphite sealing method developed by Fernandez et al. and the leakage was subsequently measured using an helium/ethanol system [11]. The length of the membrane was 14.35 cm and its diameter 14.26 mm, resulting in a total membrane surface area of 64.3 cm^2 . The membrane thickness was measured by SEM (Phenom) analysis on a cross section of the membrane and was found to be 5.2 μm . The membrane was integrated from the top flange of the reactor with a stainless-steel tube, such that 2 cm remained between the bottom gas distributor and the bottom membrane seal. Single and mix gas experiments were performed first without catalyst particles, here referred to as empty tube. After these experiments the catalyst, a Rh-based catalyst supplied by Johnson Matthey (average particle size of 170 μm), was loaded into the reactor to perform the mix gas tests under fluidized conditions and subsequently the (steam) reforming experiments. The reactor system could be operated in two configurations, viz. as a normal fluidized bed reformer and as a fluidized bed membrane reactor, simply by opening and closing of the membrane permeate line. The minimum fluidization velocity of the catalyst was experimentally determined at different temperatures and

atmospheric pressure using the standard pressure-drop method. The feed flow rate for reactive experiments was selected in such a way that the fluidized bed was in the bubbling fluidization regime. The amount of catalyst was selected to cover the full active membrane surface, resulting in 165 g of catalyst. The reactor was placed inside an oven to ensure isothermal operation. In the reforming experiments the temperature, pressure and feed gas composition were varied. The system performance was evaluated in terms of methane conversion (Eq. 4.4), separation factor (SF, Eq. 4.5) and hydrogen recovery factor (HRF, Eq. 4.6) as defined below:

$$\text{Methane conversion} = \frac{F_{CH_4,in} - F_{CH_4,out}}{F_{CH_4,in}} \quad \text{Eq. 4.4}$$

$$\text{Separation factor} = \frac{F_{H_2,perm}}{F_{H_2,perm} + F_{H_2,ret}} \quad \text{Eq. 4.5}$$

$$\text{Hydrogen recovery factor} = \frac{F_{H_2,perm}}{4F_{CH_4,in}} \quad \text{Eq. 4.6}$$

The gas feed to the reactor was controlled by Bronkhorst® digital mass flow controllers. The feed of water was controlled by a Bronkhorst® Coriflow liquid meter and steam was produced using a Bronkhorst® controlled evaporator mixer. The pressure was controlled by a back-pressure regulator supplied by Bronkhorst®. The permeate side was either operated at atmospheric pressure or at vacuum. The volumetric flow rate at the permeate side was measured using a Horiba film flow meter. The composition of both the permeate and retentate streams were measured using a Varian micro GC equipped with two molecular sieve 5A columns and a PoraPlot Q column. The retentate flow rate is obtained from the nitrogen balance. The carbon balance was satisfied with $\pm 5\%$ error for all experiments reported hereafter.

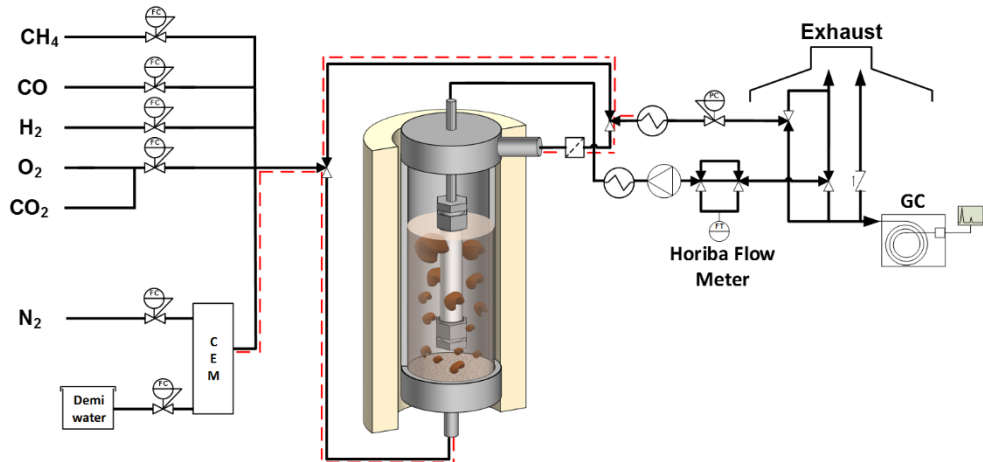


Figure 4.2. Schematic representation of the experimental setup.

4.2.2. Membrane performance characterization

Once the membrane was placed in the reactor, the nitrogen leakage was monitored periodically. To activate the membrane, the system was heated up to 400 °C in nitrogen, once at this temperature the membrane was exposed to 2 NI/min of air for 2 minutes. Subsequently, the system was flushed with nitrogen and heated up to 550 °C and left in a hydrogen environment until a stable hydrogen flux was obtained. After reaching stable conditions, the permeation tests were performed decreasing the oven temperature from 550 °C to 400 °C with steps of 50 °C; the results are shown in Figure 4.3. The hydrogen permeability of the membrane could be well described as a function of the driving force using an exponent n equal to 0.5 (i.e. Sieverts' law), as shown in Figure 4.3. An activation energy and a pre-exponential factor of respectively 9.23 kJ/mol and $4.57 \cdot 10^{-8} \text{ mol m}^{-1} \text{ s}^{-1} \text{ Pa}^{-0.5}$ were fitted to the experimental data. These values are comparable with the 9.99 kJ/mol and $6.93 \cdot 10^{-8} \text{ mol m}^{-1} \text{ s}^{-1} \text{ Pa}^{-0.5}$ reported earlier by Fernandez et al. for a similar membrane [12]. The initial H₂/N₂ ideal perm-selectivity was found to be 18000 at 545 °C and 4576 at 384 °C with a transmembrane pressure difference of 1 bar.

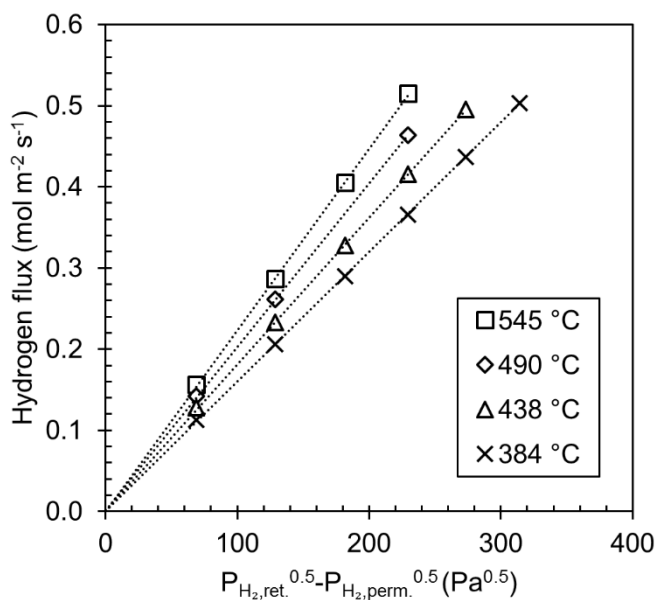


Figure 4.3. Single gas test permeation results of hydrogen.

4.2.3. Model description

The reactor model developed in this work describes a membrane fluidized bed section in which a dead-end perm-selective membrane can be integrated. It is an improvement of the model described by Gallucci et al. [13]. The model was firstly developed by Deshmukh et al. and based on the frequently used bubble assemblage model proposed by Kato and Wen [14,15]. In this approach, both the bubble and emulsion phases are divided into a number of CSTRs along the reactor. In particular, Kato and Wen related the volume of the CSTR to the local bubble size, whereas Deshmukh et al. adopted a different approach where the CSTRs all have the same volume and the number of CSTRs is used describe the amount of gas back mixing in the system [14,16]. The steady state overall (bubble and emulsion phases) component mass conservation equations, the total volume balance and the overall balances for each component used in the model are formulated in Table 4.2. These equations consider the chemical transformations in the emulsion phase and a net gas production due to the chemical reactions and gas extraction via the membrane. The equations are solved for each section in the fluidized bed reactor. Since the introduction of membranes reduces the extent of back mixing, a large number of CSTRs is selected representing plug flow

behaviour. The empirical correlations for the description of the system hydrodynamics and mass transfer are obtained from literature and are described in Appendix I [15,17–19]. Although these equations are developed for fluidized beds without membranes, it is shown in prior works that a reasonable description of the system with immersed membranes can also be obtained [13,16]. The chemical reactions are described using the kinetic rate laws by Numaguchi and Kikuchi for the steam reforming and water gas shift reactions [20]. The kinetic parameters for the Rh based catalyst are obtained from Marra et al. [21]. The rate expressions and kinetic parameters are provided in Appendix II. Because of the high steam-to-carbon ratio applied in the experimental conditions the dry reforming reaction can be assumed to be of negligible influence in the reaction system. This was also confirmed by separate kinetic tests reported in Appendix III. Moreover, it was shown that the kinetics did not play a significant role on the experimental results due to the high catalyst activity.

Table 4.2. Mass balance equations for each CSTR in each section of the fluidized bed membrane reactor [22].

Total mass balance

$$\begin{aligned}
 & u_{b,n-1}^s A_T \rho_{b,n-1} - u_{b,n}^s A_T \rho_{b,n} + u_{e,n-1}^s A_T \rho_{e,n-1} - u_{e,n}^s A_T \rho_{e,n} \\
 & + \sum_{i=1}^{n_c} (N_{i,mol}^{membrane} M_{w,i} A_{membrane} \varepsilon_{b,n}) \\
 & + N_{i,mol}^{membrane} M_{w,i} A_{membrane} (1 - \varepsilon_{b,n}) = 0
 \end{aligned}$$

Bubble phase component mass balance

$$\begin{aligned}
 & u_{b,n-1}^s A_T \rho_{b,n-1} - u_{b,n}^s A_T \rho_{b,n} - \sum_{i=1}^{n_c} K_{be,i,n} V_{b,n} \rho_{b,n} (w_{b,i,n} - w_{e,i,n}) \\
 & + \sum_{i=1}^{n_c} N_{i,mol}^{membrane} M_{w,i} A_{membrane} \varepsilon_{b,n} \\
 & + [w_{e,i,n} HSF(Q) - w_{b,i,n} HSF(-Q)] = 0
 \end{aligned}$$

Emulsion phase component mass balance

$$\begin{aligned}
 & u_{e,n-1}^s A_T \rho_{e,n-1} - u_{e,n}^s A_T \rho_{e,n} + \sum_{i=1}^{n_c} K_{be,i,n} V_{b,n} \rho_{b,n} (w_{b,i,n} - w_{e,i,n}) \\
 & + \sum_{i=1}^{n_c} N_{i,mol}^{membrane} M_{w,i} A_{membrane} (1 - \varepsilon_{b,n}) \\
 & - \left(\sum_{j=1}^{n_{rxn}} v_{j,i} r_j \right) V_{e,n} \rho_{p,n} (1 - \varepsilon_e) \\
 & + [w_{e,i,n} HSF(Q) - w_{b,i,n} HSF(-Q)] = 0
 \end{aligned}$$

Transfer term

$$\begin{aligned}
 Q &= u_{e,n-1}^s A_T \rho_{e,n-1} - u_{e,n}^s A_T \rho_{e,n} & \text{where} \\
 & + \sum_{i=1}^{n_c} K_{be,i,n} V_{b,n} \rho_{b,n} (w_{b,i,n} - w_{e,i,n}) & u_{b,0}^s A_T = u_{tot} A_T \varepsilon_{b,0} \\
 & \pm \sum_{i=1}^{n_c} N_{i,mol}^{membrane} M_{w,i} A_{membrane} (1 - \varepsilon_{b,n}) & u_{e,0}^s A_T = u_{tot} A_T (1 - \varepsilon_{b,0}) \\
 & & u_{e,n}^s A_T = u_{e,n} A_T (1 - \varepsilon_{b,n})
 \end{aligned}$$

The selective extraction of hydrogen in the model is described by Sieverts' law, Eq. 4.7, using the experimentally obtained parameters of the membrane.

$$N_i = \frac{P_0}{t} e^{-E_a/RT} \left(P_{H_2,ret}^n - P_{H_2,perm}^n \right) \quad \text{Eq. 4.7}$$

When describing hydrogen extraction from a mixture through a highly selective and permeable membrane, Sieverts' law is found to be insufficient to predict the transmembrane flux [23,24]. Due to the depletion of the permeable species near the membrane and accumulation of the non-permeable species, a mass transfer boundary layer is formed along the membrane (phenomena known as concentration polarisation). To account for the mass transfer limitations induced and accurately describe the membrane permeation, the concentration at the membrane surface is required. In this work, the stagnant film model is applied to determine the concentration at the membrane surface [25]. In the stagnant film model, the following assumptions are applied:

- Steady state conditions;
- No axial convection in the film layer;
- No axial dispersion, only radial dispersion.
- The thickness of the stagnant film is assumed to remain constant along the length of the membrane.

The boundary layer thickness is indicated with δ , see Figure 4.4. The steady state mass balance of the shell around a cylindrical membrane in the radial direction, as shown in Figure 4.4, leads to Eq. 4.8, where $N_{i,r}$ is the flux in the radial direction.

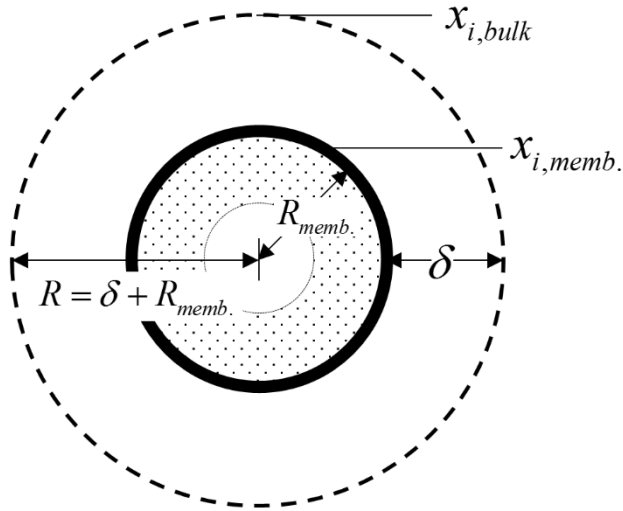


Figure 4.4. Schematic description of the film around the membrane.

$$-\frac{1}{r} \frac{d}{dr} (rN_{i,r}) = 0 \quad \text{Eq. 4.8}$$

The total flux through the film layer in the radial direction can be written as the sum of the drift flux and diffusive mole flux, Eq. 4.9, using the generalised Fick's law, where D_i represents the effective diffusivity of component i , C_{tot} the total concentration and x_i the mole fraction of component i

$$N_{i,r} = -D_i C_{tot} \frac{dx_i}{dr} + x_i N_{tot} \quad \text{Eq. 4.9}$$

Since the membrane can be approximated as fully permselective for H_2 , N_{tot} equals $N_{i,r}$, so further rearranging Eq. 4.9 leads to Eq. 4.10.

$$N_{i,r} = -D_i C_{tot} \frac{1}{1-x_i} \frac{dx_i}{dr} \quad \text{Eq. 4.10}$$

From the steady state mass balance, it follows that the term $rN_{i,r}$ is constant over the layer.

$$rN_{i,r} = c \quad \text{at} \quad r = R_{memb.} + \delta,$$

Eq. 4.11

$$N_{i,r} = N_{i,r_m+\delta}$$

Combining this and Eq. 4.10 and integrating over the boundary layer of thickness δ yields Eq. 4.12

$$N_{i,r_m} = - \frac{D_i C_{tot}}{R_{memb.} \ln\left(1 + \frac{\delta}{R_{memb.}}\right)} \ln\left(\frac{1 - x_{i,memb.}}{1 - x_{i,bulk}}\right) \quad \text{Eq. 4.12}$$

Since the flux through the film layer and membrane are equal, Eq. 4.12 can be used to determine $x_{i,memb.}$ and obtain the partial pressure of hydrogen at the surface of the membrane.

4.3. Results and discussion

4.3.1. Permeation of N₂ and H₂ mixtures

Gas permeation experiments were performed to determine the influence of the concentration polarisation on the membrane separation and to validate the implementation of the stagnant film in the model. Hydrogen permeation in the empty tube system (no catalyst bed) from a 75% H₂/N₂ mixture was measured at different total pressures. After these experiments the catalyst was loaded into the system. The presence of the catalyst should not influence the hydrogen permeation from a pure hydrogen mixture. However, the experiment with the 75% H₂/N₂ mixture showed that the flux was increased compared to the empty tube system. In Figure 4.5, the experimental results are shown together with the model results.

The extent of the concentration polarisation can be represented by the Concentration Polarisation Coefficient (CPC). Several definitions of the CPC exist

in literature; however, in this work the definition presented by Caravella et al. is used [23], taking the logarithmic average into account in determining the pressure difference over the module. The CPC for both the results of the empty and fluidized bed system permeation tests are shown in Figure 4.6. The concentration polarisation coefficient is reduced by the introduction of the fluidized bed from 0.41 to 0.32 at 3 bar, and at 5 bar is decreased from 0.52 to 0.34.

Because the model without concentration polarisation does not take mass transfer limitations into account, the hydrogen flux is over-predicted. This shows that a description taking the concentration polarisation into account is indeed required in the model. To describe the permeation results in the empty tube system, a δ of 1.125 cm was fitted to the experiment at 4 bar total pressure. In the work of Helmi et al. [26] it is shown that the radial dispersion in the fluidized bed is larger than the molecular gas diffusion coefficient D_i . Since there is no general correlation available for the radial dispersion in membrane fluidized beds its value was estimated using CFD simulations at $1 \cdot 10^{-4} \text{ m}^2/\text{s}$, which was also adopted in this work. Accordingly, a δ of 0.975 cm was found to correctly describe the hydrogen flux. The increase in the hydrogen flux in the fluidized bed compared to the empty system can thus be explained by the increase of the radial dispersion of the system due to the bubbling behaviour of the fluidized bed resulting in a decrease in δ .

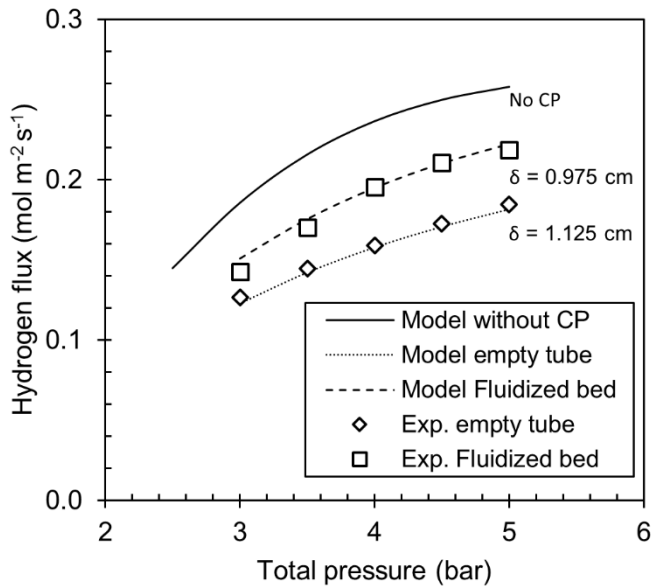


Figure 4.5. Permeated hydrogen flux at different total pressures from a 75% H_2/N_2 mixture at 380 °C, with a total feed flow of 3.6 NI/min.

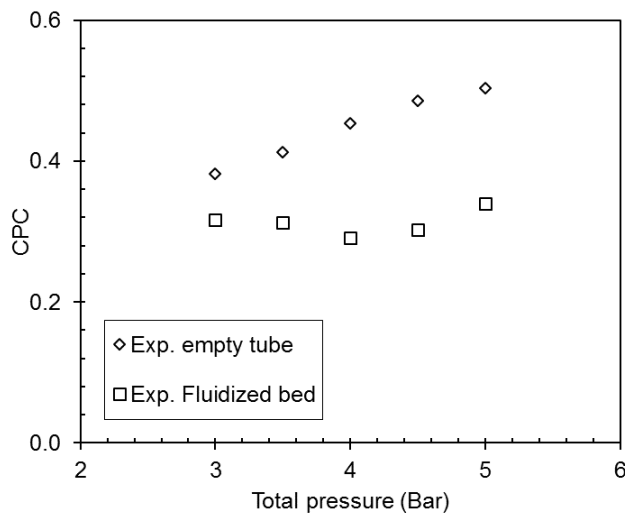


Figure 4.6. Concentration polarisation coefficient for the empty tube and the fluidized bed system at different pressures.

Figure 4.7a shows the film layer thickness at 3 bar fitted for different feed fractions of hydrogen in the system without fluidized bed for different total feed flow rates. To indicate the effect of hydrogen depletion on the results, the bars in Figure 4.7 show the inlet and outlet fraction of hydrogen of the system. The film layer

thickness increases with an increase in the partial pressure of hydrogen, roughly between 6 and 12 mm. Analysis of the conditions of these results show that the decrease in δ with a decrease in the partial pressure of hydrogen and fluidization velocity is related to the increase in the Reynolds number of the system, as shown in Figure 5b, demonstrating the strong influence of the hydrodynamics on the extent of concentration polarisation. However, for the fluidized bed there is no correlation available to get a good estimation of the δ as a function of the different operating conditions. Therefore, in this work δ is considered as an adjustable parameter in the model and obtained by fitting to the results of a base case reforming experiment performed at the following conditions: 480 °C, a total pressure of 3 bar, a total feed flow rate of 3.6 NI/min and a feed distribution of $\text{CH}_4:\text{CO}_2:\text{H}_2\text{O} = 1:0.7:3$. The δ obtained from the fitting was 0.54 cm as a result of the more vigorous hydrodynamics of the fluidized bed; this constant δ is further used to describe all reforming experiments presented in the following analysis. The CPC for the system with biogas reforming was found to be 0.78, with the use of the hydrogen concentrations obtained from the model.

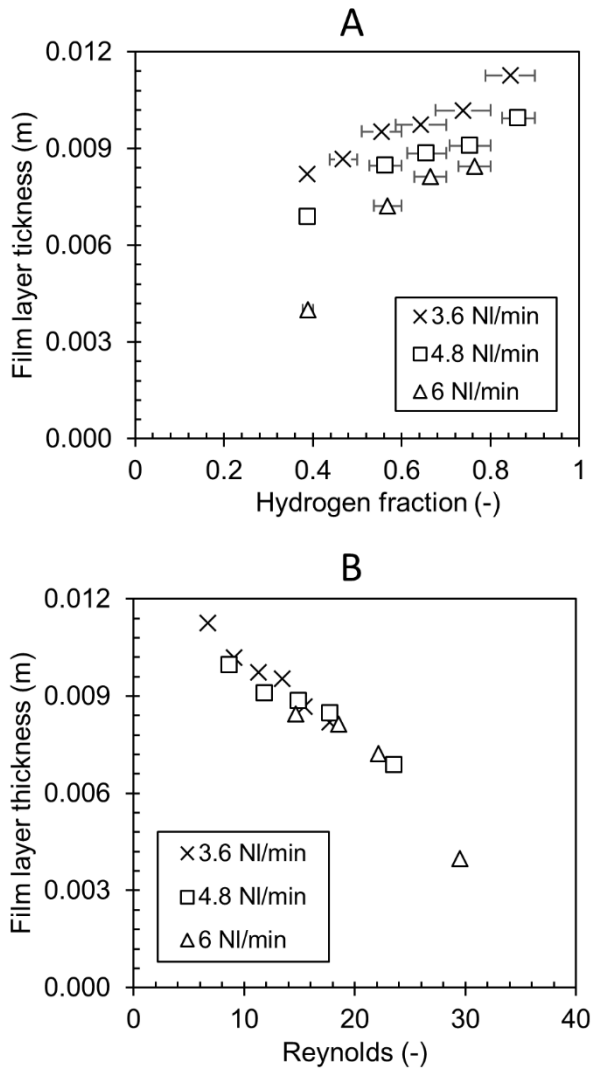


Figure 4.7. A: Film layer thickness for different hydrogen fractions at 3 bar and 370 °C for different total feed flow rates in system without fluidized bed. B: the thickness of the boundary layer as function of the Reynolds number.

4.3.2. Biogas steam reforming

To validate the model for the reforming of synthetic biogas, experiments were carried out at temperatures between 430 °C and 540 °C, with CO₂/CH₄ feed ratios ranging from 0 to 0.9, pressures from 2 bar up to 5 bar and a range of steam-to-carbon ratios (SCR) from 2 to 4. The stability of the system was monitored using

the before-mentioned base case experiment together with the performance of the membrane. The nitrogen and hydrogen permeability of the membrane increased over time: the fluidization roughens the membrane surface increasing the active area for hydrogen permeation, but also creating defects for nitrogen to pass. The discrepancy between the model and experiments was therefore higher for the experiments varying the SCR, as they were performed in a later stage of the system. All other results showed good agreement with the model and the use of one single δ showed to be sufficient over the investigated experimental ranges. From Figure 4.8 to Figure 4.11 the experimental results together with the model predictions are shown in terms of methane conversion, SF and HRF. The effects of the studied parameters will be further elaborated to show the effects and the differences between methane steam reforming (MSR) and biogas steam reforming (BSR). The impact of the temperature is studied for three different values, a comparison is made between MSR and BSR, all the other parameters are studied with and without the selective extraction of hydrogen. In all cases, the experimental results and the model predictions fit with the predicted equilibrium conversion. The cases without extraction of hydrogen behaved as expected for SMR: the methane conversion increases with temperature due to the endothermic nature of the system (Figure 4.8); a decrease in the methane conversion with increasing pressure as a result of the negative effect of pressure on the SMR reaction (Figure 4.9) and when the CO₂ concentration in the feed is increased, to form the synthetic biogas mixture, the conversion reduces due to the high concentration of CO₂ (Figure 4.8 and Figure 4.10). The increase in H₂O content on the other hand had a positive effect on the methane conversion, since this is a reactant forcing the equilibrium to the product side (Figure 4.11). When hydrogen was extracted from the system the equilibrium was shifted upwards. The extent of this shift depends on the permeability of the membrane and the transmembrane driving force. Focusing on temperature, the permeability of the membrane increases with temperature showing a higher SF and HRF and thus increases the conversion. A maximum methane conversion of 72% and 68% for respectively MSR and BSR at 533 °C was obtained. The transmembrane pressure is strictly related to the system pressure, therefore increasing the pressure results in an increase of SF as well as HRF. Over the tested range, the conversion increased by

50% to 105% with respect to the conversion without membrane. Although, it was not possible to work at higher pressures in the experimental system it can be expected that at higher pressure, hence higher HRF, the conversion would increase with pressure. In this way, the system can overcome the negative effect of the pressure on the SMR reaction. The study of different BSR mixtures with different CO_2/CH_4 ratios showed a constant shift in equilibrium, as the SF was not affected by the higher feed rate of CO_2 . The equilibrium conversion and HRF still decreased with an increase in the CO_2 fraction and the concentration of CO was increased on the retentate side with increasing CO_2/CH_4 , showing the effect of the CO_2 on the WGS equilibrium. CO poisoning could be assumed to be negligible, as the SF was not affected and considering the temperature the experiments were performed at [27]. The dilution effect of CO_2 could not be studied well in these experiments since the system feed was balanced with CO_2 , later performed experiments with lower dilutions also showed no significant effect of an increase in the CO_2 content in the feed on the SF. As mentioned before, the methane conversion increases with higher SCR, however, also the shift showed a small increase. This increase in shift can be explained as follows: as more hydrogen is produced, also the transmembrane pressure difference is increased, which can be seen from a slight increase in SF. During the experiments, there was no indication of carbon formation, and after the experiment no carbon was visible in the system or on the membrane.

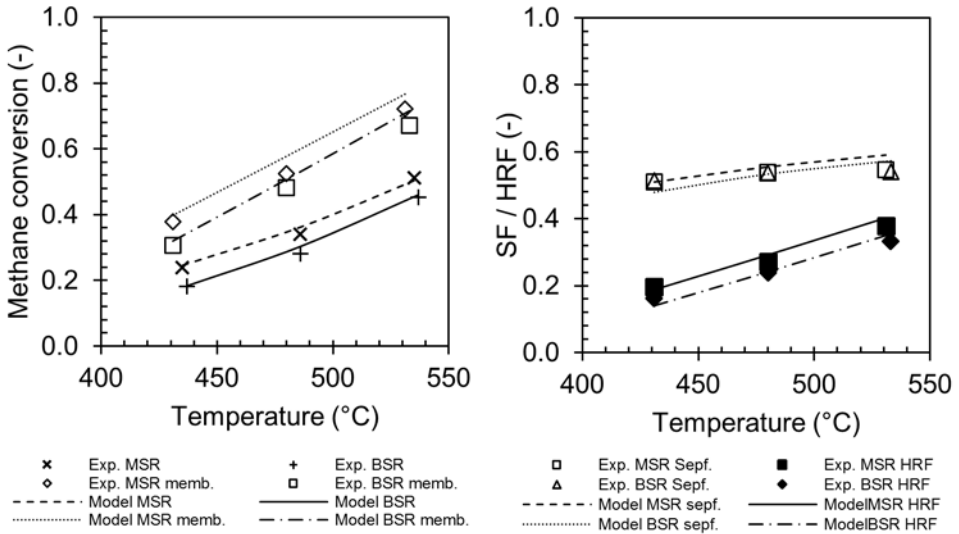


Figure 4.8. Methane conversion, SF and HRF of SMR and BSR ($CO_2/CH_4 = 0.7$) as a function of temperature at 3 bar, a total feed of 3.6 NI/min with 10% of methane and a SCR of 3.

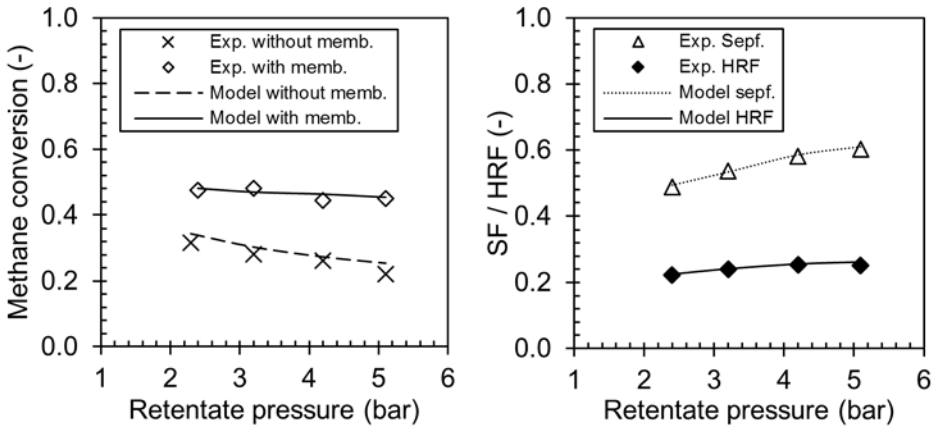


Figure 4.9. Methane conversion, SF and HRF for different pressures at 480 °C, a total feed of 3.6 NI/min with 10% of methane and a SCR of 3.

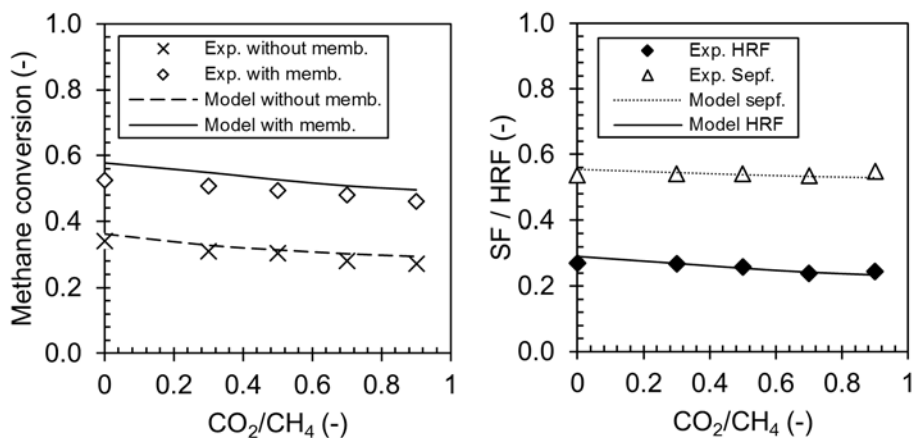


Figure 4.10. Methane conversion, SF and HRF for different CO_2/CH_4 ratios at 480 °C, 3 bar, a total feed of 3.6 NI/min with 10% of methane and a SCR of 3.

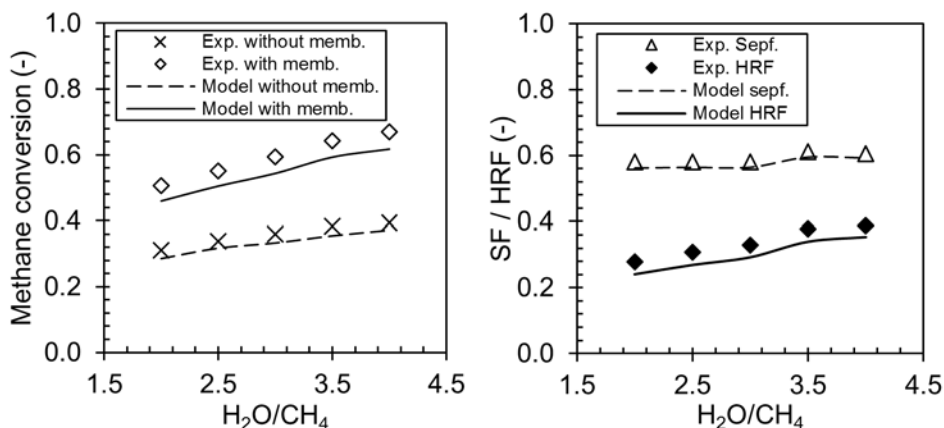


Figure 4.11. Methane conversion, SF and HRF for different SCRs at 480 °C, 3 bar and a total feed of 3.6 NI/min with 10% of methane.

The methane conversion, SF and HRF are important parameters to assess the reactor performance, although the purity of the hydrogen is as important to demonstrate the potential of the presented concept for biogas steam reforming. The permeate composition for the different cases is reported in Figure 4.12. The minimum amount of CO that was detected at the permeate side in the experiments was 146 ppm, in the other cases the GC was not detecting any CO and the amount can be assumed to be at least lower than 146 ppm. CO was found in three cases, where in two of the cases the CO concentration in the system was relatively high as a result of the high CO_2/CH_4 ratio or the low SCR, while in the other case the

temperature was lower (437 °C) resulting in a lower hydrogen flux. The hydrogen purity is strongly affected by the temperature, because it affects the hydrogen flux as consequence of the increased hydrogen permeability and methane conversion at higher temperatures. The lowest and highest hydrogen purity found for BSR were 97.34% and 99.88% achieved at the lowest and highest operation temperature, respectively. This effect could also already be seen from the increase in the ideal selectivity during the membrane characterization.

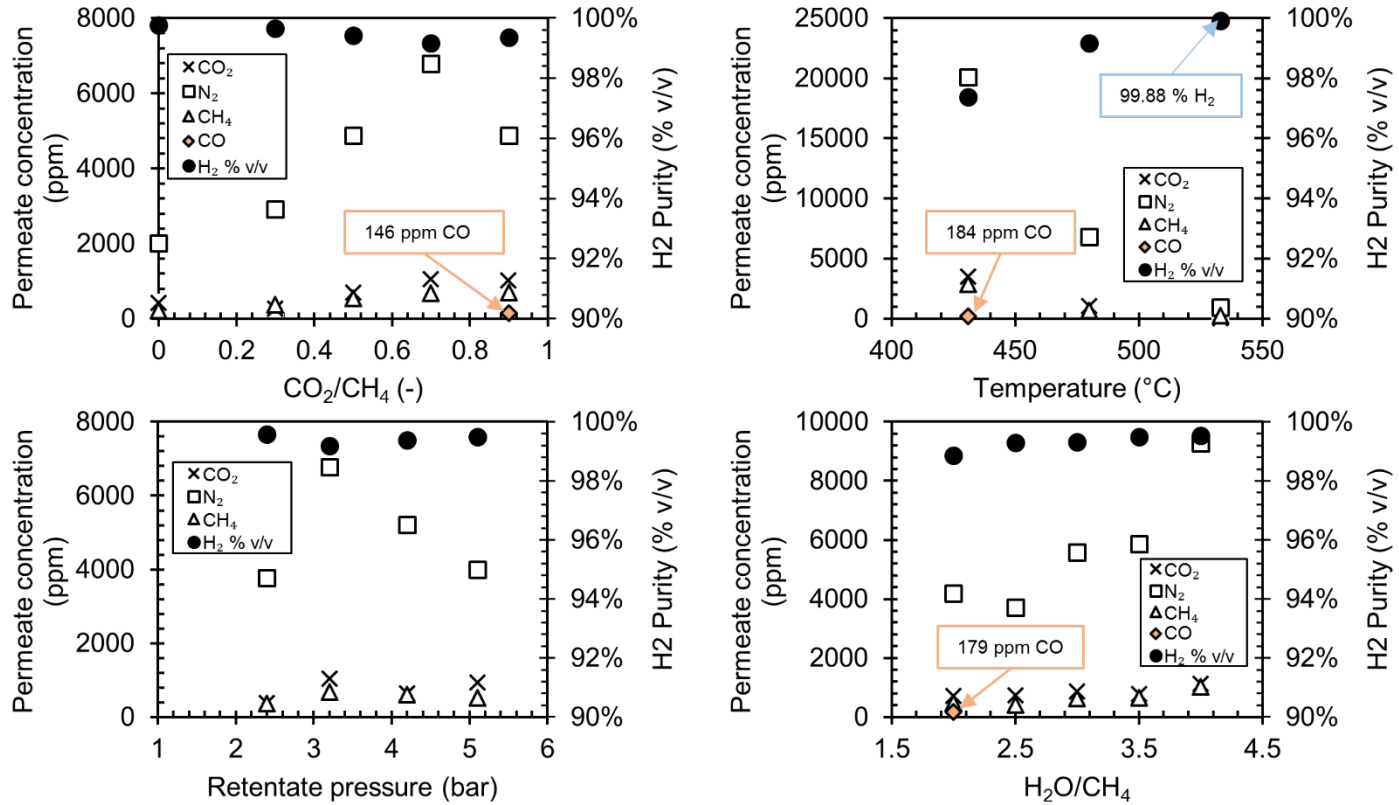


Figure 4.12 Permeate composition for: (a) CO₂/CH₄ ratio, (b) temperature, (c) pressure and (d) SCR.

4.3.3. Optimization and scale-up

To further validate the implementation of the concentration polarisation in the model, experiments with high dilution ratios were performed. From the results of these experiments a higher discrepancy with the model for the flux was observed. This can be discerned from Figure 4.13, where the high and the low dilution cases are compared. This discrepancy can be explained by the increase in the hydrogen partial pressure in the system and the change in validity of the assumed film layer thickness.

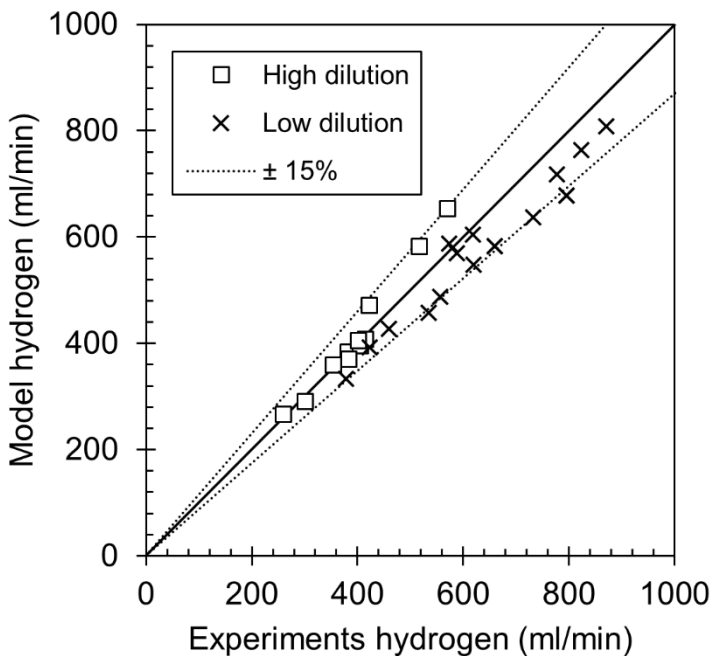


Figure 4.13. Parity plot of the predicted and measured hydrogen flow for high and low dilution conditions

Further scale up of the system to higher pressures would therefore require a new estimation of δ . However, no Sherwood correlation is available in the literature to describe the mass transfer from the bulk to the immersed membrane. To study the importance of the parameter δ , the validated model is used to evaluate this. To do this, the model was scaled up and the operation conditions were selected as for an industrial application. The system feed was selected as a representative biogas reforming mixture. Both the feed composition and the operation conditions

are listed in Table 4.3 and the computed concentration profile along the reactor length is shown in Figure 4.14.

Table 4.3. Conditions and feed composition used for the analyses of the scaled-up system.

Parameter	value	Unit
Pressure	12	bar
Temperature	550	°C
Permeate pressure	0.1	bar
H ₂ O/CH ₄	2.4	-
CO ₂ /CH ₄	0.76	-
N ₂ /CH ₄	0.37	-
u/u _{mf}	7.41	-

It can be seen, that in the first part most of the hydrogen is produced and the highest hydrogen concentration is reached. After this point the rate of hydrogen extraction becomes dominant over the rate of hydrogen production, and therefore the hydrogen concentration decreases along the reactor. Both the steam and methane concentration decrease along the reactor as they are converted. CO₂ is produced together with CO. A small difference can be outlined between the emulsion phase and bubble phase concentrations due to the influence of bubble-to-emulsion phase mass transfer limitations. This is not the case for the hydrogen transport, since in the model it was assumed that hydrogen is extracted from both the emulsion and bubble phase. To evaluate the importance of the thickness δ , the system was evaluated for three different cases: δ equal to 0.54 cm as resulted from the permeation experiments, a δ of 0.25 cm and 0.75 cm. The results of these calculations are shown in Figure 4.15. The thickness δ has a significant influence on the system performance. The conversion is shown as a function of the membrane productivity, indicating the amount of hydrogen that can be obtained per unit of membrane area. The productivity of the membranes decreases proportionally with the thickness of δ . Which means that a decrease in thickness δ of 25% leads in an increase of 25% in the productivity. These results not only highlight the importance of the film layer thickness on the design of

fluidized bed membrane reactors, but also indicate the potential of improving a membrane system by decreasing the concentration polarisation.

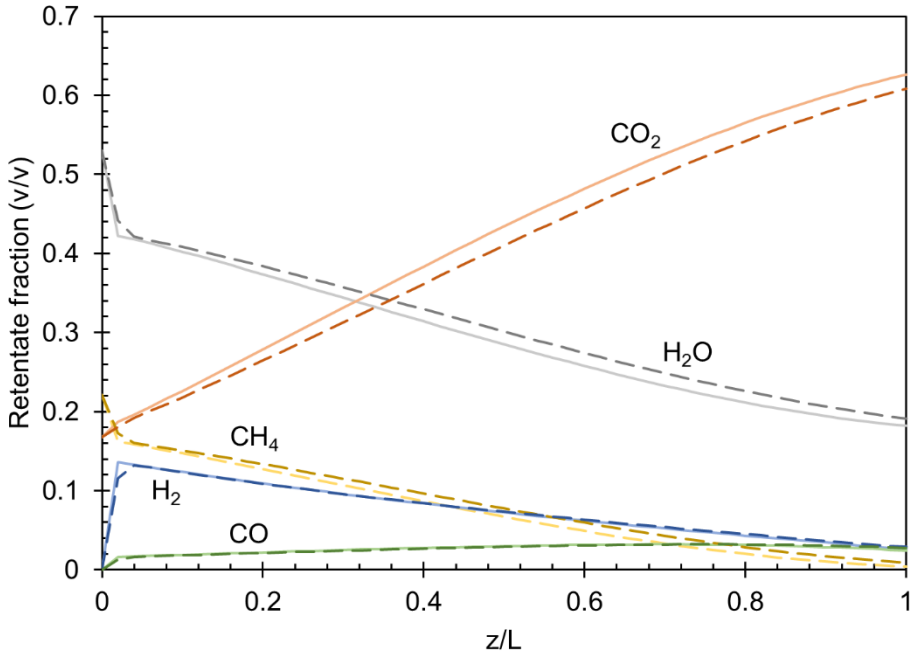


Figure 4.14. Composition along the reactor at 550 °C, 12 bar, load-to-surface ratio of $3 \text{ m}^3_{\text{CH}_4} \text{ m}^{-2}_{\text{memb.}} \text{ h}^{-1}$, continues lines and dashed lines represent respectively emulsion and bubble phase gas fractions.

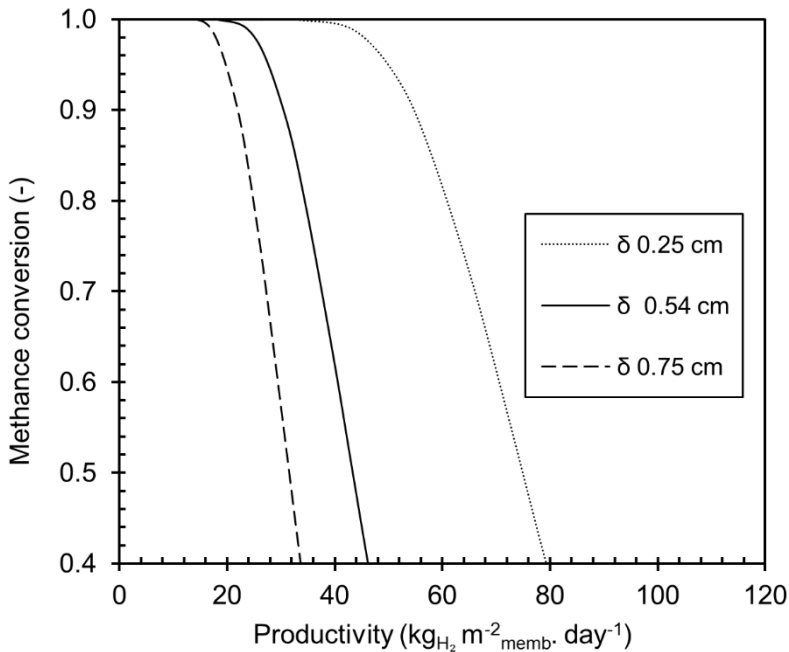


Figure 4.15. Membrane productivity as function of methane conversion for three different thicknesses of δ .

4.4. Conclusions

Hydrogen production via steam reforming of biogas has been experimentally investigated in a fluidized bed membrane reactor and the results were used to validate a phenomenological, one-dimensional, two-phase model, that was extended to account for concentration polarisation using a stagnant boundary layer film model. A Pd-Ag membrane supported on Al₂O₃ has been used both in an empty shell-and-tube configuration and in a fluidized bed with a Jonson Matthey Rh based catalyst. Permeation results in the two different system configurations were used to determine the thickness of the mass transfer boundary layer (δ). The importance of the hydrogen concentration and fluidization velocity on the extent of concentration polarisation is shown. A good description of the reforming experiments over the entire range of experimental conditions was obtained by the model when using the same thickness δ of 0.54 cm. Experiments with synthetic biogas mixtures showed lower conversions, however, the hydrogen separation was not affected and the previous estimation

of δ was shown to be adequate. However, when scaling up the system to higher dilution ratios showed larger discrepancies in the model predictions. The model was used to further scale up the system and study the dependency on the thickness δ . It was shown that the thickness significantly influenced the system productivity and scaled proportionally with the productivity.

Appendix

Appendix I Empirical correlations used in the model for the description of the system hydrodynamics and mass transfer.

Parameter	Equation	Ref.
Archimedes number	$Ar = \frac{d_p^3 \rho_g (\rho_p - \rho_g) g}{\mu_g^2}$	
Minimum fluidization velocity	$u_{mf} = \left(\frac{\mu_g}{\rho_g d_p} \right) \left(\sqrt{(27.2)^2 + 0.0408 Ar} - 27.2 \right)$	[18]
Bed voidage at minimum fluidization velocity	$\varepsilon_{mf} = 0.586 Ar^{-0.029} \left(\frac{\rho_g}{\rho_p} \right)^{0.021}$	[28]
Projected reactor area	$A_T = \frac{\pi}{4} D_T^2$	
Bubble diameter	$d_b = d_{b,max} - (d_{b,max} - d_{b,0}) e^{\left(\frac{0.3z}{D_T} \right)}$	[17]
Initial bubble diameter	$d_{b,0} = 0.376 (u_0 - u_{mf})^2$	[19]
Maximum bubble diameter	$d_{b,max} = \min \left(1.6374 A_T (u_0 - u_{mf})^{0.4}; D_T \right)$	
Average bubble diameter	$d_{b,avg} = \frac{d_{b,max} + (d_{b,max} - d_{b,0}) \frac{D_T}{0.3} \left(e^{-0.3 \frac{H_2}{D_T}} - e^{-0.3 \frac{H_1}{D_T}} \right)}{H_2 - H_1}$	
Average bubble rise	$u_{b,avg} = u_0 - u_{mf} + 0.711 (g d_{b,avg})^{0.5}$	

Emulsion velocity	$u_e = \frac{u_0 - f_b u_b}{1 - f_b}$	
Bubble phase fraction	$f_b = \frac{u_0 - u_{mf}}{u_{b,avg}}$	[15]
Emulsion phase fraction	$f_e = 1 - f_b$	
Initial superficial bubble gas velocity	$u_{b,0}^s = u_{b,0} f_{b,0} \quad f_{b,0} = \left(1 - \frac{H_{mf}}{H_f} \right)$	
Height of the bed at min. fluid. Velocity	$H_{mf} = H_s \frac{1 - \varepsilon_s}{1 - \varepsilon_{mf}}$	[29]
Height of bed expansion	$H_f = H_{mf} \frac{c_1}{c_1 - c_2}$	
	$C_1 = 1 - \frac{u_{b,0} e^{-\frac{0.275}{D_r}}}{u_{b,avg}}$	
	$C_2 = \frac{u_{b,0}^s}{u_{b,avg}} \left(1 - e^{-\frac{0.275}{D_r}} \right)$	
Gas exchange coefficient Bubble to cloud	$K_{bc} = 4.5 \left(\frac{u_{mf}}{d_{b,avg}} \right) + 5.85 \left(\frac{D_g^{0.5} g^{0.25}}{d_{b,avg}^{5/4}} \right)$	[19]
Cloud to emulsion	$K_{ce} = 6.77 \left(\frac{D_g \varepsilon_{mf} u_{b,avg}}{d_{b,avg}^3} \right)^{0.5}$	

Bubble to emulsion mass transfer resistance	$\frac{1}{K_{be}} = \frac{1}{K_{bc}} + \frac{1}{K_{ce}}$	
Binary diffusivities (m ² /s)	$D_g = \frac{10^{-3} T^{1.75} \left(\frac{1}{M_{w,i}} + \frac{1}{M_{w,j}} \right)^{\frac{1}{2}}}{P \left[V_{D,i}^{\frac{1}{3}} + V_{D,j}^{\frac{1}{3}} \right]^2}$ <p>Diffusion volumes taken from: [30]</p>	[31]

Appendix II Reaction rate laws and kinetic parameters

Reaction	Stoichiometry and reaction rate equation	Ref.
Methane steam reforming	$r_{SMR} = \frac{k_{SMR} \left(P_{CH_4} P_{H_2O} - \frac{P_{H_2}^3 P_{CO}}{K_{SMR}^{eq}} \right)}{P_{H_2O}^{1.596}}$	[20]
Water gas shift	$r_{WGS} = \frac{k_{WGS} \left(P_{CO} P_{H_2O} - \frac{P_{H_2} P_{CO_2}}{K_{WGS}^{eq}} \right)}{P_{H_2O}}$	
	$k_i = A_i e^{\left(\frac{E_{act,i}}{RT} \right)}$	
Constant	Value	Unit
A_{SMR}	$9.74 \cdot 10^4$	$\text{mol bar}^{-0.404} \text{kg}_{\text{cat}}^{-1} \text{s}^{-1}$
A_{WGS}	$17.2 \cdot 10^2$	$\text{mol bar}^{-1} \text{kg}_{\text{cat}}^{-1} \text{s}^{-1}$
$E_{act,SMR}$	$83.6 \cdot 10^3$	J mol^{-1}
$E_{act,WGS}$	$54.53 \cdot 10^3$	J mol^{-1}

[21]

Appendix III Kinetic evaluation

Catalyst

The catalyst, provided by Johnson Matthey, contained 2.5% Rh and 2.5% Ce that was impregnated onto a γ -alumina particles (average particle diameter of 250 μm) via incipient wetness impregnation from metal nitrates. The catalyst was subsequently calcined at 500 °C in air.

Kinetic setup

A setup designed for the measurement of catalyst activities and stabilities under reforming conditions was used. The catalyst and inert material were loaded into a quartz tubular reactor. The catalyst was supported by a small piece of glass wool. The catalyst, typically 20 mg, was first mixed with inert (quartz) particles in a ratio 'catalyst:inert' = 1:15. This resulted in a bed height of about 10 mm. On top of the catalyst bed quartz particles of 1-2 mm were placed to allow pre-heating of the feed gas. The out- and inlet temperature of the catalyst bed was monitored with thermocouples. A schematic representation of the reactor is shown in Figure 4.16. The reactor was placed inside a tubular oven. The feed and outlet system of the reactor was traced and insulated and was kept at 160 °C during the experiments. The gas feed was supplied by Brooks mass flow controllers. The steam feed was controlled by a Bronkhorst® mass flow controller and generated at 130 °C in a controlled evaporator mixer (CEM). The inlet and outlet flow was analysed by an online micro-GC with two mol-sieve (5A) columns and a poraplot Q (PPQ) column. The oven was heated with a flow of nitrogen at a heating rate of 3 °C/min to 550 °C. The catalyst was then exposed to a flow of 250 ml/min of air for 1 hour. After this the system was flushed with nitrogen and a flow of 500 ml/min 20% hydrogen in nitrogen was put for 30 minutes to reduce the catalyst. For all experimental results the mass balance obtained was closed within 1% error. All experiments used had a significantly lower conversion than the equilibrium conversion.

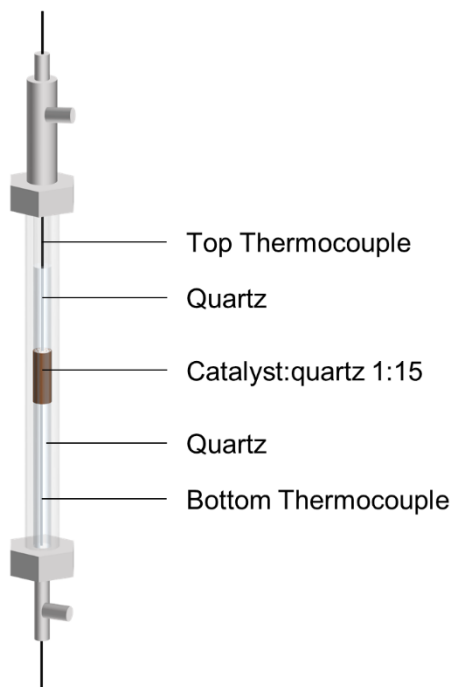


Figure 4.16. Schematic representation of the kinetics reactor.

Kinetic model

First it was verified whether the conversion rate was not limited by external or internal mass or heat transport limitations. Mears criterion was used to verify whether the reaction rate was influenced by external transport limitations. To avoid external mass transfer limitations, Mears criterion should be below 0.15, which was indeed the case [32]. In addition, absence of external mass transfer limitations was also experimentally evaluated. No change in conversion was measured when the total volumetric flow rate was varied while keeping the residence time with respect to methane constant. Influence of internal transport limitations was evaluated by the Weisz modulus [33]. A Weisz modulus < 0.25 was found, which indicates that the effectiveness factor is above 0.95. Calculating the effectiveness factor with the use of the (approximated) Thiele modulus an effectiveness factor above 0.99 was found, excluding a significant influence of internal mass transfer limitations. Also the influence of possible heat transfer limitations were checked, and both Mears criteria for absence of external and

internal heat transfer limitations were satisfied [34]. Table 4.4 summarizes the used criteria.

Table 4.4. Kinetic criteria for mass and heat transport limitations.

Mears criterion for external mass transfer limitations [32]

$$\frac{R_{obs} \rho_{cat} n}{C_{CH_4} k_c} \leq 0.15 \quad \text{where } k_c = Sh \frac{D_{eff}}{d_p} a_c$$

Weisz modulus for internal mass transfer limitations [33]

$$\frac{(n+1)R_{obs} \cdot \rho_{cat} (d_p / 6)^2}{2D_{eff} C_{CH_4}^s} < 0.25$$

Mears criterion for external heat transfer limitations [34]

$$\frac{|\Delta H_{rxn}^0| R_{obs} \cdot \rho_{cat} d_p E}{h_f T^2 R}$$

Mears criterion for internal heat transfer limitations [34]

$$\frac{|\Delta H_{rxn}^0| R_{obs} \cdot \rho_{cat} d_p E}{\lambda_p T^2 R}$$

Many works employing Rh catalysts for steam methane reforming refer to the work by Wei and Iglesia, that uses the assumption that the methane dissociation step is the rate limiting step and that the rate is first order in methane [35]. To investigate the validity of this assumption for the used catalyst, experiments with different partial pressures of methane at different temperatures were performed. A simple kinetic description, as shown in Eq. 4.13 and Eq. 4.14, was then used to describe the results at each temperature.

$$R_{SR} = k_{SR} p_{CH_4}^n (1 - \eta_{SR})$$

Eq. 4.13

$$R_{WGS} = k_{WGS} p_{CO} (1 - \eta_{WGS}) \quad \text{Eq. 4.14}$$

$$\eta_j = \frac{\Pi_i p_i^{v_i}}{K_{eq_j}} \quad \text{Eq. 4.15}$$

The water gas shift reaction is commonly assumed at equilibrium. However, the outlet composition of our experiments was relatively close to equilibrium, but not fully at equilibrium. The equilibrium values for the WGS reaction, η_{WGS} , as a function of the weight-to-feed ratio is shown in Figure 4.17.

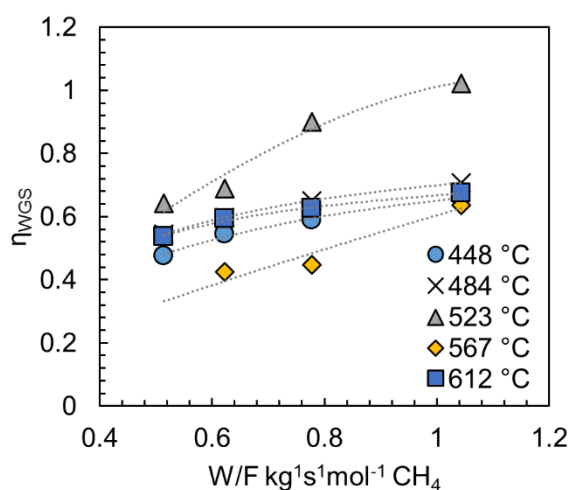


Figure 4.17. WGS equilibrium in the experiments versus weight to feed ratio (W/F) at 1.5 bar a SCR of 4 diluted with nitrogen.

A simple rate description for the water gas shift reaction with only a first order dependency on the partial pressure of CO was used. The experimental results are shown together with the fitted description in Figure 4.18, where for each temperature the reaction order of the methane steam reforming, n , was fitted separately, using a simple plug flow reactor model description assuming isothermal conditions, negligible pressure drop and no mass transfer limitations. It was found that a good description was only obtained with values for n below unity, which indicates that for our catalyst the description of Wei and Iglesia was not sufficiently adequate. Most likely the discrepancy is related to inhibition effects of co-reacting species, where this effect becomes somewhat less pronounced for higher temperatures, and the reaction order n in methane increases somewhat.

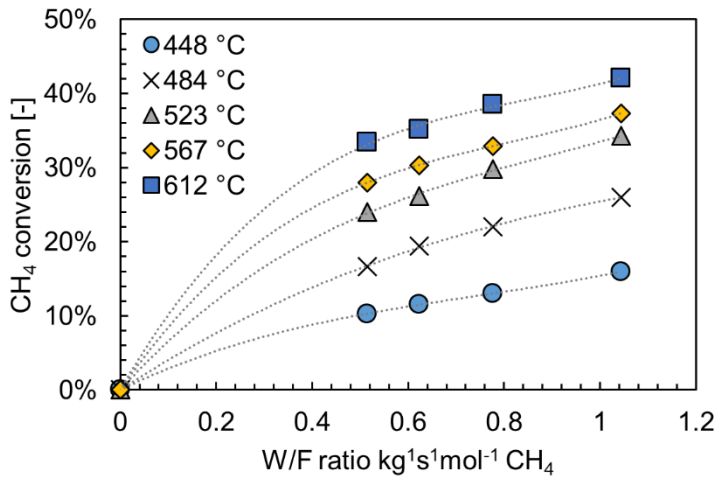


Figure 4.18. Total methane conversion for different Weight to feed ratios at 1.5 bar a SCR of 4 diluted with nitrogen.

Table 4.5. Kinetic parameters obtained from fitting.

	448 °C	484 °C	523 °C	567 °C	612 °C
k_{sr} [mol¹kg⁻¹s⁻¹kPa⁻ n]	0.45	0.71	1.08	1.92	2.53
n	0.33	0.33	0.35	0.49	0.52
k_{wgs} [mol¹kg⁻¹s⁻¹kPa⁻¹]	724.14	401.82	396.97	353.75	129.73

In the work by Jacobsen et al. the same effect is observed and a description with adsorption parameters for CO and H₂ is applied. To understand the effects of CO and H₂ on the performance of our catalyst, we performed CO and H₂ co-feeding experiments at a fixed temperature of 500 °C. The effects of the H₂ partial pressure in the feed are shown in Figure 4.19. A clear decrease in the methane conversion with an increase in the partial pressure of H₂ was observed. The description with only the methane reaction order (n) fitted without H₂ co-feeding was insufficient for this case, as the decrease in conversion was more extensive, and could be well described with the model by Jacobsen et al.

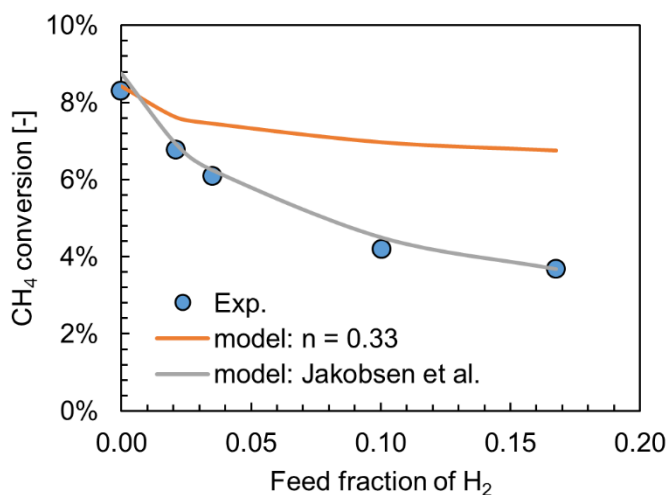


Figure 4.19. Results of co-feeding of H₂ at 500 °C with 10% methane and SCR of 4 in nitrogen.

In order to validate whether the kinetic rate expressions used in the phenomenological model were sufficiently adequate, the kinetics using a constant reaction order in methane, the kinetics by Jacobsen et al. and by Marra et al. have been compared in Figure 4.20. Clearly, the adsorption of CO and H₂ can have a significant impact on the methane conversion. The kinetic model assumed in this chapter was based on the kinetic description by Marra et al., which shows a significantly lower activity. To assess the influence of the reaction kinetics on the methane conversion in a fluidized bed membrane reactor, all three kinetic models were implemented in the phenomenological model. However, no differences in the obtained results could be found, as shown in Figure 4.21. The reason for this is the relatively slow separation of hydrogen in comparison to the fast reaction kinetics. Only when the catalyst was 100,000 times more diluted, effects could be noticed.

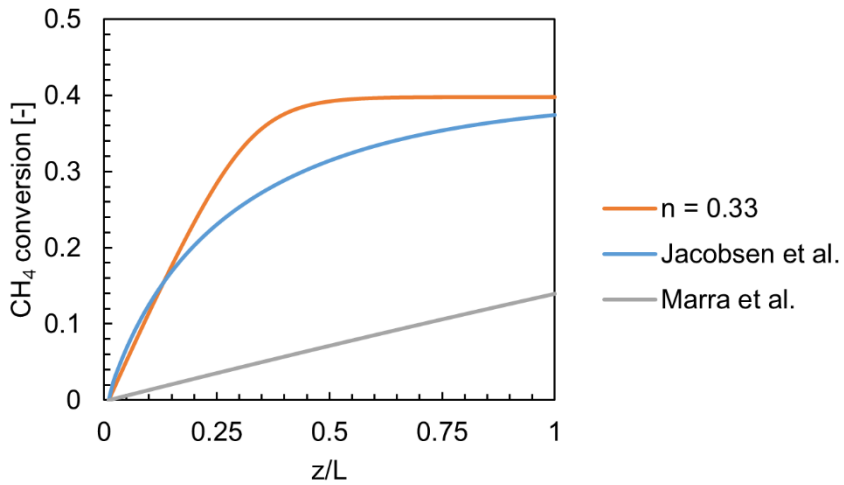


Figure 4.20. 100 ml/min 5% methane feed with SCR of 4 in nitrogen over 16 g of catalyst.

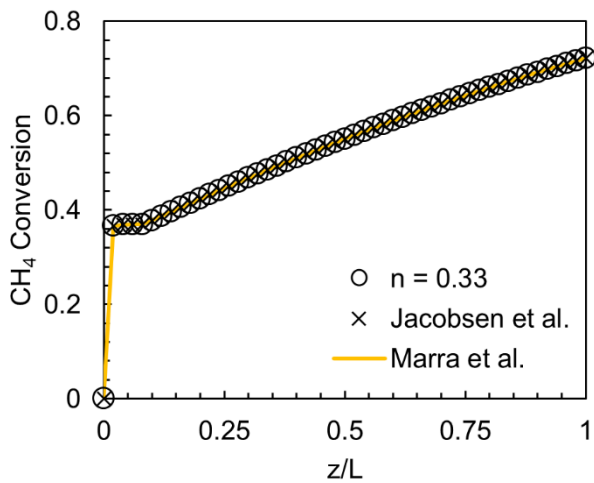


Figure 4.21. Kinetic comparison in the phenomenological model at 500 °C and 10 bar.

Nomenclature

Ar	Archimedes number
A_j	Arrhenius pre-exponential factor
A_T	Area of bed cross section [m ²]
$d_{b,0}$	Initial bubble diameter [m]
d_b	Bubble diameter [m]
$d_{b,avg}$	Average bubble diameter [m]
$d_{b,max}$	Maximum bubble diameter [m]
d_p	Particle diameter [m]
D_g	Gas diffusivity [m ² s ⁻¹]
D_T	Bed diameter [m]
$E_{act,j}$	Activation energy for reaction j
f_k	Fraction of phase k
F_i	Molar flow of species i [mol s ⁻¹]
g	Gravitational acceleration [m s ⁻²]
H_{mf}	Height of the bed at minimum fluidization velocity [m]
H_f	Height of the fluidized bed [m]
H_s	Height of the packed bed [m]
K_{ce}	Volumetric interchange coefficient between cloud and emulsion [s ⁻¹]
K_{bc}	Volumetric interchange coefficient between bubble and cloud [s ⁻¹]
$K_{be,i,n}$	Volumetric interchange coefficient between bubble and emulsion phase [s ⁻¹]

K_j^{eq}	Equilibrium constant for reaction j
$M_{w,i}$	Molar weight of component i [kg mol ⁻¹]
N_i	Molar flux component i [mol m ⁻² s ⁻¹]
p_0	Pre-exponential factor for permeability of membrane [mol m ⁻¹ s ⁻¹ Pa ⁻ⁿ]
P_i	Partial pressure of species i [bar]
r_j	Reaction rate of reaction j [mol kg ⁻¹ s ⁻¹]
$R_{memb.}$	Radius of the membrane
$HSF(Q)$	Heaviside function of Q
t	Thickness of Membrane selective layer thickness [m]
$u_{k,n}^s$	Superficial velocity of phase j in cell k [m s ⁻¹]
u_{mf}	Minimum fluidization velocity [m s ⁻¹]
u_0	Superficial gas velocity at inlet
u_b	Bubble rise velocity
$u_{b,avg}$	Average bubble rise velocity
$V_{D,i}$	Diffusion volume for component i
$V_{k,n}$	Volume of phase k in cell n [m ³]
$w_{k,i,n}$	Weight fraction of phase k, component i in cell n
$x_{i,bulk}$	Molar fraction of species i in the bulk
$x_{i,memb.}$	Molar fraction of species i adjacent to the membrane

Greek symbols

δ	Thickness of the stagnant film layer [m]
ΔH_r^θ	Reaction enthalpy at standard conditions [kJ mol ⁻¹]

$\mathcal{E}_{k,n}$	Fraction of phase k in cell n
\mathcal{E}_{mf}	Bed voidage at minimum fluidization velocity
μ_g	Gas viscosity [Pa s]
$\nu_{j,i}$	Stoichiometric coefficient of reaction j component i
$\rho_{k,n}$	Density of phase k in cell n [kg m ⁻³]

Subscripts

b	Bubble phase
e	Emulsion phase
g	Gas phase
i	Species
j	Reaction
n	Number of CSTR in emulsion or bubble phase
s	Solid phase

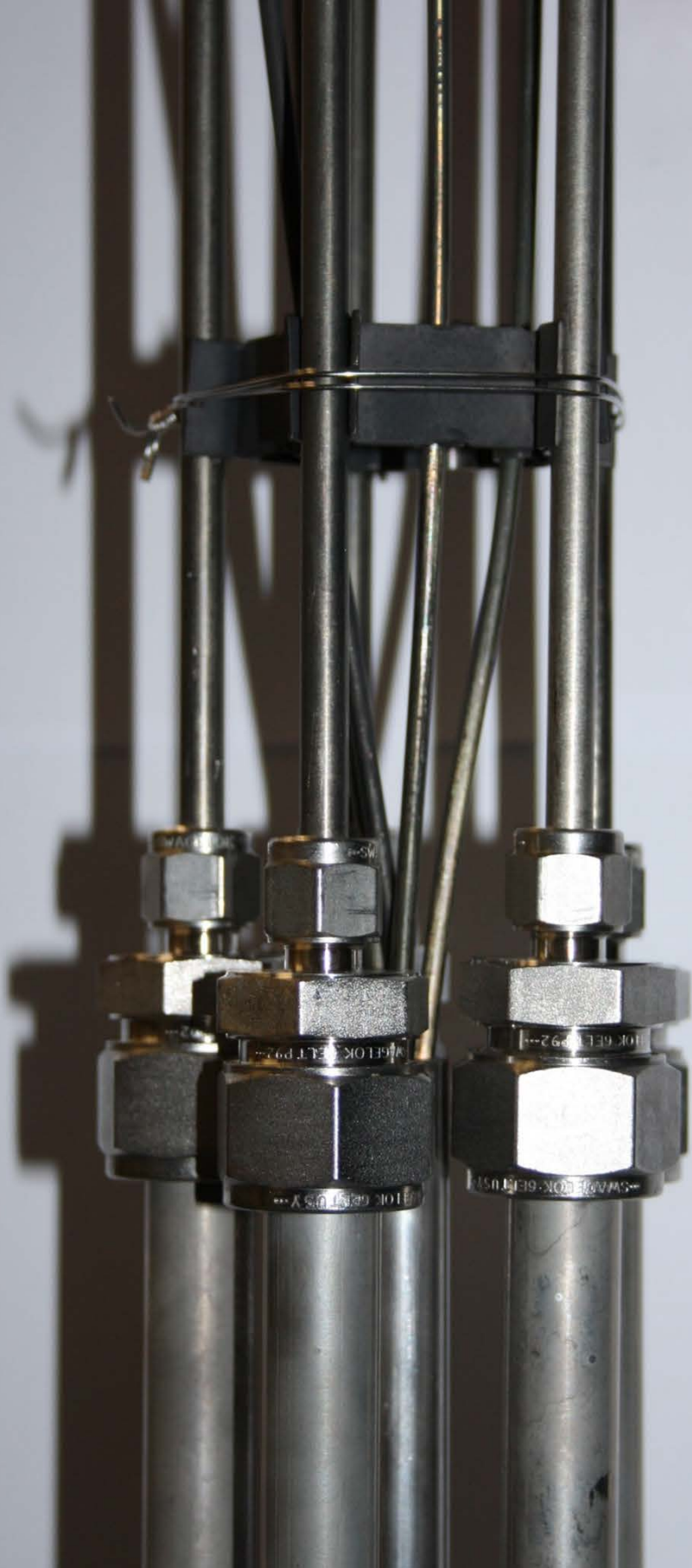
References

- [1] F. Van Foreest, Perspectives for Biogas in Europe, 2012.
- [2] L. Yang, X. Ge, C. Wan, F. Yu, Y. Li, Progress and perspectives in converting biogas to transportation fuels, *Renew. Sustain. Energy Rev.* 40 (2014) 1133–1152. doi:10.1016/j.rser.2014.08.008.
- [3] J. Xuan, M.K.H. Leung, D.Y.C. Leung, M. Ni, A review of biomass-derived fuel processors for fuel cell systems, 13 (2009) 1301–1313. doi:10.1016/j.rser.2008.09.027.
- [4] S.D. Angeli, G. Monteleone, A. Giaconia, A.A. Lemonidou, ScienceDirect State-of-the-art catalysts for CH₄ steam reforming at low temperature, *Int. J. Hydrogen Energy.* 39 (2013) 1979–1997. doi:10.1016/j.ijhydene.2013.12.001.
- [5] T. Sato, T. Suzuki, M. Aketa, Y. Ishiyama, K. Mimura, N. Itoh, Steam reforming of biogas mixtures with a palladium membrane reactor system, *Chem. Eng. Sci.* 65 (2010) 451–457. doi:10.1016/j.ces.2009.04.013.
- [6] A. Iulianelli, S. Liguori, Y. Huang, A. Basile, Model biogas steam reforming in a thin Pd-supported membrane reactor to generate clean hydrogen for fuel cells, *J. Power Sources.* 273 (2015) 25–32. doi:10.1016/j.jpowsour.2014.09.058.
- [7] J.M. Vásquez Castillo, T. Sato, N. Itoh, Effect of temperature and pressure on hydrogen production from steam reforming of biogas with Pd–Ag membrane reactor, *Int. J. Hydrogen Energy.* 40 (2015) 3582–3591. doi:10.1016/j.ijhydene.2014.11.053.
- [8] S. Hara, K. Sakaki, N. Itoh, Decline in Hydrogen Permeation Due to Concentration Polarization and CO Hindrance in a Palladium Membrane Reactor, (1999) 4913–4918.
- [9] N. Mori, T. Nakamura, K.I. Noda, O. Sakai, A. Takahashi, N. Ogawa, et al., Reactor configuration and concentration polarization in methane steam reforming by a membrane reactor with a highly hydrogen-permeable

- membrane, *Ind. Eng. Chem. Res.* 46 (2007) 1952–1958. doi:10.1021/ie060989j.
- [10] S. Volkers, H. Kuipers, Heat Transfer in a Membrane Assisted Bubbling Fluidized Bed with Immersed Horizontal Tubes Heat Transfer in a Membrane Assisted Bubbling Fluidized Bed with Immersed Horizontal Tubes, (2005).
- [11] E. Fernandez, A. Helmi, K. Coenen, J. Melendez, J.L. Viviente, D.A. Pacheco Tanaka, et al., Development of thin Pd-Ag supported membranes for fluidized bed membrane reactors including WGS related gases, *Int. J. Hydrogen Energy.* 40 (2015) 3506–3519. doi:10.1016/j.ijhydene.2014.08.074.
- [12] E. Fernandez, K. Coenen, A. Helmi, J. Melendez, J. Zuñiga, D.A. Pacheco Tanaka, et al., Preparation and characterization of thin-film Pd–Ag supported membranes for high-temperature applications, *Int. J. Hydrogen Energy.* (2015). doi:10.1016/j.ijhydene.2015.08.050.
- [13] F. Gallucci, M. van Sint Annaland, J.A.M. Kuipers, Autothermal reforming of methane with integrated CO₂ capture in a novel fluidized bed membrane reactor. Part 1: Experimental demonstration, *Top. Catal.* 51 (2008) 133–145. doi:10.1007/s11244-008-9126-8.
- [14] S.A.R.K. Deshmukh, J.A. Laverman, A.H.G. Cents, M.V.S. Annaland, J.A.M. Kuipers, Development of a Membrane-Assisted Fluidized Bed Reactor . 1 . Gas Phase Back-Mixing and Bubble-to-Emulsion Phase Mass Transfer Using Tracer Injection and Ultrasound Experiments, (2005) 5955–5965.
- [15] K. Kato, C.Y. Wen, Bubble assemblage model for fluidized bed catalytic reactors, *Chem. Eng. Sci.* 24 (1969) 1351–1369. doi:10.1016/0009-2509(69)85055-4.
- [16] S.A.R.K. Deshmukh, J.A. Laverman, M.V.S. Annaland, J.A.M. Kuipers, Development of a Membrane-Assisted Fluidized Bed Reactor . 2 . Experimental Demonstration and Modeling for the Partial Oxidation of Methanol, (2005) 5966–5976.

- [17] S. Mori, C.Y. Wen, Estimation of bubble diameter in gaseous fluidized beds, *AIChE J.* 21 (1975) 109–115. doi:10.1002/aic.690210114.
- [18] C.-Y. Shiau, C.-J. Lin, Equation for the superficial bubble-phase gas velocity in fluidized beds, *AIChE J.* 37 (1991) 953–954. doi:10.1002/aic.690370619.
- [19] D. Kunii, O. Levenspiel, *Fluidization Engineering*, Elsevier, 1991. doi:10.1016/B978-0-08-050664-7.50012-3.
- [20] T. Numaguchi, K. Kikuchi, Intrinsic kinetics and design simulation in a complex reaction network; steam-methane reforming, *Chem. Eng. Sci.* 43 (1988) 2295–2301. doi:10.1016/0009-2509(88)87118-5.
- [21] L. Marra, P.F. Wolbers, F. Gallucci, M.V.S. Annaland, Development of a RhZrO₂ catalyst for low temperature autothermal reforming of methane in membrane reactors, *Catal. Today.* 236 (2014) 23–33. doi:10.1016/j.cattod.2013.10.069.
- [22] F. Gallucci, M. Van Sint Annaland, J.A.M. Kuipers, Autothermal reforming of methane with integrated CO₂ capture in a novel fluidized bed membrane reactor. Part 2 comparison of reactor configurations, *Top. Catal.* 51 (2008) 146–157. doi:10.1007/s11244-008-9127-7.
- [23] A. Caravella, G. Barbieri, E. Drioli, Concentration polarization analysis in self-supported Pd-based membranes, *Sep. Purif. Technol.* 66 (2009) 613–624. doi:10.1016/j.seppur.2009.01.008.
- [24] F. Gallucci, M. Van Sintannaland, J.A.M. Kuipers, Theoretical comparison of packed bed and fluidized bed membrane reactors for methane reforming, *Int. J. Hydrogen Energy.* 35 (2010) 7142–7150. doi:10.1016/j.ijhydene.2010.02.050.
- [25] A.L. Zydney, Stagnant film model for concentration polarization in membrane systems, *J. Memb. Sci.* 130 (1997) 275–281. doi:10.1016/S0376-7388(97)00006-9.
- [26] A. Helmi, R.J.W. Voncken, A.J. Raijmakers, I. Roghair, F. Gallucci, M. van

- Sint Annaland, On concentration polarization in fluidized bed membrane reactors, *Chem. Eng. J.* 332 (2018) 464–478. doi:10.1016/j.cej.2017.09.045.
- [27] H. Amandusson, L.G. Ekedahl, H. Darnetun, Effect of CO and O₂ on hydrogen permeation through a palladium membrane, *Appl. Surf. Sci.* 153 (2000) 259–267. doi:10.1016/S0169-4332(99)00357-8.
- [28] T.E. Broadhurst, H.A. Becker, Onset of fluidization and slugging in beds of uniform particles, *AIChE J.* (1975). doi:10.1002/aic.690210204.
- [29] C.Y. Shiau, C.J. Lin, An improved bubble assemblage model for fluidized-bed catalytic reactors, *Chem. Eng. Sci.* (1993). doi:10.1016/0009-2509(93)81010-S.
- [30] R.C. Reid, J.M. Prausnitz, T.K. Sherwood, *The properties of gases and liquids*, 4th ed, McGraw-Hill (1977). (1987). doi:10.1002/aic.690240634.
- [31] E.N. Fuller, P.D. Schettler, J.C. Giddings, A new method for prediction of binary gas-phase diffusion coefficients, *Ind. Eng. Chem.* 58 (1966) 18–27. doi:10.1021/ie50677a007.
- [32] D.E. Mears, Tests for Transport Limitations in Experimental Catalytic Reactors, *Ind. Eng. Chem. Process Des. Dev.* 10 (1971) 541–547. doi:10.1021/i260040a020.
- [33] P.B. Weisz, C.D. Prater, Interpretation of Measurements in Experimental Catalysis, *Adv. Catal.* (1954). doi:10.1016/S0360-0564(08)60390-9.
- [34] D.E. Mears, Diagnostic criteria for heat transport limitations in fixed bed reactors, *J. Catal.* 20 (1971) 127–131. doi:10.1016/0021-9517(71)90073-X.
- [35] J. Wei, E. Iglesia, Structural requirements and reaction pathways in methane activation and chemical conversion catalyzed by rhodium, 225 (2004) 116–127. doi:10.1016/j.jcat.2003.09.030.



Chapter

Five

Effects of scale-up on membrane reactor performance

Fluidized bed membrane reactors have shown great potential and are now being scaled up to larger scale. However, understanding of the system behaviour at larger scales still needs to be improved. This chapter investigates the effects of scaling the single membrane fluidized bed reactor investigated in chapter 4 to a system containing 5 or 7 membranes. Experiments to characterize the system and with and without prevailing reactions are performed at different temperatures (400-550 °C) and feed flow rates. The results are compared with predictions from a 1D-phenomenological model. The results show a decrease in performance as a result of mass transfer limitations due to induced differences in fluidization behaviour in larger systems. Investigation into different membrane configurations confirm the interaction of concentration polarization layers and the importance of proper tuning of the distance between the membranes.

5.1. Introduction

The experimental demonstrations of intensified and integrated systems for methane reforming reactions differ in scale, from milliliter scale in the lab up to 40 Nm³H₂/h [1]. In the work of Kyriakides et al. the performance of a membrane reactor with commercial Ni catalyst pellets has been compared to a system with a Ni catalyst on a ceramic foam [2]. They show that the ceramic foam significantly reduces the radial temperature difference between the reactor wall and the membrane. In the work of Boeltken et al. a micro-structured membrane reactor has been presented. In this system, a very high catalyst-to-membrane surface ratio is obtained, combined with high heat and mass transfer properties of a micro-reactor system [3]. The fluidized bed membrane reactor concept has been demonstrated for different applications [4][5][6][7]. Moreover, in the previous chapter it is demonstrated that the fluidized bed membrane reactor can reduce concentration polarization (CP), thus increased mass transfer while operating at virtual isothermal conditions (i.e. excellent heat transfer). The demonstrations of these concepts show significant improvements of the membrane performance by reactor design, however, the scale remains generally small, around 10-100 cm² of membrane area [8][3]. The larger systems from 0.5-10 m² reported in literature often focus on the demonstration of the concept and stability [9][10]. The effects on membrane performance of scaling up these systems is therefore relatively little explored. With the increase in selectivity and hydrogen fluxes of the membranes, the operating conditions are critical parameters in optimizing the reactor design. In these cases, the mass transport or reaction rates can become limiting in comparison to the membrane permeation rate. The behavior of the concentration polarization effects can thus play a significant role in determining the required membrane area and reactor design.

Several works have studied the mass transport in membrane reactors in detail. In the work by Murmura et al. the emergence of a reaction boundary layer (RBL) that develops along the membrane wall has been observed [11]. In this case the reaction rate becomes limiting and a region near the membrane is identified where the system is not at equilibrium. By adapting the membrane-to-wall distance to the RBL the system could be optimized. In the work by Voncken et al. the

separation of hydrogen from a hydrogen/nitrogen mixture in a fluidized bed membrane system has been studied using two-fluid model [12]. Different configurations of membrane placements are described and the effect on CP and fluidized bed hydrodynamics is discussed. An interaction of two concentration polarization layers is found to further reduce the membrane performance.

The work in this chapter aims at further investigating the effects that scaling up of fluidized bed membrane reactor has on the performance of the system and what the implications for a future reactor design are. Experiments have been performed on two different fluidized bed membrane reactor systems. The phenomenological model developed in chapter 4 is used to investigate a scaled up system with 5 membranes under steam reforming conditions [13]. The investigation and analysis are then extended to a 7-membrane system, where different configurations are studied.

5.2. Experimental

5.2.1. Setup

The experimental system used in this study can be divided into three sections: the feeding system, reactor system and gas analysis system. A schematic representation of the experimental setup is given in Figure 5.1. From the feeding system the following gasses could be fed to the system: H_2 , He, N_2 , Air, CO_2 , CH_4 and CO. The feed flow rate of these gasses was controlled with Bronkhorst mass flow controllers. A steam feed was provided from a Stepdos O3RC pump and fed through an evaporation system to produce and mix the steam with the reactor feed. The reactor feed could be fed to the reactor section or by-passed directly to the analysis section. The feed to and from the reactor section was traced and kept at 140 °C when steam was fed to the system. After the reactor section two streams are treated, the permeate and the retentate, A cyclone was applied to remove fine particles escaped from the retentate and a 7 μm filter was applied to avoid finer particles from escaping the system. This stream was then led through a condenser to remove the steam and was fed to a SICK analyser to obtain the gas composition. The permeate side could be brought to a pressure of 0.1 bar with the use of a vacuum pump. The flow rate of the permeate side was measured

using a Horibastec flowmeter. Both permeate and retentate streams were sent to the vent of the system.

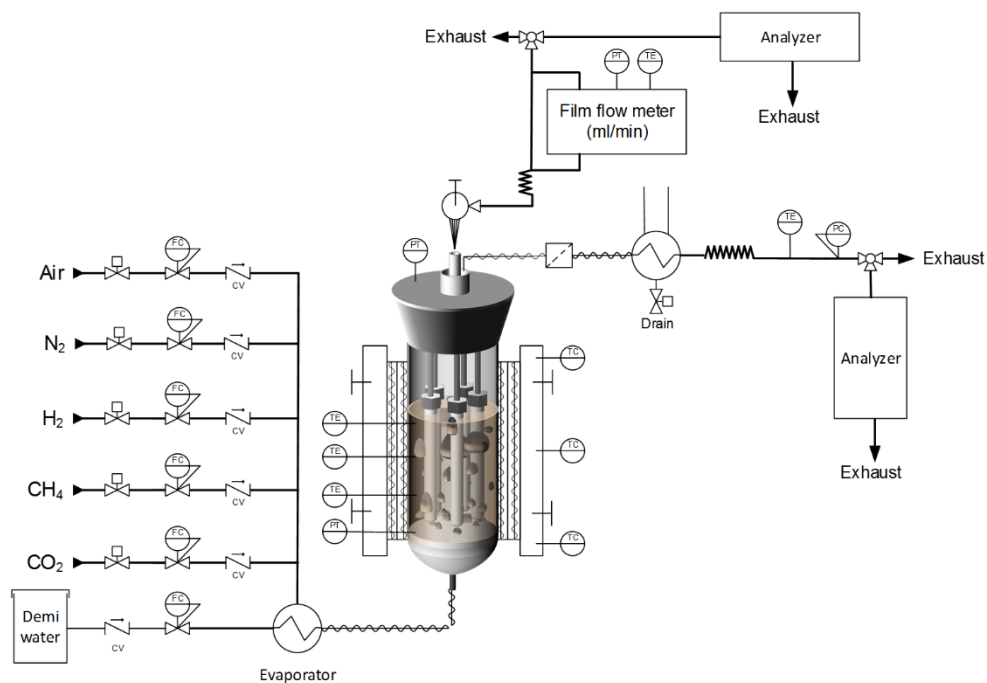


Figure 5.1. Schematic representation of the experimental setup.


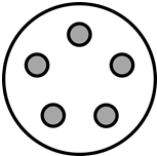

In this study two reactors have been used in the testing setup: one with 5 membranes (referred to as 5-MR) and one with 7 membranes (referred to as 7-MR). In the 5-MR system it was not possible to obtain results at a $U/U_{mf} > 4$ due to setup limitations. If there are no kinetic limitations, which is the case here, the system performance depends on the methane load-to-surface ratio (LTSR) [14]. The load-to-surface ratio in relation to the hydrogen recovery or methane conversion can be used as a key design parameter. From the desired capacity and system performance the required membrane area and feed flow rate follows. When the membrane geometry is fixed, the distance also referred to as the pitch between the membranes will result in the free area and hence the velocity obtained in the system. In the case of the 7 membrane system the pitch between the membranes was reduced therefore the desired LTSR could be obtained at higher velocities. The details of both reactors are presented in Table 5.1. The

system presented in the previous chapter is added for comparison and was used to validate the model [13]. The membranes were fingerlike tubular Al_2O_3 supported thin film PdAg membranes and sealed using a swagelok connection with a graphite ferrule. In these systems the membranes were connected with a dense metal tube from the top flange and vertically immersed into the fluidized bed. In Table 5.1 the placement of the membranes is also specified for each configuration. In the 5-MR system a pentagonal configuration of the membranes was used, here the thermocouple and pressure capillary were bundled in the middle. For the 7-MR system a hexagonal configuration with a center membrane was used. In this case, the thermocouples were placed in the space between the membrane and reactor wall. To reduce the system volume of the 7-MR the membranes were placed as close together as possible in a staggered arrangement. A picture of both reactor configurations is shown in Figure 5.2. Both systems have the ability to measure each membrane separately, for purpose of characterization of the permeation properties and evaluation of the stability. Prior to the reaction experiments, the membranes were characterized without the fluidized bed present. The catalyst, a Rh/ Al_2O_3 catalyst was provided by Johnson Matthey, had an average particle size of 250 μm and was mixed with Al_2O_3 support with the same particle size and distribution. The reforming experiments were performed in a temperature range between 420 °C and 550 °C and up to a pressure of 6 bar(a). The system was evaluated using the following performance parameters: methane conversion and hydrogen recovery factor; which are defined in Eq. 5.1 and Eq. 5.2, respectively.

$$\text{Methane conversion} = \frac{(F_{\text{CH}_4,\text{in}} - F_{\text{CH}_4,\text{out}})}{F_{\text{CH}_4,\text{in}}} \quad \text{Eq. 5.1}$$

$$\text{Hydrogen Recovery Factor} = \frac{F_{\text{H}_2,\text{perm.}}}{4F_{\text{CH}_4,\text{in}}} \quad \text{Eq. 5.2}$$

Table 5.1. Reactor details.

	Single membrane reactor [13]	5-MR	7-MR
Internal Reactor Diameter (mm)	42.7	100	80
Catalyst Rh/Al ₂ O ₃ (kg)	0.13	1.29	0.92
Catalyst in support (Al ₂ O ₃) mixture	87.5% (w/w)	44% (w/w)	44% (w/w)
Membrane(s)	1 PdAg on Al ₂ O ₃ 14/7 mm (OD/ID*)	5 PdAg on Al ₂ O ₃ 14/7 mm (OD/ID*) fingerlike	7 PdAg on Al ₂ O ₃ 14/7 mm (OD/ID*) fingerlike
Membrane Area (cm ²)	64.2	929.9	1281.8
Membrane Configuration			

*(OD/ID) outer diameter and inner diameter

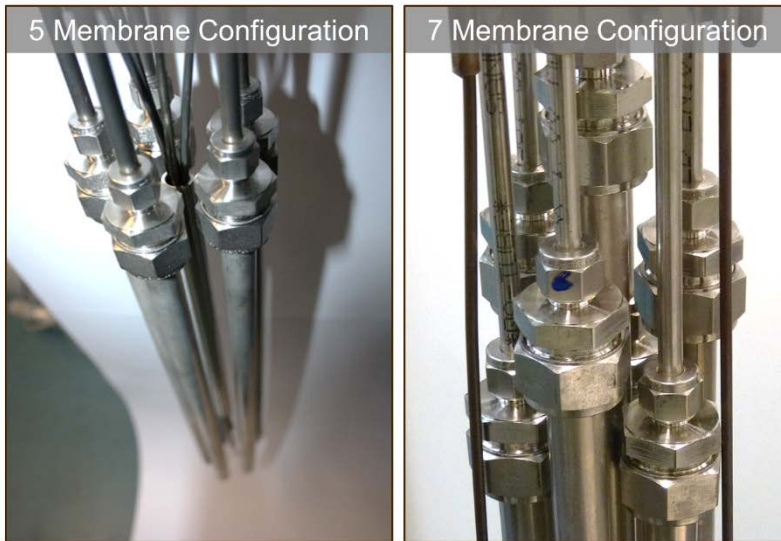


Figure 5.2. Pictures of the 5 and 7 membrane configuration.

5.2.2. Membranes

In this study a total of 7 membranes were used. The membranes were produced using an electroless plating technique described in Chapter 2. The 5 membranes used in 5-MR were resealed and reused in the 7-MR (thus losing a few mm in length when reused). All the membranes and their corresponding lengths are shown in Table 5.2.

Table 5.2. List of membranes and corresponding lengths used in the systems.

Membrane	5 MR (cm ²)	7 MR (cm ²)
M1	186	180
M2	185	179
M3	187	179
M4	186	178
M5	186	177
M6		194
M7		194

5.2.3. Phenomenological model

The phenomenological one-dimensional two-phase fluidized bed membrane reactor model described in Chapter 4, which accounts for concentration polarization through a stagnant film, was used for the analysis. In the model approach, both the bubble and emulsion phases of the fluidized bed are divided into a number of CSTRs along the reactor height [14]. The model validation was performed with experimental results obtained with the single membrane reactor (Table 5.1). The film layer thickness δ was estimated from the experimental results using Eq. 5.3. Here, D_i is the molecular diffusion coefficient for an empty tube system or the dispersion coefficient for a fluidized bed, which was estimated from CFD simulations at $1 \cdot 10^{-4} \text{ m}^2\text{s}^{-1}$ [15], $R_{memb.}$ is the radius of the membrane, $x_{i,memb.}$ and $x_{i,bulk}$ are the concentration on the membrane surface and in the bulk respectively and C_{tot} is the total concentration. In Chapter 4, a film layer thickness of 0.54 cm was found, with which the reforming experiments in the single membrane system could be well described. In the presented work Eq. 5.3 is rewritten to Eq. 5.4, which allows to distinguish between the finite flux correction factor ξ_m (Eq. 5.5), the geometric factor f (Eq. 5.6) and the mass transfer coefficient k_m (Eq. 5.7). k_m and f are used in the evaluation of the experimental results.

$$N_{i,r_m} = -\frac{D_i C_{tot}}{R_{memb.} \ln\left(1 + \frac{\delta}{R_{memb.}}\right)} \ln\left(\frac{1 - x_{i,memb.}}{1 - x_{i,bulk}}\right) \quad \text{Eq. 5.3}$$

$$N_{i,r_m} = -k_m f \xi_m C_{tot} (x_{i,bulk} - x_{i,memb.}) \quad \text{Eq. 5.4}$$

$$\xi_m = \frac{\ln\left(\frac{1 - x_{i,memb.}}{1 - x_{i,bulk}}\right)}{(x_{i,bulk} - x_{i,memb.})} \quad \text{Eq. 5.5}$$

$$f = \frac{\frac{\delta}{R_{memb.}}}{\ln\left(1 + \frac{\delta}{R_{memb.}}\right)} \quad \text{Eq. 5.6}$$

$$k_m = \frac{D_i}{\delta} \quad \text{Eq. 5.7}$$

5.3. Results

5.3.1. Membrane characterization

In order to analyze the results and model the performance of the system, the performance of each of the membranes in the system was determined first. After integration of the membranes the reactor system was heated up to 400 °C without catalyst present in the reactor. The membranes were exposed to an air treatment of two minutes at this temperature. Subsequently, the system was heated to 500 °C and left under pure hydrogen for 24 hours until a stable hydrogen permeation was reached. The temperature was then decreased with steps of 25 °C to 400 °C, and permeation tests were performed at each interval. The measured hydrogen permeation fluxes through these membranes can be well described with a difference in the square root of the partial pressure at the retentate and permeate side of the membrane, indicating that the bulk diffusion of hydrogen in the PdAg layer is rate limiting (Sieverts' law) [16]. The permeation results obtained were used to determine the pre-exponential factor and activation energy for each membrane, and these results are reported in Table 5.3. Although the membranes are prepared in the same way, still a significant variation in the performance was observed, which is most likely a result of inhomogeneities during the manufacture of the membranes. Note that 5 of the 7 membranes used in the 7-MR were used previously in the 5-MR system. The use and resealing, and subsequent treatment and heating resulted in a slight decrease in the membrane performance. The obtained flux permeation values are in the same range as reported previously in literature [17]. In previous work the membrane pre-exponential factor was found to be $8.74 \cdot 10^{-3} \text{ mol}^1 \text{s}^{-1} \text{m}^{-2} \text{Pa}^{-0.5}$ and the activation energy 9.26 kJ/mol [13]. The

average values of the pre-exponential factors and activation energies are also reported. In order to evaluate whether these average values give a good representation of the full system, predictions with the averaged values have been compared with the cumulative flow rate predicted by accounting for the fluxes through each membrane separately, see Figure 5.3. A difference of less than 1% was obtained for the total membrane permeation flux when using the average values or the individual membrane fluxes. In case the parameters obtained from the worst or best performing membrane were used, a difference of up to 15% could be obtained. This shows, that when scaling up a membrane system to for example a system containing more than 100 membranes, a representative sample should be used to estimate the average performance of the entire set of membranes. Moreover, it shows that further improvements in the production process are required to reduce the differences in membrane performance.

Table 5.3. Membrane characteristics

Membrane	5 Membrane Reactor			7 Membrane Reactor		
	P_0 $10^{-3} \text{ mol}^1\text{s}^{-1}\text{m}^{-2}\text{Pa}^{-0.5}$	E_a (kJ/mol)	r^2	P_0 $10^{-3} \text{ mol}^1\text{s}^{-1}\text{m}^{-2}\text{Pa}^{-0.5}$	E_a (kJ/mol)	r^2
M1	6.58	7.0	0.995	7.85	7.5	0.997
M2	7.83	9.2	0.999	8.74	9.9	0.980
M3	6.78	7.3	0.997	8.52	8.5	0.976
M4	6.58	8.8	0.996	7.19	8.7	0.998
M5	6.97	9.1	0.997	7.94	9.3	0.999
M6				7.53	8.1	0.996
M7				7.32	7.3	0.997

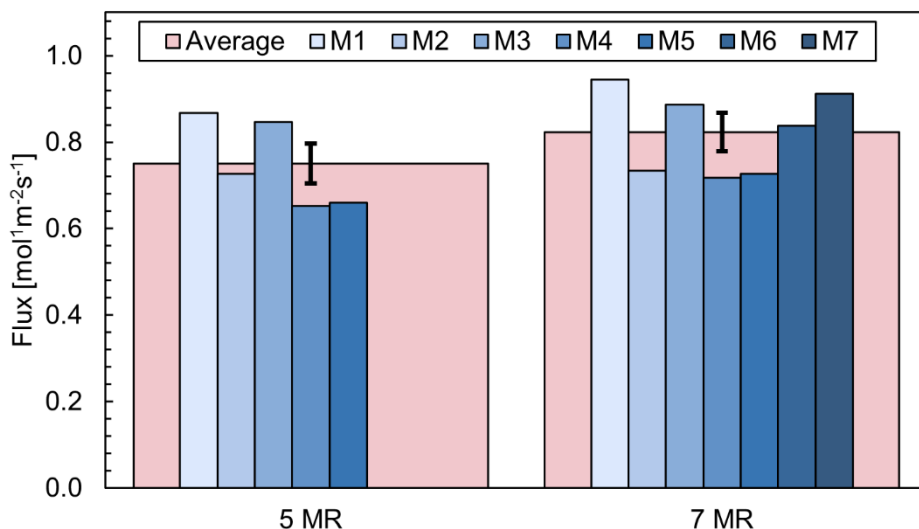


Figure 5.3. Hydrogen flux under pure hydrogen at 500 °C and a transmembrane pressure difference of 4 bar.

5.3.2. 5 membrane reactor

The 5-MR was evaluated at different operating pressures for steam reforming of methane, and the results are shown in Figure 5.4. The methane equilibrium conversion decreases with an increase in the pressure. The experimental results show a slight initial decrease with pressure as a result of the stoichiometry of the SMR reaction. The decrease is however much lower than the decrease in the equilibrium conversion because of the selective extraction of hydrogen. Contrary to the thermodynamic equilibrium conversion, when the pressure is increased above 4 bar an increase in the conversion was measured as a result of the hydrogen extraction. At this point the effect of the increase in the hydrogen extraction due to the increase in pressure, is stronger than the decrease in equilibrium conversion.

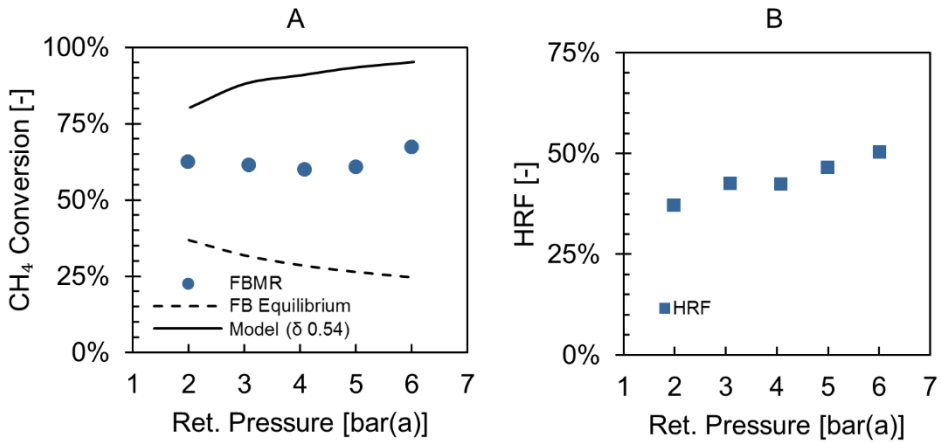


Figure 5.4. A) Methane conversion, B) Hydrogen recovery factor, for steam reforming of methane in the 5-MR at 485 °C and a SCR of 3 for different total pressures.

The reactor performance was modelled at the same conditions as used in the experiments and is included in Figure 5.4, where in the 1D model a film layer thickness of 0.54 cm was used, which was obtained from single membrane experiments. This significantly over predicts the experimental results, as shown in Figure 5.4. The hydrogen flux that is obtained from the model is much larger than obtained from the experiments, explaining the difference in conversion, indicating that the model validated with results from the single membrane experiments does not agree when the system is scaled up. As a result of the scale up, the hydrogen recovery factor, which was at highest around 35% in the single membrane system, increases to about 50% with the 5 membrane system. The other main difference was the fluidization regime in which the system was operated. The relative superficial velocity (based on the feed) used in the single membrane system U/U_{mf} was 7.41 [13]. However, in the 5-membrane system the U/U_{mf} was between 1 to 4, depending on the experimental conditions. The lower hydrogen flux observed can be either caused by bubble-to-emulsion phase mass transfer or by concentration polarization. From the model results it becomes clear that bubble-to-emulsion phase mass transfer is not limiting. It is therefore very likely that the lower hydrogen flux is a result of concentration polarization. As mentioned before the 5-membrane system has a much lower U/U_{mf} . Therefore, fluidization is much less vigorous. The decrease in the U/U_{mf} ratio could

significantly affect the emulsion phase to membrane mass transfer rate. This would mean that the assumption of a film layer thickness of 0.54 cm and a radial dispersion coefficient of $1 \cdot 10^{-4}$ m²/s in the fluidized bed was no longer valid for this situation. To evaluate these effects, the mass transfer term was adjusted to match the model prediction with the experimental results. Both the mass transfer coefficient and the geometric factor were adjusted. However, it was not possible to discriminate between the effect of the radial dispersion coefficient or the film layer thickness, and the results are therefore presented in terms of k_{mf} . The mass transfer coefficient k_{mf} obtained from the adjustments are presented in Figure 5.5. A significantly lower mass transfer rate can be observed for lower U/U_{mf} . Considering the results of the 5-MR and the single membrane reactor a linear relationship between k_{mf} and the fluidization velocity is found. This indicates that the observed relationship can explain the discrepancy between the model and experimental results. This means that the decrease to half of the U/U_{mf} in the 5-membrane system, compared to the single membrane system, resulted in a decrease of the lateral dispersion coefficient by a factor 1.46. Or that the mass boundary layer thickness was increased by a factor 1.58.

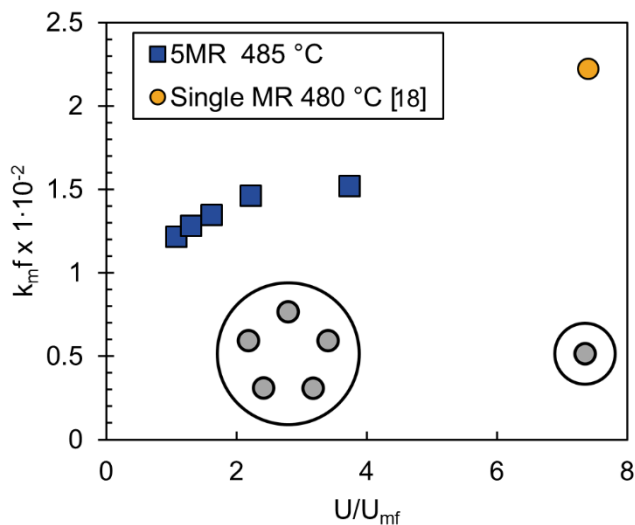


Figure 5.5. Mass transfer coefficient k_{mf} at different U/U_{mf} for the 5MR and single membrane system. [13][18]

5.3.3. 7-Membrane system

In the 7-MR system the pitch between the membranes is reduced while the membrane area is increased. This results in similar load-to-surface ratios at higher U/U_{mf} . The 7-MR also had the possibility to measure two of the seven membranes in the bundle separately. In this way the performance of a single membrane in the bundle could be obtained. Moreover, each of the membranes could be closed individually, in this way the performance of different membrane configurations could be studied. The results of the 7-MR are shown in Figure 5.6. As mentioned before, the HRF decreases with increasing LTSR. With the increase in temperature, the HRF increases, due to an increase in equilibrium conversion and an increase in permeability of the membranes. The influence of the temperature on the obtained HRF decreased at higher temperatures. This was because the pressure on the permeate side could not be kept constant and increased, as the vacuum pump capacity was insufficient to keep a low permeate pressure. Therefore, at higher fluxes the permeate pressure increased resulting in a lower driving force over the membrane at higher temperatures.

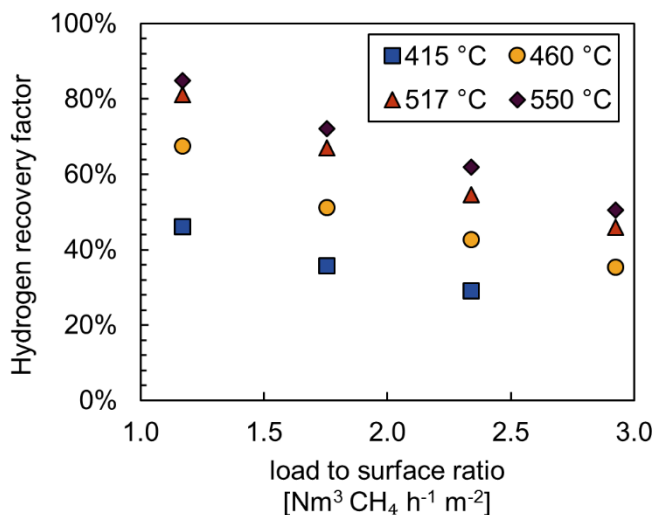


Figure 5.6. HRF vs LTSR of the 7-membrane system at different temperatures, SCR 3, pressure of 5 bar(a) on the retentate and vacuum conditions ranging for 0.22 to 0.56 at the permeate.

To understand the degree of concentration polarization in this system the mass transfer coefficient k_{mf} was estimated with the model, for each of the experiments presented in Figure 5.6. The results show a similar trend as the results obtained from the 5-membrane system. With the increase in U/U_{mf} , as a result of the increased LTSR, the mass transfer is increased. Another observation that can be made from these results is that at higher temperatures the mass transfer rate is on average decreased. At higher temperatures the average driving force in the system is increased due to the increase in the permeability of the membranes, which leads to an increase in flux. As shown by Helmi et al., the porosity of the emulsion phase can be reduced near the membrane resulting in the formation of densified zones, which can result in an additional mass transfer resistance for gas components [18], i.e. an increase in the film layer thickness or a decrease in the effective radial dispersion coefficient. These effects become more pronounced when the flux is increased. Vonken et al. also showed this effect for 250 μm particles. As with temperature the flux is increased the formation of densified zones could be a reason explanation for the observed reduced mass transfer rate at higher temperatures.

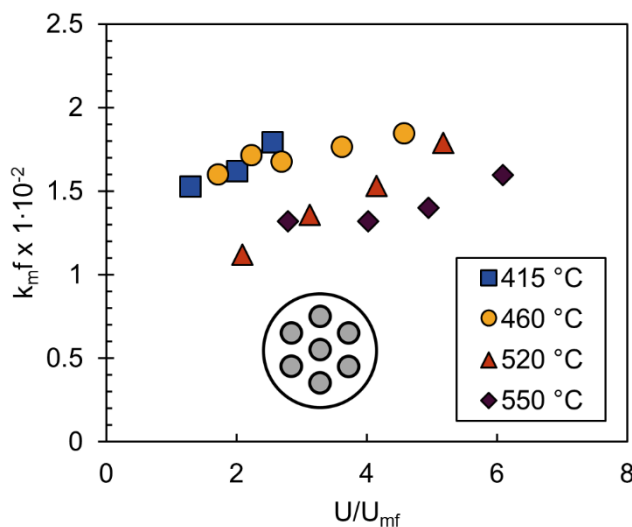


Figure 5.7 Mass transfer coefficient k_{mf} at different U/U_{mf} for the 7MR system.

In the work by Voncken et al. also the effect of the membrane configuration is discussed for separation from a hydrogen mixture. The work shows that, depending on the configuration, the membranes can compete for hydrogen reducing the membrane productivity. In the case the membranes are placed too close together the mass transfer boundary layers start to interact, in which case the area from which hydrogen is transported from the bulk towards the CP layer is significantly reduced. A reduction in this area results in an even lower mass transport rate. In the 7-membrane system the membranes are placed at a distance of only 1 cm from each other.

The 7-MR system allowed measuring the performance of an individual membrane while the bundle of membranes was active and also allowed operation in different configurations by closing some of the membranes. First, the performance in the bundle of the center membrane (membrane 0) was compared to the performance of one of the outer membranes (Membrane 6). The results are shown in Figure 5.8 as a percentage of their theoretical contribution according to the measured membrane permeability. The results show that in the cases of 5.3 and 3.2 times U_{mf} the performance of the membranes comes close to their theoretical contribution. No significant difference in performance is observed between both membranes, indicating that the inner membrane is not performing significantly less than the other membranes. However, when operating close to U_{mf} , the membrane performance shows a large deviation from the theoretical contribution for both membranes, and in this case de-fluidization could have resulted in preferential flow and played a significant role.

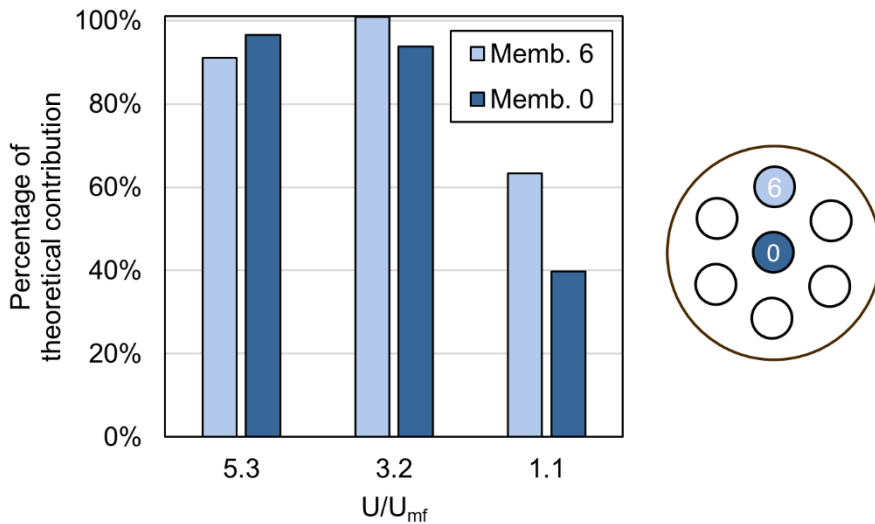


Figure 5.8. Comparison of membrane performance in the bundle at 500 °C and 5 bar.

To further investigate the interaction effects of the mass transfer boundary layers, the performance was compared with different membrane configurations. The first configurations that were investigated were: all membranes are active, membrane 6 was closed and membrane 0 closed. The obtained system performance in terms of HRF and estimated averaged mass transfer boundary layer thickness are shown for the different configurations in Figure 5.9. The results show that the "deactivation/closing" of a single membrane hardly affects the system performance, the hydrogen recovery at 2.2 U/U_{mf} only changes from 51.3 to 49.2 and 50.5, while the surface area was reduced by 14%. As can be seen from the calculated averaged mass transfer coefficients k_{mf} from the obtained experimental data that the emulsion phase to membrane wall mass transfer rate is increased when one membrane was closed. Closing the middle membrane seems to have an even stronger effect on the film layer thickness as this membrane is expected to have more 'interaction' with the other membranes than the membranes placed at the outer ring. Thus, the decrease in available membrane area is compensated by a decrease in the concentration polarization, explaining that the hydrogen recovery factor was hardly affected. The same effect was obtained at the higher velocity of U/U_{mf} 3.8. The decrease in the HRF at higher relative fluidization velocity is a result of an increase in the the load-to-surface ratio.

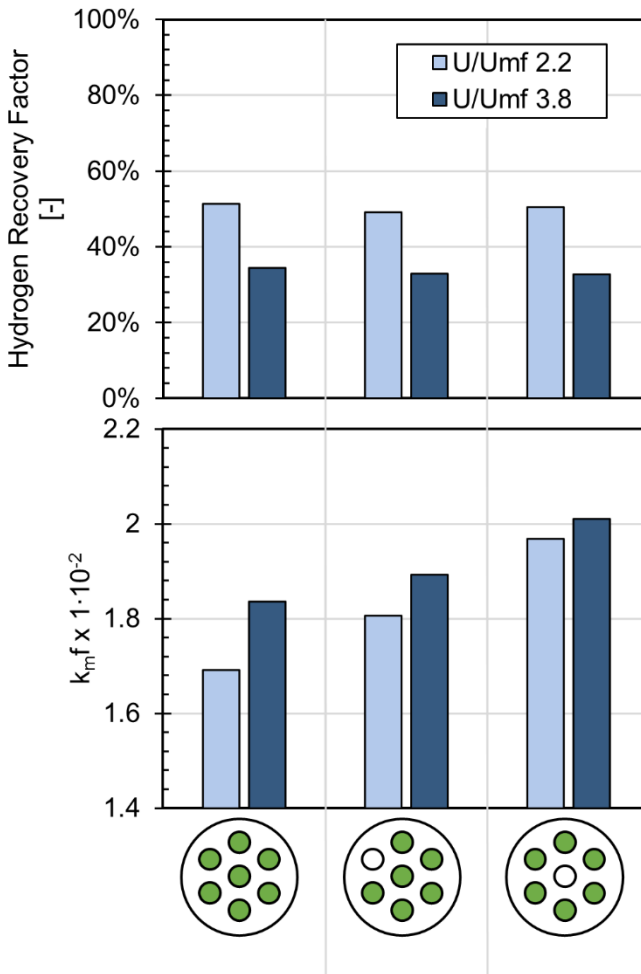


Figure 5.9. Hydrogen recovery and mass transfer coefficient k_{mf} for the full system and full system without membrane 6 and 0 at different U/U_{mf} .

Subsequently, the performance of another three configurations was compared, where in these cases only three membranes were active (and four membranes closed). The results and corresponding configurations are shown in Figure 5.10. In these cases, the system performance is clearly affected by the configuration of the membranes. Placing the membranes close to each other results in a significant decrease in the average mass transfer coefficient k_{mf} . The more the mass transfer boundary film layers interact or overlap, the higher the degree of CP. It should be noted that in this case an additional effect of gas by-pass could play a role. The results clearly indicate an effect of 'interaction' between the membranes CP layers,

also at higher relative fluidization velocities. In the simulation study by Voncken et al. a minimum distance of 2 cm between the membranes was advised for membranes with a very similar diameter and permeability. The presented results thus agree with this and indicate that contact between the CP layers should be avoided. However, too much free space between the membranes could result in gas by-pass. Furthermore, the free space and load-to-surface area need to be tuned to achieve the desired superficial velocity and obtain the desired fluidization behaviour. To fully optimize these parameters in a reactor design, also the particle size and membrane size and length need to be carefully tuned.

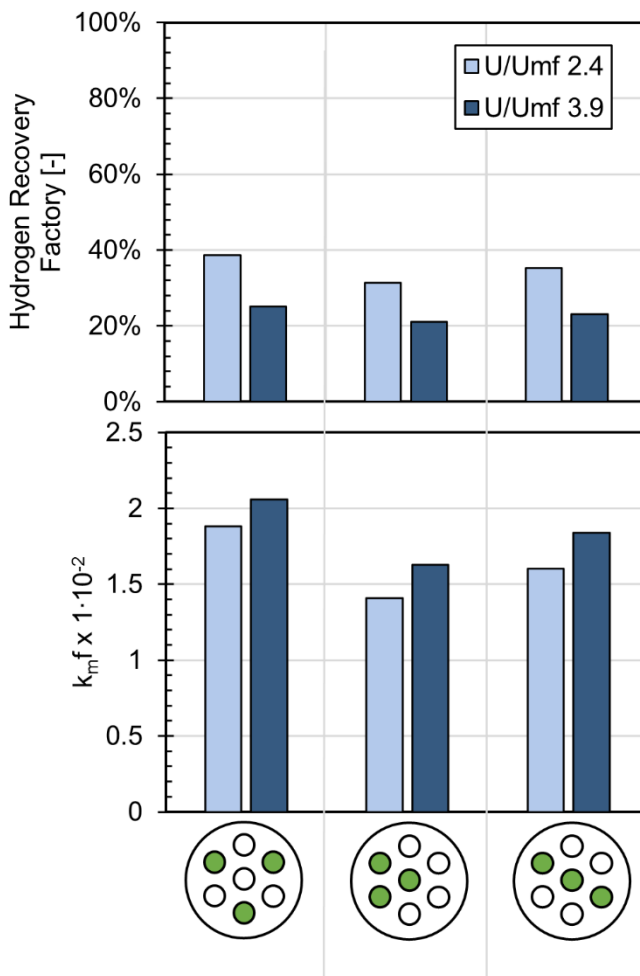


Figure 5.10. Hydrogen recovery and mass transfer coefficient k_{mf} for different configurations and U/U_{mf} .

5.4. Conclusions

In the presented work two fluidized bed membrane reactors and different membrane configurations have been experimentally evaluated, and a 1D two-phase phenomenological model that accounts for concentration polarization was used to analyze the results and understand the behavior of the systems.

First, each of the membranes was separately characterized, and the results showed a variation in membrane permeability up to 15%, which needs to be taken into consideration when scaling up or evaluating a system with multiple membranes. This deviation can most likely be reduced, when the membrane production process becomes more standardized and is also scaled up.

Comparison of the performance of a system with 5 membranes and with 7 membranes with predictions from the phenomenological reactor model, that was validated with a single membrane reactor, showed that the extent of concentration polarization depends on the fluidization behavior. An increase in the relative fluidization velocity U/U_{mf} resulted in an increase of the average emulsion phase to membrane surface mass transfer coefficient (and thus reduced CP).

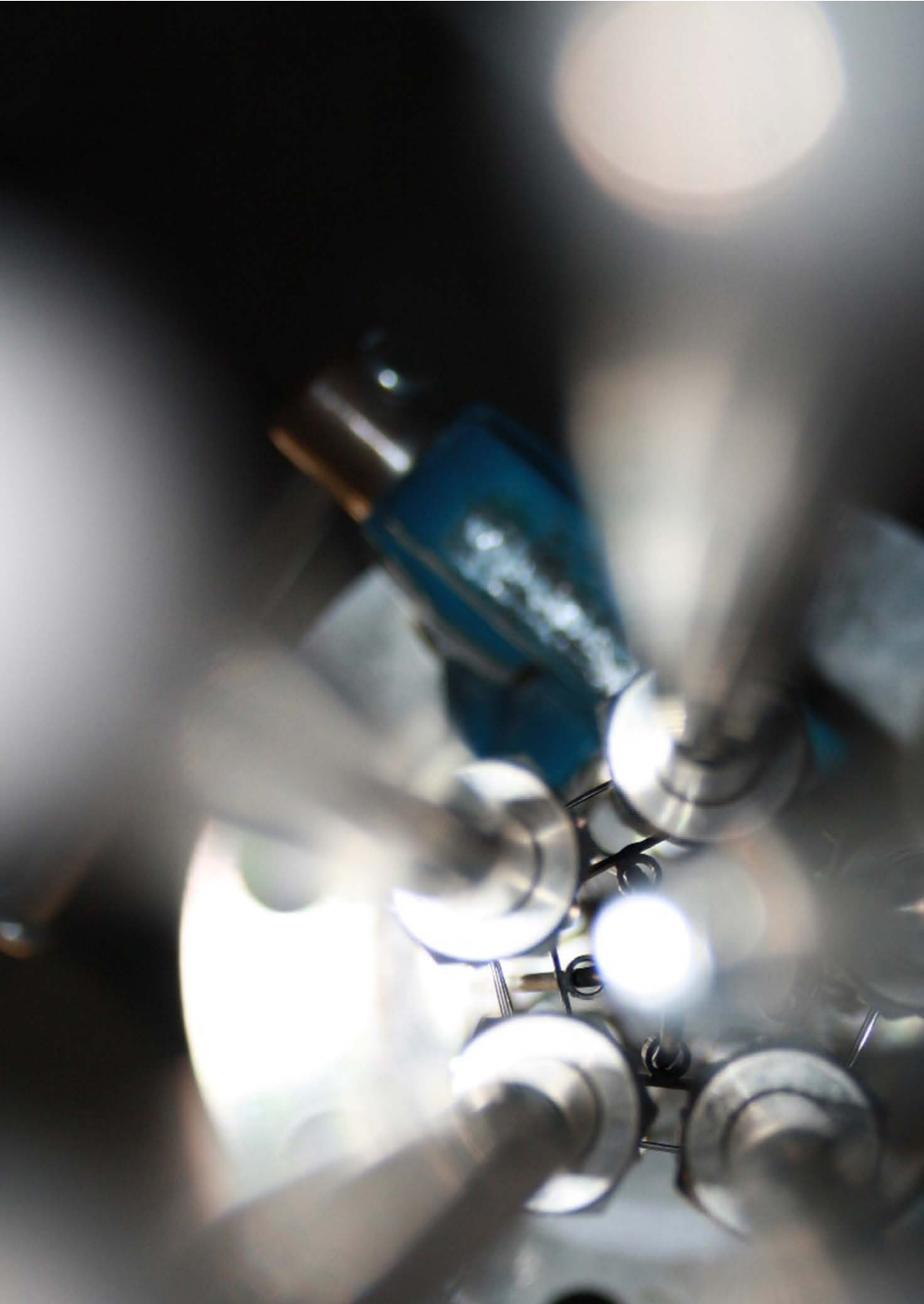
The average emulsion phase to membrane surface mass transfer could also be increased when overlap of the mass transfer layer was reduced. In this way a reduction of 14% of the membrane area led to almost no difference in hydrogen recovery. Evaluation of the performance of the system with different membrane configurations showed a clear increase in the extent of CP (up to about 25% decrease in the overall mass transfer rate), when the membranes were placed relatively close together, which was attributed to the interaction or overlap of the mass transfer boundary layers of neighboring membranes. A minimum distance between the membranes to avoid interacting boundary layers is thus advised. However, for the optimal design of fluidized bed membrane reactors, also the free space between the membranes should be kept to a minimum to maximize productivity and avoid gas by-pass.

References

- [1] B.N. Lukyanov, D. V. Andreev, V.N. Parmon, Catalytic reactors with hydrogen membrane separation, *Chem. Eng. J.* 154 (2009) 258–266. doi:10.1016/j.cej.2009.04.023.
- [2] A.S. Kyriakides, L. Rodríguez-García, S. Voutetakis, D. Ipsakis, P. Seferlis, S. Papadopoulou, Enhancement of pure hydrogen production through the use of a membrane reactor, *Int. J. Hydrogen Energy.* 39 (2014) 4749–4760. doi:10.1016/j.ijhydene.2014.01.093.
- [3] T. Boeltken, A. Wunsch, T. Gietzelt, P. Pfeifer, R. Dittmeyer, Ultra-compact microstructured methane steam reformer with integrated Palladium membrane for on-site production of pure hydrogen: Experimental demonstration, *Int. J. Hydrogen Energy.* 39 (2014) 18058–18068. doi:10.1016/j.ijhydene.2014.06.091.
- [4] S.A. Wassie, J.A. Medrano, A. Zaabout, S. Cloete, J. Melendez, D.A.P. Tanaka, et al., Hydrogen production with integrated CO₂ capture in a membrane assisted gas switching reforming reactor: Proof-of-Concept, *Int. J. Hydrogen Energy.* 43 (2018) 6177–6190. doi:10.1016/j.ijhydene.2018.02.040.
- [5] J.A. Medrano, I. Potdar, J. Melendez, V. Spallina, D.A. Pacheco-Tanaka, M. van Sint Annaland, et al., The membrane-assisted chemical looping reforming concept for efficient H₂ production with inherent CO₂ capture: Experimental demonstration and model validation, *Appl. Energy.* 215 (2018) 75–86. doi:10.1016/j.apenergy.2018.01.087.
- [6] J.A. Medrano, E. Fernandez, J. Melendez, M. Parco, D.A.P. Tanaka, M. Van Sint Annaland, et al., Pd-based metallic supported membranes: High-temperature stability and fluidized bed reactor testing, *Int. J. Hydrogen Energy.* 41 (2016) 8706–8718. doi:10.1016/j.ijhydene.2015.10.094.
- [7] E. Fernandez, A. Helmi, J.A. Medrano, K. Coenen, A. Arratibel, J. Melendez, et al., Palladium based membranes and membrane reactors for hydrogen production and purification: An overview of research activities at Tecnalia

- and TU/e, *Int. J. Hydrogen Energy*. 42 (2017) 13763–13776. doi:10.1016/j.ijhydene.2017.03.067.
- [8] A. Arratibel Plazaola, D.A. Pacheco Tanaka, M. Van Sint Annaland, F. Gallucci, *Recent Advances in Pd-Based Membranes for Membrane Reactors*, *Molecules*. 22 (2017) 1–53. doi:10.3390/molecules22010051.
- [9] Y. Shirasaki, T. Tsuneki, Y. Ota, I. Yasuda, S. Tachibana, H. Nakajima, et al., *Development of membrane reformer system for highly efficient hydrogen production from natural gas*, *Int. J. Hydrogen Energy*. 34 (2009) 4482–4487. doi:10.1016/j.ijhydene.2008.08.056.
- [10] F. Gallucci, E. Fernandez, P. Corengia, M. van Sint Annaland, *Recent advances on membranes and membrane reactors for hydrogen production*, *Chem. Eng. Sci.* 92 (2013) 40–66. doi:10.1016/j.ces.2013.01.008.
- [11] M.A. Murmura, S. Cerbelli, M.C. Annesini, *Designing the optimal geometry of a membrane reactor for hydrogen production from a pre-reformed gas mixture based on the extent of the reaction boundary layer*, *Chem. Eng. Process. Process Intensif.* 120 (2017) 148–160. doi:10.1016/j.ces.2017.07.011.
- [12] R.J.W. Voncken, I. Roghair, M. van Sint Annaland, *A numerical study on concentration polarization in 3D cylindrical fluidized beds with vertically immersed membranes*, *Chem. Eng. Sci.* 205 (2019) 299–318. doi:10.1016/j.ces.2019.05.010.
- [13] N. de Nooijer, F. Gallucci, E. Pellizzari, J. Melendez, D.A. Pacheco Tanaka, G. Manzolini, et al., *On concentration polarisation in a fluidized bed membrane reactor for biogas steam reforming: Modelling and experimental validation*, *Chem. Eng. J.* 348 (2018) 232–243. doi:10.1016/j.ces.2018.04.205.
- [14] F. Gallucci, M. Van Sint Annaland, J.A.M. Kuipers, *Autothermal reforming of methane with integrated CO₂ capture in a novel fluidized bed membrane reactor. Part 2 comparison of reactor configurations*, *Top. Catal.* 51 (2008) 146–157. doi:10.1007/s11244-008-9127-7.

- [15] A. Helmi, R.J.W. Voncken, A.J. Raijmakers, I. Roghair, F. Gallucci, M.V.S. Annaland, On concentration polarization in fluidized bed membrane reactors, *Chem. Eng. J.* 332 (2018) 464–478. doi:10.1016/j.cej.2017.09.045.
- [16] T.L. Ward, T. Dao, Model of hydrogen permeation behavior in palladium membranes, *J. Memb. Sci.* 153 (1999) 211–231. doi:10.1016/S0376-7388(98)00256-7.
- [17] E. Fernandez, A. Helmi, K. Coenen, J. Melendez, J.L. Viviente, D.A. Pacheco Tanaka, et al., Development of thin Pd-Ag supported membranes for fluidized bed membrane reactors including WGS related gases, *Int. J. Hydrogen Energy.* 40 (2015) 3506–3519. doi:10.1016/j.ijhydene.2014.08.074.
- [18] A. Helmi, I. Campos Velarde, F. Gallucci, M. van Sint Annaland, Hydrodynamics of dense gas-solid fluidized beds with immersed vertical membranes using an endoscopic-laser PIV/DIA technique, *Chem. Eng. Sci.* (2018). doi:10.1016/j.ces.2018.02.038.



Chapter

Six

Economic perspective for biogas to hydrogen

This chapter reflects on the research and results obtained in this thesis. A techno-economic analysis is performed on the basis of flowsheeting simulations using Aspen Puls of an integrated system for the production of 100 kg per day of hydrogen from biogas using a fluidized bed membrane reactor, and the results are compared with a reference case using a conventional small-scale steam reformer. Biogas from a landfill and an anaerobic digester were considered in the analysis at two different pressures. The conclusions reached in previous chapters of this thesis have been used to guide the selection of the operating conditions and the design of the system and reactor. The implications of the research on the perspective of the technology are discussed.

6.1. Introduction

The use of biogas for the production of hydrogen requires a system that works efficiently at small scale. Conventional decentralised small-scale hydrogen production units (10 Nm³/h up to 1000 Nm³/h) convert natural gas into hydrogen, these are commonly used for industrial applications or as supply for hydrogen filling stations. The process is based on the conventional steam reforming process taking place between 600 °C and 1000 °C, and requires downstream processing to obtain pure hydrogen. The use of biogas in these systems for the production of hydrogen has been suggested in literature [1,2]. However, these processes require energy intensive separation of the CO₂ to produce pure hydrogen, since biogas contains significant amounts of CO₂.

The process can be significantly intensified with the use of a fluidized bed membrane reactor, as separation and reaction are combined as has been demonstrated in chapters 4 and 5. However, the feasibility of a concept cannot be based on the evaluation of the reactor only. The integration of the reactor in a system and the system into a complex network is essential for the success of this technology.

This chapter shortly discusses the results of the previous chapters and on the basis of these results the integration of the FMBR with auxiliaries to form the fuel processes system is investigated by flowsheet calculations using Aspen Plus. A techno-economic analysis is carried out of the system for the production of 100 kg renewable hydrogen per day from biogas based on steam reforming with a fluidized bed membrane reactor. Steam reforming of biogas in a conventional small-scale reformer system is also simulated as a reference and is compared with the fluidized bed membrane system. The results of this analysis will help reflecting on the conclusions from previous chapters and provide a scope for future research and development of the concept.

6.2. Methodology

6.2.1. System layouts

Benchmark steam reforming

To verify the competitiveness of the fluidized bed membrane reactor concept for biogas to hydrogen it is compared to a benchmark. The benchmark used in this chapter is based on conventional high-temperature steam reforming, using biogas as a feedstock. In this process, biogas (either obtained from landfill or an anaerobic digester) is fed towards a desulfurization unit, where 99.9% sulphur removal is achieved. At this point the biogas feed splits into two parts; one part is burned in order to provide the reformer with the required heat. The other part is compressed, as moderate pressures enhance significantly the economics of the process due to smaller vessel volumes. The compressed biogas is mixed with steam, and the reaction mixture is fed to the Reforming Reactor, operating at 800 °C. After a first cooling step, the gas mixture undergoes water gas shift reaction, so that the produced CO is converted to CO₂, increasing the hydrogen production. For this reason, two adiabatic shift reactors are considered operating at different temperatures (350 °C and 200 °C), maximizing the CO conversion. Both reformer and WGS reactors were modelled in Aspen as Gibbs reactors. The H₂-rich stream is further cooled down at moderate temperature and the remaining water is removed in a condenser. The condensed H₂O is used as cooling fluid in the heat exchangers between the cascades of the shift reactors. On the other hand, the dry gas is sent to a Pressure Swing Adsorption (PSA) system, from which a high-purity H₂ stream is recovered. The obtained H₂ is further compressed to 20 bar. The heat requirements of the process are supplied by the combustion of the off-gas from the PSA unit together with an additional amount of desulfurized biogas. A schematic layout of the benchmark small-scale steam reforming process is shown in Figure 6.1.

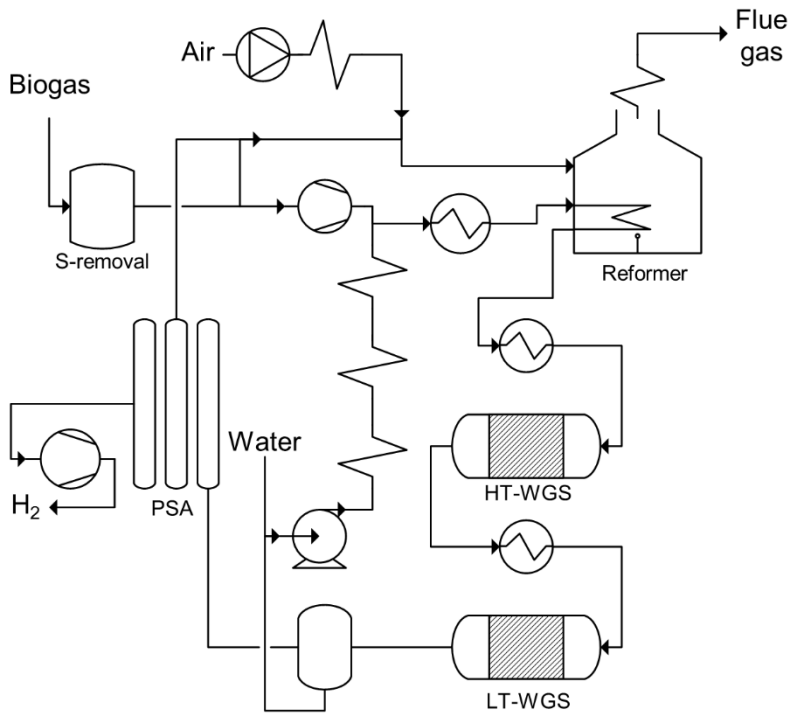


Figure 6.1. Reference Case System Layout

Membrane reformer system

The membrane reactor system has a similar layout as the benchmark plant. The results reported in chapter 3 have clearly indicated the necessity to remove sulphur from the biogas stream. The gas is then pressurised and sent to the membrane reactor. The membrane reactor is described with a stoichiometric reactor in combination with a separator which allowed to simulate the hydrogen extraction, and the final composition is subsequently obtained through a Gibbs reactor. A vacuum pump was used on the permeate side in order to increase the transmembrane H_2 partial pressure difference and increase the hydrogen flux. The vacuum pump was modelled in Aspen Plus as a compressor, which increases the permeate pressure from 0.1 bar to atmospheric pressure. Finally, a compressor was used to obtain the desired outlet pressure of hydrogen.

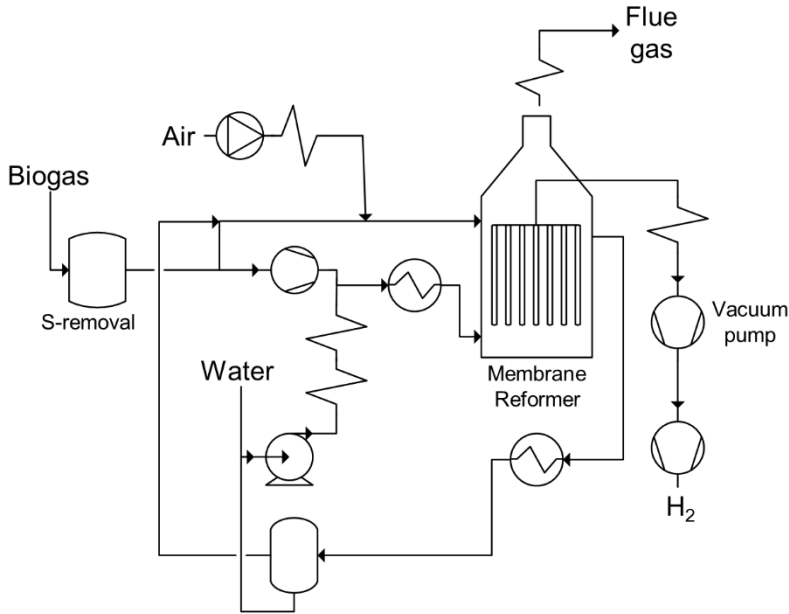


Figure 6.2. Membrane reactor plant layout

6.2.2. General definitions and assumptions

The considered hydrogen plants were designed for a production capacity of 100 kg of H_2 per day. The produced hydrogen is delivered at the same pressure for all cases (20 bar), with a desired purity of at least 4.0. The composition of Biogas (BG) may vary significantly and depends heavily on the process from which is obtained. Therefore, different raw materials and sources result in different CH_4 and CO_2 concentrations in the final mixture. In order to assess the impact of different gas concentrations in the obtained biogas, two different compositions were evaluated, one regarding landfill biogas and one regarding biogas obtained from an anaerobic digester. The Biogas compositions investigated in this chapter are presented in Table 6.1 [3,4].

Table 6.1. Biogas Compositions and lower heating value.

Component	Landfill (LF) (%mol)	Anaerobic digester (AD) (%mol)
CH ₄	44.2	58.1
H ₂ O	3.073	2.7
CO ₂	34	33.9
CO	6x10 ⁻⁴	-
H ₂	0.017	-
H ₂ S	0.01	0.4
N ₂	16	3.8
O ₂	2.7	1.1
Lower Heating Value [MJ/kg]	12.7	17.8

Landfill Biogas is characterized by a lower CH₄ content and a higher content of H₂S. The H₂S has to be removed in the early stages of the process upstream of the reformer. The amount of H₂S in the Landfill Biogas and in the Anaerobic Digester is assumed to be 100 and 4000 ppm, respectively [3].

All systems presented were simulated in Aspen Plus V10®. The Peng-Robinson cubic equation of state was used for all thermodynamic properties [5]. The main assumptions and design parameters are presented in Table 6.2. The PSA system was modelled as a separator in Aspen and the efficiency depended via a correlation on the pressure ratio between the feed and the off-gas; the lower the off-gas pressure, the higher the H₂ recovery [6,7]. The pressure of the off-gas was set at 1.2 bar. The membrane reactor system was simulated using the results and model obtained in chapter 5.

Table 6.2. List of Assumptions

Parameter	Units	Value	Reference
<i>Operating Conditions & Target Production</i>			
Ambient Temperature	°C	15	-
H ₂ Production Target	kg/day	100	-
H ₂ Purity	%	99.99	-
Plant Lifetime	years	10	-
Yearly Operation	hours	7884	-
<i>Reformer</i>			
Pressure	bar	10 and 20	-
S/C ratio	-	4	[4]
Temperature	°C	800	[8], [9]
Residence Time	min	0.021	[10]
<i>Water Gas Shift Reactors</i>			
HT Temperature	°C	350	[11]
LT Temperature	°C	200	[11]
HT Residence Time	min	0.003	[12]
LT Residence Time	min	0.03	[12]
<i>Membrane Reactor</i>			
Pressure	bar	10 and 20	-
S/C ratio (H ₂ O/CH ₄)	-	4	-
O/C ratio	-	~0.37	-
Temperature/Pressure Drop	°C	550	-
Excess of O ₂ in the Burner	%	20	-
<i>Pressure Swing Adsorption H₂</i>			
Efficiency	%	77.6-86.8	[6]
H ₂ Side Pressure Drop	bar	0.5	[4]
Reformate Pressure Outlet	bar	1.2	[4]
<i>Auxiliaries</i>			
Pumps Hydraulic Efficiency	%	70	[4]
Mechanical Efficiency	%	95	[4]
Compressors Isentropic Efficiency	%	70	[4]

The system performance was evaluated in terms of the overall system efficiency, as defined in Eq. 6.1.

$$\eta_s = \frac{\dot{m}_{H_2} LHV_{H_2}}{\dot{m}_{BG} LHV_{BG} + W_{aux}} \quad \text{Eq. 6.1}$$

Where LHV_{BG} is the low heating value of biogas at 0 °C and W_{aux} is the sum of the electric consumptions of the system auxiliaries, such as compressors, pumps and vacuum pump.

6.2.3. Economic analysis

An economic evaluation was done in order to compare the final hydrogen production cost (€/kg) of the two processes. The same methodology was used as presented in the work by Marcoberardino et al., which is widely used by many authors regarding H_2 production and power plant calculations [1,13,14]. According to the above mentioned methodology, the hydrogen production cost (COH) is defined as [15]:

$$COH = \frac{[TPC \cdot CCF] + C_{O\&M,fix} + [C_{O\&M,var} \cdot h_{eq}]}{m_{H_2}} \quad \text{Eq. 6.2}$$

With TPC being the total plant cost as shown in Eq. 6.3, calculated from the Component cost ($C_{i,2019}$) with indirect cost ($\%_{IC} = 0.14$), installation cost ($\%_{TIC} = 0.8$) and owner's and contingencies costs ($\%_{C\&OC} = 0.15$). h_{eq} stands for the operating hours of the plant within a year and the CCF represents the capital charge rate factor that matches the applicable finance structure and capital expenditure period.

$$TPC = \left[\left(\sum_i C_{i,2019} * (1 + \%_{TIC}) \right) * (1 + \%_{IC}) \right] * (1 + \%_{C\&OC}) \quad \text{Eq. 6.3}$$

The Capital Charge Factor for Independent Power Producers assuming three years as capital expenditure period and a finance structure of low risk, as the transition from a natural gas to a biogas plant does not incorporate significant diversities, is

set to 0.149. The membrane reactor setup, was assumed to be at the same technological readiness level [16].

For the determination of component cost, literature sources, reports and data available within the project of European Horizon2020 BIONICO were used [13,14,17]. The actual component cost was then scaled using equation Eq. 6.4, where the actualized component cost $C_{i,2019}$ is calculated from the reference cost ($C_{i,0}$) and the reference size ($s_{i,0}$), with the actual size (s_i) and the scale factor (f). The cost is then actualized by the CEPCI index of 2018 (603.1) and the one of the reference year. The cost assumptions concerning the operation and maintenance (O&M) and variable cost are shown in Table 6.3.

$$C_{i,2018} = \left(C_{i,0} \left(\frac{s_i}{s_{i,0}} \right)^f \right) \frac{CEPCI_{2018}}{CEPCI_y} \quad \text{Eq. 6.4}$$

Table 6.3. O&M fixed and variable costs

O&M-Fixed Costs			
Labor Costs	k€	60	[18]
Maintenance Cost	%TPC	2.5	[15], [19]
Insurance	%TPC	2.0	[15], [19]
Pd membrane tubes	k€/m ²	5.51	[20]
Auxiliaries			
Electricity	ct€/kWh	8	[21]
Process Water	€/tonne	2.0	[14]
Cooling Water	€/tonne	0.35	[14]
Raw Materials			
AD Biogas	€/GJ	3.46	[4]
LF Biogas	€/GJ	1.5	[4]
Catalysts			
High Temperature WGS Fe-based	k€/m ³	2.8	[14]
Low Temperature WGS Cu-based	k€/m ³	2.8	[14]
Activated Carbon	€/kg H ₂ S	0.77	[3]
Ni/Al ₂ O ₃	k€/m ³	10	[14]
Rh/Al ₂ O ₃	k€/m ³	53.1	[22]
Waste Processing	€/tonne	31.52	[23]

6.3. Results

6.3.1. Reference plant

A summary of the results for the reference plant is presented in Table 6.4. Both results of biogas coming from an anaerobic digester as well as from the landfill are analysed at two different pressures. The efficiency of both systems is increased when operating at an increased operating pressure of 20 bar, as less biogas is needed and the necessity of downstream compression of hydrogen is avoided. The cost of the equipment is also reduced, as less reactor volume is required and downstream compression of hydrogen is no longer required. The cost of hydrogen (COH) is found to be in the range of 6.37 - 6.68 €/kg with the presented assumptions. The COH is found to be strongly influenced by the cost of biogas. Thus the landfill gas results in lower operation cost, as it is cheaper. However, the capital cost is increased due to the lower concentration of methane. A breakdown of the capital cost is presented in Figure 6.3. These results are used as a comparative basis for the process employing a fluidized bed membrane reformer.

Table 6.4. Results of the techno-economic analysis of the reference system.

	AD 10 bar	AD 20 bar	LF 10 bar	LF 20 bar
Thermal Efficiency %	65.9	67.4	62.8	64.2
Biogas [kg/h]	39.6	39.1	57.2	56.4
Cost equipment [k€]	219	213	238	226
Cost of H ₂ [€/kg]	6.48	6.24	6.68	6.37
CAPEX [€/kg]	2.35	2.28	2.55	2.42
OPEX fixed [€/kg]	2.59	2.56	2.61	2.56
OPEX Var. [€/kg]	1.55	1.40	1.52	1.38

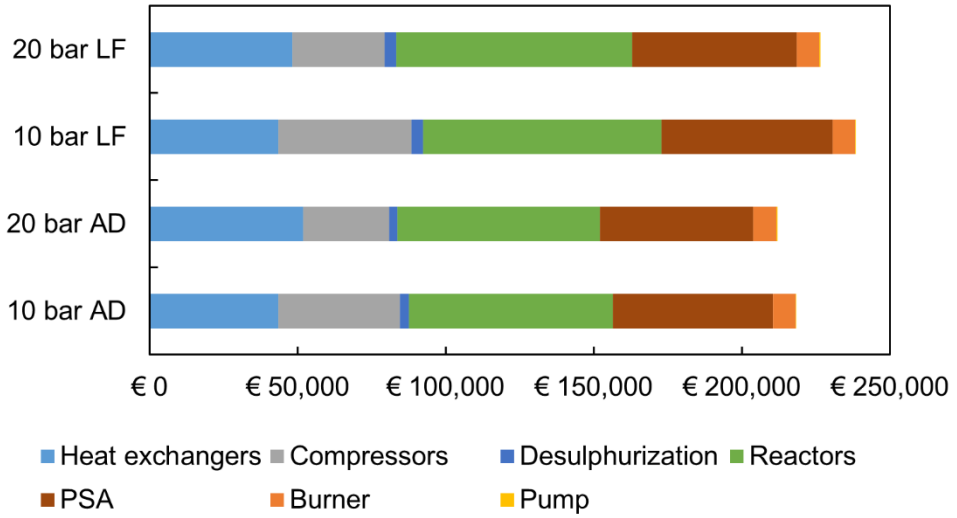


Figure 6.3. Breakdown of capital expenditures for the reference system.

6.3.2. Fluidized bed membrane reformer system

To obtain the required membrane area the phenomenological model as shown in chapter 5 was used. The mass transfer was assumed to be equal to the case at 4 U/U_{mf} and 550 °C as obtained from the experimental results shown in chapter 5. Using the model for each case a graph where the hydrogen recovery is related to the load to surface ratio is obtained, as shown in Figure 6.4 for the case of AD biogas.

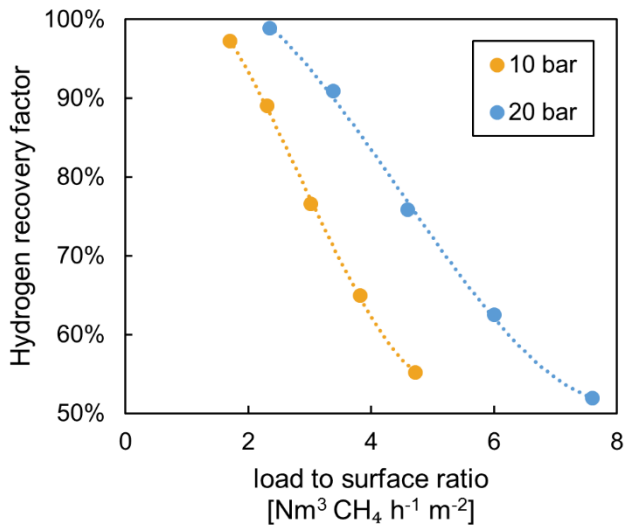


Figure 6.4. Model results of hydrogen recovery factor vs load to surface ratio at two different pressures for AD biogas at 550 °C.

The membrane reformer has shown to be able to overcome thermodynamic limitations and obtain very high conversions, as shown in previous chapters. However, when fully integrated in the system a very high recovery of hydrogen, with a corresponding very high conversion, is not always the optimal operation condition. From the analysis, it is found that with an increase in recovery the required amount of biogas to be burnt to maintain the reaction temperature is also increased. For each case presented in the following part therefore the optimal recovery was defined to minimize the COH. In Figure 6.5. Cost of hydrogen and fraction of biogas to the burner as a function of the hydrogen recovery for AD biogas at 10 and 20 bar.

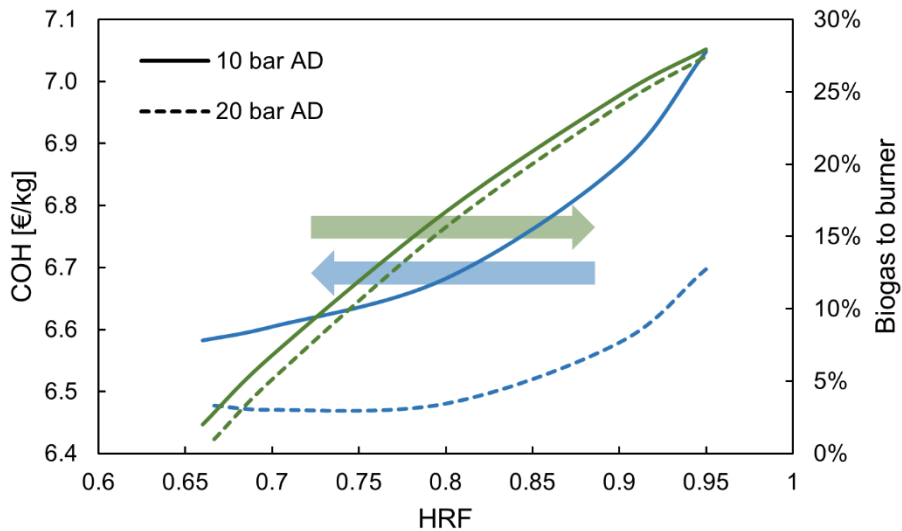


Figure 6.5. Cost of hydrogen and fraction of biogas to the burner as a function of the hydrogen recovery for AD biogas at 10 and 20 bar.

It was found that the minimum cost was between 66 and 70% of recovery at 10 and 20 bar respectively for the AD biogas. For the LF biogas this was at 68% and 71% of recovery at 10 and 20 bar operation, respectively. At this point very little extra biogas was required to be burnt, as the energy required could be almost obtained from the burning of the off-gas from the reactor. This resulted in a minimum total amount of biogas required. Moreover, the lower reaction temperature (550 °C) compared to the reference case contributed to a lower amount of biogas required and therefore a higher efficiency, see Table 6.5. Results of techno economic analysis of the fluidized bed membrane reactor system.. Additionally, the capital cost could be reduced, because the WGS units and the PSA system were no longer required. However, as can be seen in the breakdown of the CAPEX in Figure 6.6, the costs of the membranes are responsible for a large part of the CAPEX. A significant reduction in the CAPEX can be obtained by operation at higher pressures, because the reduced membrane costs because of the decreased required membrane area, exceeds the increased costs of the compressor. However, the OPEX of the membrane reformer system is increased as a result of the power required to lower the partial pressure in the permeate

side (vacuum pump) and to increase the pressure of the hydrogen up to 20 bar (compressor), eventually resulting in a higher COH compared to the reference system, 6.62-6.47 €/kg.

Table 6.5. Results of techno economic analysis of the fluidized bed membrane reactor system.

	AD 10 bar	AD 20 bar	LF 10 bar	LF 20 bar
Thermal Efficiency %	69.5	70.8	67.8	68.8
Biogas [kg/h]	36.2	35.2	51.5	50.2
Cost equipment [k€]	189	181	204	197
Cost of H2 [€/kg]	6.58	6.47	6.62	6.55
CAPEX [€/kg]	2.02	1.93	2.19	2.10
OPEX fixed [€/kg]	2.65	2.57	2.68	2.59
OPEX Var. [€/kg]	1.92	1.97	1.75	1.85

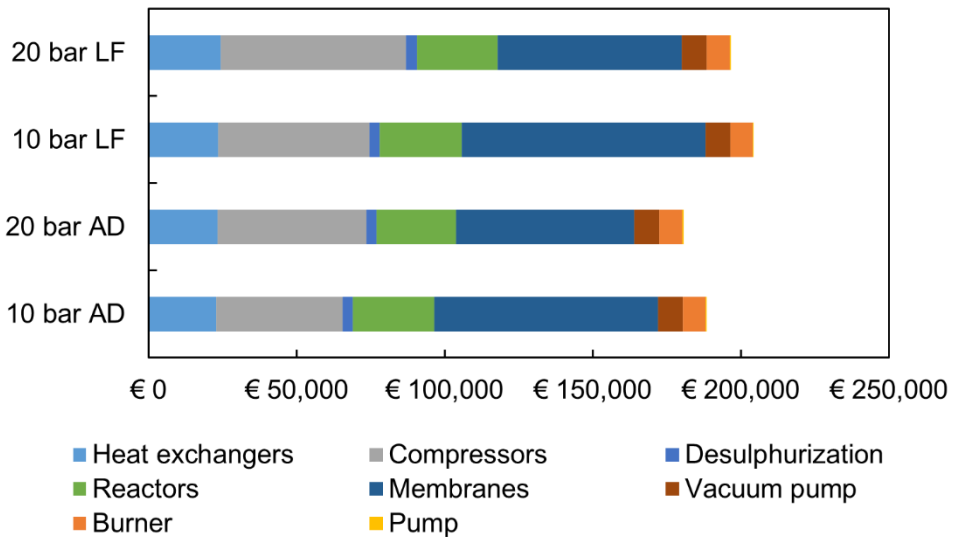


Figure 6.6. Breakdown of capital expenditures of the fluidized bed membrane reactor system.

6.3.4. Discussion

Membrane stability

The results from the techno-economic analysis should be hold in strong regard to the work presented in this thesis. As discussed in chapter 2, membrane stability and performance are key to the success of the fluidized bed membrane system. The results presented here assume membranes operating for the lifetime of the plant, under these reforming conditions. As shown in chapter 2 there was still significant degradation of the membrane performance under the presented conditions. The developments of more resilient membranes, such as the double skin membranes presented by Arratibel et al. could offer a solution to these problems [24,25]. Other solutions that could increase membrane lifetime is a method, where the membrane defects are repaired [26]. The method could be developed in such way that the membrane repair treatment can be performed in the reactor itself under certain conditions. The method would utilise the effect of grain growth at high temperature to close formed defects. If the membranes could not be repaired, recycling of the membrane should be considered, where the recycling of the palladium decreases membrane cost. All three techniques should be further developed and studied, and should result in a decrease in the membrane cost, making the system more economically viable. These are developments that should go together with commercialisation of the membrane technology. As also is shown in chapter 2 that stable operation can be achieved at milder conditions, confirming the stability and potential of these membranes for reactor concepts that operate at lower temperatures. Increasing membrane production is also estimated to result in a decrease of the cost.

H₂S removal

As demonstrated in chapter 3, the H₂S removal is an important step in the process and cannot be dismissed, as the effect of the H₂S on the membranes, catalyst and equipment is too significant. The search for more H₂S resistant membranes should be continued, however membrane stability should be considered and not only be based on performance. Additionally, conditions should be intensified as operation is often at higher pressures and lower partial pressures of hydrogen, for current use of palladium-based membranes contact with H₂S should be avoided and trace

amounts <0.25 ppm still need to be considered. Moreover, Rh as well as Ni-based catalysts are strongly influenced by sulphur poisoning. The resistance of a Rh-based catalyst is found to be higher, however still also suffers from poisoning [27]. Beside this, H_2S is not the only trace component in the biogas and also the presence of siloxanes and ammonia need to be considered for their potential effect on the system performance and durability.

Operation conditions

Chapter 4 explored the different effects of operation conditions on the steam reforming of biogas in a fluidized bed membrane reactor. The results of the techno-economic analysis show that the highest recovery is not always the optimal condition, when the optimization of the entire integrated system is considered. From the techno-economic analysis, it becomes evident that pressure and temperature can have positive effects on the reactor productivity, but can also decrease the system efficiency. Moreover, also the membrane stability imposes a temperature limit. The high diversity of different biogas feed compositions depending on the source only adds to the complexity of determining the best operation conditions. In the analysis presented in this chapter only $550\text{ }^\circ\text{C}$ and two different operating pressures were investigated. However, further integration of the phenomenological reactor model and the Aspen Plus simulations could offer further insight in finding ideal operation conditions.

An important parameter which is strongly influenced by operation conditions is the amount of biogas used. The membrane system in comparison to the reference case uses less biogas. However, variable costs are higher due to the increased electricity consumption (due to vacuum pump and compressor). The small additional amount of biogas that is required for heating could be replaced by electrical heating. Therefore the membrane system shows a higher potential for electrification, which can be expected to become increasingly important in the near future.

Catalyst

The required amount of catalyst is calculated in relation to the required membrane area, considering the concentration of catalyst applied during the lab tests

described in chapter 5. As indicated in chapter 4, there are no kinetic limitations. This means that the amount of catalyst could be further reduced, hence reducing cost. Reducing the catalyst ratio to only 10% (a possible decrease considering the high activity of the catalyst) of the used amount would reduce the CAPEX with ~2.3%. Moreover, the particle size could also have an influence on the stability of the fluidized bed, smaller particles might decrease the impact on the membrane surface enhancing the membrane stability. However, this might also affect the hydrodynamics of the system and change the mass transport towards the membranes.

Mass transfer

Concentration polarisation is discussed in both chapter 4 and 5. It was shown that the extent of concentration polarisation could be adequately described using the film layer model for the single membrane submerged in a fluidized bed. However, when scaling up in chapter 5 the influence of the fluidization behaviour becomes clear, as an increase in the velocity in the system improves the mass transfer rates towards the membranes. Moreover, it is shown that the inter-membrane distance also affects the concentration polarisation. The techno-economic analysis also allows evaluating the impact of concentration polarization on the COH. Therefore, a separate analysis was performed where the mass transfer coefficient as presented in chapter 5 was increased by 50% which brings it to the value obtained in the single membrane system (thus resembling the case where the mass transfer boundary layers of the membranes do not interact with each other). This results in a decrease in the required membrane area, and hence also in the amount of catalyst required reducing the cost of hydrogen. The results of the different cases are shown in Figure 6.7.

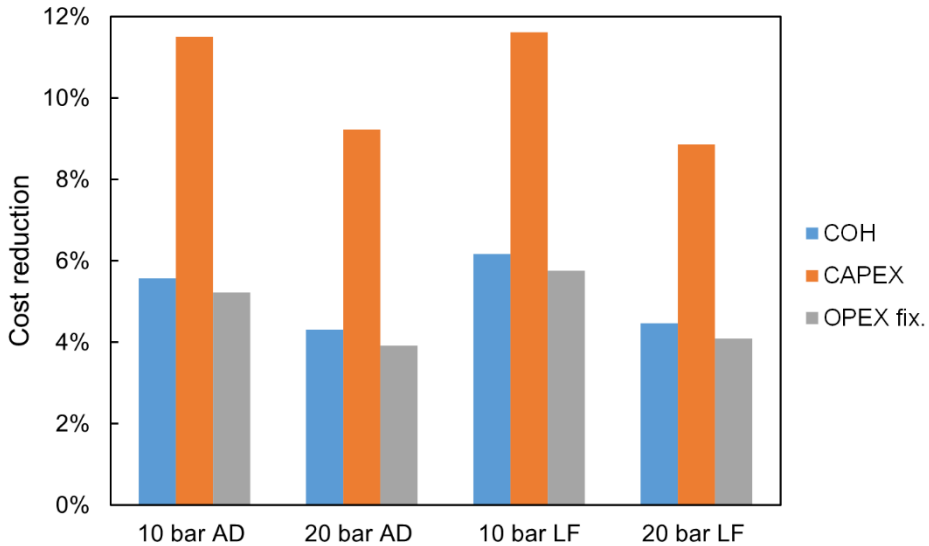


Figure 6.7. Cost reduction due to the increase in mass transfer towards the membrane.

The strong impact of the mass transport in the system is evident as almost up to 12% of the CAPEX could be reduced by an increase in the mass transfer rates. Further understanding of the mass transfer in fluidized beds could therefore help implementing further improvements on the concept, bringing the cost of hydrogen down to 6.19-6.27 €/kg. Increased velocities are therefore interesting, but the concomitant increase in demands on the membrane stability and geometry needs to be considered as well. The effects of concentration polarisation should therefore carefully be considered in the design of these systems.

6.4. Conclusions

Hydrogen is and will be indispensable for our society. The production of hydrogen must shift from a fossil-based feedstock towards renewables to reduce the environmental impact of GHG emissions produced in the process. The use of biogas as a feedstock for hydrogen is one of the pathways towards renewable hydrogen. The fluidized bed membrane reactor is a reactor concept which enables the production of hydrogen from biogas. In this chapter the fluidized bed membrane reactor was compared with the reference of conventional steam

methane reforming at small scale. The cost of hydrogen for the reference case is found to be 6.37 - 6.68 €/kg. The origin of the biogas used shows to play a role as the cost of biogas can be significantly different depending on its source. It is shown that the operation conditions and reactor performance are strongly dependent on the integration within the entire system. The CAPEX can be significantly reduced. However, membrane cost remains a significant part. The use of a vacuum pump to reduce the partial pressure on the permeate side, together with the compressor to deliver the hydrogen at 20 bar, increases significantly the power demand of the concept, resulting in an increased OPEX compared to the reference. Bringing the cost of hydrogen production in a fluidized bed membrane reactor system to 6.47-6.62 €/kg.

The most critical assumptions made in this analysis are also points that require further investigation and development and can potentially decrease the cost of hydrogen with the fluidized bed membrane reactor concept. These points have been identified as:

- membrane stability and lifetime;
- Operation conditions;
- Concentration polarization.

Where the latter is shown to be able to reduce the cost of hydrogen by almost 6% when the mass transfer is enhanced by 50%, the highest rate which was obtained in chapter 4 for the single membrane system, which resulted in a cost of hydrogen of 6.19-6.27 €/kg. This shows the potential of the fluidized bed membrane reactor to utilize biogas for the production of renewable hydrogen.

Nomenclature

AD	Anaerobic digester
CCF	Capital charge factor
CEPCI _y	Chemical engineering plant cost index
C&OC	Owner's and contingencies costs €
COH	Cost of hydrogen €/kg
$C_{O\&M,fix}$	Fixed operation and maintenance cost €
$C_{O\&M,var}$	Variable operation and maintenance cost €
$C_{i,2018}$	Cost of equipment i
$C_{i,0}$	Reference cost of equipment i
f	Scale factor
h_{eq}	Year equivalent operation
IC	Indirect cost €
LF	Landfill
LHV_i	Lower heating value of component/mixture I in MJ/kg
\dot{m}_i	Mass flow of i in kg/h
s_i	Size of the equipment i
$s_{i,0}$	Reference size of the equipment i
TIC	Installation cost €
TPC	Total plant cost €
W_{aux}	Electrical consumption in MJ/h
y	Year
η_s	System efficiency

References

- [1] L.B. Braga, J.L. Silveira, M.E. Da Silva, C.E. Tuna, E.B. Machin, D.T. Pedroso, Hydrogen production by biogas steam reforming: A technical, economic and ecological analysis, *Renew. Sustain. Energy Rev.* 28 (2013) 166–173. doi:10.1016/j.rser.2013.07.060.
- [2] H.J. Alves, C. Bley Junior, R.R. Niklevicz, E.P. Frigo, M.S. Frigo, C.H. Coimbra-Araújo, Overview of hydrogen production technologies from biogas and the applications in fuel cells, *Int. J. Hydrogen Energy.* 38 (2013) 5215–5225. doi:10.1016/j.ijhydene.2013.02.057.
- [3] Q. Sun, H. Li, J. Yan, L. Liu, Z. Yu, X. Yu, Selection of appropriate biogas upgrading technology-a review of biogas cleaning, upgrading and utilisation, (2015). doi:10.1016/j.rser.2015.06.029.
- [4] G. Marcoberardino, D. Vitali, F. Spinelli, M. Binotti, G. Manzolini, G. Di Marcoberardino, et al., Green Hydrogen Production from Raw Biogas: A Techno-Economic Investigation of Conventional Processes Using Pressure Swing Adsorption Unit, *Processes.* 6 (2018) 19. doi:10.3390/pr6030019.
- [5] D.-Y. Peng, D.B. Robinson, A New Two-Constant Equation of State, *Ind. Eng. Chem. Fundam.* 15 (1976) 59–64. doi:10.1021/i160057a011.
- [6] G.Q.M. J. Stocker, M. Whysall, 30 Years of PSA Technology for Hydrogen Purification, (1998).
- [7] C.A. Grande, PSA Technology for H₂ Separation, in: *Hydrog. Sci. Eng. Mater. Process. Syst. Technol.*, Wiley-VCH Verlag GmbH & Co. KGaA, Weinheim, Germany, 2016: pp. 489–508. doi:10.1002/9783527674268.ch21.
- [8] Y. Matsumura, T. Nakamori, Steam reforming of methane over nickel catalysts at low reaction temperature, *Appl. Catal. A Gen.* 258 (2004) 107–114. doi:10.1016/j.apcata.2003.08.009.
- [9] B. Tjaden, M. Gandiglio, A. Lanzini, M. Santarelli, M. Jä Rvinen †, Small-Scale Biogas-SOFC Plant: Technical Analysis and Assessment of Different

- Fuel Reforming Options, (2014). doi:10.1021/ef500212j.
- [10] E. Pellizzari, Hydrogen Production from Biogas Using Fluidized Bed Membrane Reactors: Modeling and Experimental Validation of the Reactor and System Techno-economic Assesment, (n.d.).
- [11] D. Falleiros, B. Lima, F.A. Zanella, M.K. Lenzi, P.M. Ndiaye, 4 Modeling and Simulation of Water Gas Shift Reactor: An Industrial Case, n.d.
- [12] G. Barbieri, W Water Gas Shift (WGS), (n.d.). doi:10.1007/978-3-642-40872-4_598-1.
- [13] G. Di Marcoberardino, D. Vitali, F. Spinelli, M. Binotti, Green Hydrogen Production from Raw Biogas: A Techno-Economic Investigation of Conventional Processes Using Pressure Swing Adsorption Unit, (2018). doi:10.3390/pr6030019.
- [14] V. Spallina, D. Pandolfo, A. Battistella, M.C. Romano, M. van Sint Annaland, F. Gallucci, Techno-economic assessment of membrane assisted fluidized bed reactors for pure H₂ production with CO₂ capture, *Energy Convers. Manag.* 120 (2016) 257–273. doi:10.1016/j.enconman.2016.04.073.
- [15] Toward a Common Method of Cost Estimation for CO₂ Capture and Storage at Fossil Fuel Power Plants, 2013.
- [16] F. Gallucci, J. Antonio Medrano, L. Roses, A. Brunetti, G. Barbieri, J. Viviente, et al., Process Intensification via Membrane Reactors, the DEMCAMER Project, *Processes*. 4 (2016) 16. doi:10.3390/pr4020016.
- [17] BIONICO, Biogas membrane reformer for decentralized H₂ production, *Fuel Cells Hydrog. 2 Jt. Undert. under Grant Agreem. No 671459*. (2015). <http://www.bionicoproject.eu/>.
- [18] Average Salary in European Union 2018 | Reinis Fischer, (n.d.).
- [19] Power Plant Cost Estimation Methodology Quality Guidelines for Energy System Studies, 2011.
- [20] E. Fernandez, A. Helmi, J.A. Medrano, K. Coenen, A. Arratibel, J. Melendez,

- et al., Palladium based membranes and membrane reactors for hydrogen production and purification: An overview of research activities at Tecnalia and TU/e, *Int. J. Hydrogen Energy*. 42 (2017) 13763–13776. doi:10.1016/j.ijhydene.2017.03.067.
- [21] Industrial prices for electricity in the Netherlands 1995-2017 | Statistic, (n.d.). <https://www.statista.com/statistics/596254/electricity-industry-price-netherlands/>.
- [22] G. Di Marcoberardino, S. Foresti, M. Binotti, G. Manzolini, Potentiality of a biogas membrane reformer for decentralized hydrogen production, *Chem. Eng. Process. - Process Intensif.* 129 (2018) 131–141. doi:10.1016/j.cep.2018.04.023.
- [23] I.K. Kookos, *Introduction to chemical plant design*, Tziola, 2009.
- [24] A. Arratibel, J.A. Medrano, J. Melendez, D.A. Pacheco Tanaka, M. van Sint Annaland, F. Gallucci, Attrition-resistant membranes for fluidized-bed membrane reactors: Double-skin membranes, *J. Memb. Sci.* 563 (2018) 419–426. doi:10.1016/j.memsci.2018.06.012.
- [25] A. Arratibel, A. Pacheco Tanaka, I. Laso, M. van Sint Annaland, F. Gallucci, A. Pacheco, et al., Development of Pd-based double-skinned membranes for hydrogen production in fluidized bed membrane reactors, *J. Memb. Sci.* 550 (2018) 536–544. doi:10.1016/j.memsci.2017.10.064.
- [26] N. Lu, D. Xie, F. Wang, Repair of palladium membrane modules by metallic diffusion bonding, in: *Int. J. Hydrogen Energy*, 2014. doi:10.1016/j.ijhydene.2014.02.027.
- [27] M.A. Ocsachoque, J.I. Eugenio Russman, B. Irigoyen, D. Gazzoli, M.G. González, Experimental and theoretical study about sulfur deactivation of Ni/ CeO₂ and Rh/CeO₂ catalysts, *Mater. Chem. Phys.* 172 (2016) 69–76. doi:10.1016/j.matchemphys.2015.12.062.

List of publications

Publications

2019

N.C.A. de Nooijer, J.Davalos Sanchez, J. Melendez Rey, E Fernandez, D.A. Pacheco Tanaka, M. van Sint Annaland, F. Gallucci. "Influence of H₂S on the hydrogen flux of thin-film PdAgAu membranes" International Journal of Hydrogen Energy. In Press, Corrected Proof (2019)

J. Liu, S. Bellini, **N.C.A. de Nooijer**, Y Sun, D.A. Pacheco Tanaka, C. Tang, H. li, F. Gallucci, A. Caravella. "Hydrogen permeation and stability in ultra-thin PdRu supported membranes" International Journal of Hydrogen Energy. In Press, Corrected Proof (2019)

N.C.A. de Nooijer, A. Arratibel Plazaola, J. Melendez Rey, E. Fernandez, D.A. Pacheco Tanaka, M. van Sint Annaland, F. Gallucci. "Long-term stability of thin-film Pd-based supported membranes", Processes, 7 – 2 (2019), 106

2018

N.C.A. de Nooijer, F. Gallucci, E. Pellizzari, J. Melendez, D.A. Pacheco Tanaka, G. Manzolini, M. van Sint Annaland. "On concentration polarisation in a fluidized bed membrane reactor for biogas steam reforming: modelling and experimental validation", Chemical Engineering Journal. 348 (2018), 232-243.

S. Foresti, G. Di Marcoberardino, G. Manzolini, **N.C.A. de Nooijer**, F. Gallucci, M. van Sint Annaland. "A comprehensive model of a fluidized bed membrane reactor for small-scale hydrogen production", Chemical engineering and processing: process intensification, 127 (2018), 136-144.

2017

E. Fernandez, A. Helmi Siasi Farimani, J.A. Medrano Jimenez, K.T. Coenen, A. Arratibel Plazaola, J. Melendez Rey, **N.C.A. de Nooijer**, J.L. Viviente, J. Zuniga, M. van Sint Annaland, F. Gallucci, D.A. Pacheco Tanaka. "Palladium based membranes and membrane reactors for hydrogen production and purification: An

overview of research activities at Tecnalia and TU/e", *International Journal of Hydrogen Energy* 42 (19) (2017), 13763-13776.

J. Melendez Rey, **N.C.A. de Nooijer**, K.T. Coenen, E. Fernandez, J.L. Viviente, M. van Sint Annaland, P.L. Arias, D.A. Pacheco Tanaka, F. Gallucci. "Effect of Au addition on hydrogen permeation and the resistance to H₂S on Pd-Ag Alloy membranes", *Journal of Membrane Science*, 542 (2017), 329-341.

2016

(Master Thesis)

J.A. Medrano Jimenez, **N.C.A. de Nooijer**, F. Gallucci, M. van Sint Annaland. "Advancement of an Infra-red technique for whole-field concentration measurements in fluidized beds", *Sensors* 16 (3) (2016), 300.

Conference Contribution

2019

N.C.A. de Nooijer, J.Davalos Sanchez, J. Melendez Rey, E Fernandez, D.A. Pacheco Tanaka, M. van Sint Annaland, F. Gallucci. "Fluidized bed membrane reactor for hydrogen production from biogas" 14th International Conference on Membrane Reactors (ICCMR13), 8-11 July 2019, Eindhoven, The Netherlands. Oral presentation.

N.C.A. de Nooijer, M. van Sint Annaland, F. Gallucci. "Investigation on the Mass Transfer Rates in Fluidized Bed Membrane Reactors" Fluidization XVI 26-31 May 2019, Guilin, China. Oral presentation.

2018

N.C.A. de Nooijer, T. Bavoso, O. David, M. van Sint Annaland, F. Gallucci. "On the mass transfer rates in fluidized bed membrane reactors", 25th International Conference on Chemical Reaction Engineering (ISCRE25) 20-23 May 2018, Florence, Italy. Oral presentation.

N.C.A. de Nooijer, J. Melendez Rey, E. Fernandez, D.A. Pacheco Tanaka, M. van Sint Annaland, F. Gallucci. "Design and demonstration of a lab-scale fluidized bed

membrane reactor for biogas steam reforming”, European Hydrogen Energy Conference 2018 (EHEC18), 14-16 March 2018, Malaga, Spain. Oral presentation.

D.A. Pacheco Tanaka, **N.C.A. de Nooijer**, E. Fernandez, J. Melendez, J.L. Viviente, J.A. Medrano, A. Arratibel Plazaola, M. van Sint Annaland, F. Gallucci. “Palladium membrane reactors for hydrogen production”, European Hydrogen Energy Conference 2018 (EHEC18), 14-16 March 2018, Malaga, Spain. Oral presentation.

2017

N.C.A. de Nooijer, J. Melendez Rey, E. Fernandez, D.A. Pacheco Tanaka, M. van Sint Annaland, F. Gallucci. “Steam reforming of biogas in a fluidized-bed membrane reactor for the production of hydrogen” 10th World Congress of Chemical Engineering (WCCE10), 1-5 October 2017, Barcelona, Spain. Oral presentation.

N.C.A. de Nooijer, T. de Hoon, A. Arratibel Plazaola, J. Melendez Rey, E. Fernandez, D.A. Pacheco Tanaka, M. van Sint Annaland, F. Gallucci. “Stability of cermic supported Pd-Ag membranes for hydrogen production in a fluidized bed membrane reactor”, 13th International Conference on Membrane Reactors (ICCMR13), 10-13 July 2017, Houston, USA. Oral presentation.

2015

J.A. Medrano Jimenez, **N.C.A. de Nooijer**, A. Helmi Siasi Farimani, F. Gallucci, M. van Sint Annaland. “Development of a novel experimental technique for the study of mass transfer in fluidized bed membrane reactors”, 12th International Conference on Catalysis in Membrane Reactors (ICCMR12), 22-25 June 2015, Szczecin, Poland. Oral presentation.

Workshops and other contributions

2018

A. Cruellas, **N.C.A. de Nooijer**, M. van Sint Annaland, F. Gallucci. “Inorganic membranes: a way to intensify chemical processes”, NL GUTS/NMG meeting membrane separation, 6 March 2018, Amersfoort, Netherlands. Oral presentation.

2017

N.C.A. de Nooijer, F. Gallucci, E. Pellizzari, J. Melendez Rey, E. Fernandez, D.A. Pacheco Tanaka, G. Manzolini, M. van Sint Annaland. "Steam reforming of biogas for hydrogen production in a fluidized bed membrane reactor modelling and experimental validation", Third European Workshop on Membrane Reactors: Membrane Reactors for Process Intensification (MR4PI2017), 9-10 March 2017, Verona, Italy. Poster presentation.

2016

N.C.A. de Nooijer, J. Melendez, E. Fernandez, D.A. Pacheco Tanaka, M. van Sint Annaland, F. Gallucci. "Steam reforming of biogas in a fluidized bed membrane reactor for pure hydrogen production" Nederlands Membranen genootschap Jubileum posterdag 2016, Apeldoorn, Netherlands. Poster presentation

Curriculum vitae

Niek Camiel Adriaan de Nooijer was born on October 20th 1990 in Breskens, the Netherlands. In 2008 he completed his high school education at Het Zwin College in Oostburg. He continued his education at Avans University of Applied Science in Breda, where he studied Chemical Engineering and received the degree of Bachelor of Applied Science in 2012. In the same year he started the pre-master program Chemical Engineering at Eindhoven University of Technology, followed by the master. For his graduation thesis, he worked on the development of a novel experimental technique for mass transfer measurement in fluidized beds. He graduated in 2015 in the research group Chemical Process Intensification and received the degree Master of Science. In September 2015, Niek started the PhD program of Eindhoven University of Technology, as part of the European project BIONICO, in the research group Chemical Process Intensification. His research focused on the development of the fluidized bed membrane reactor for the production of hydrogen through steam reforming of biogas, of which the results are presented in this thesis. From Januari 2020 Niek will be working as Process Engineer at G.I. Dynamics B.V. in Wateringen.